Physik-Department

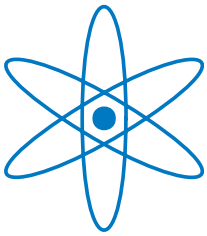

A Monte-Carlo Model of a Silicon Photomultiplier

Dissertation

von

Jožef Pulko

Technische Universität
München

TECHNISCHE UNIVERSITÄT MÜNCHEN
Fakultät für Physik
Lehrstuhl für Experimentalphysik E18

A Monte-Carlo Model of a Silicon Photomultiplier

Jožef Pulko

Vollständiger Abdruck der von der Fakultät für Physik der Technischen Universität München zur Erlangung des akademischen Grades eines

Doktors der Naturwissenschaften (Dr. rer. nat.)

genehmigten Dissertation.

Vorsitzender:	Univ.-Prof. Dr. Peter Vogl
Prüfer der Dissertation:	
	1. apl. Prof. Dr. Sibylle Ziegler
	2. Univ.-Prof. Dr. Stephan Paul

Die Dissertation wurde am 09.11.2012 bei der Technischen Universität München eingereicht und durch die Fakultät für Physik am 19.12.2012 angenommen.

Abstract

This work addresses silicon photomultipliers (SiPMs) which, on grounds of their outstanding properties, have been found to be very promising photodetectors for the future simultaneous positron emission tomography (PET) and magnet resonance imaging (MRI). SiPMs are attractive for the combined PET/MRI imaging because they are insensitive to magnetic fields, have high internal gain, good time resolution and high photon detection efficiency.

Presented in this work are measurements using a unique detector design with a single channel readout of LYSO (Lutetium Yttrium Orthosilicate) scintillator crystals using the SiPMs. Two SiPMs from the company Hamamatsu Photonics (Multi-Pixel-Photon-Counter - MPPC), differing mainly in cell size, and scintillating crystals from the company St. Gobain ($PreLude^{TM}$ 420) were used. These detector modules were investigated mainly with regard to linearity and energy resolution. In addition, gain uniformity and potential application for combined PET/MRI systems, using a SiPM matrix consisting of 4 monolithic rows of 1×4 SiPMs, was investigated. The SiPM matrix was also manufactured by Hamamatsu Photonics while the scintillating crystal block was produced by Sinocera. The detector block is designed on the principle of single channel readout. Here each scintillating crystal is optically coupled one-to-one to a single SiPM channel.

A realistic, Monte-Carlo based model describing the signal of a SiPM coupled to a scintillating crystal, which includes all important characteristics of a SiPM and a scintillating crystal, is presented in the second part of the thesis. With the help of this model the influences of various SiPM parameters on the detector performance were studied. These studies show important guidelines for choosing the optimal operating configuration of SiPMs . A simulation shows which SiPM

parameters are in need of special attention and which have a small influence on the performance in PET. This information can be used for future development of SiPMs designed for readout of specific scintillating crystals. Finally the performance of three different SiPMs from Hamamatsu Photonics coupled to different scintillating crystals, which are potentially suitable for combined PET/MRI, were investigated with the developed model. This study can help to choose optimal scintillating crystals for commercially available SiPMs.

Abstract

Die vorliegende Arbeit beschäftigt sich mit Silizium-Photomultipliern (SiPM), die aufgrund ihrer herausragenden Eigenschaften sehr vielversprechende Photodetektoren für zukünftige kombinierte Positronen-Emissions-Tomography (PET) und Magnet-Resonanz-Tomographie (MRI) sind. So sind sie unempfindlich gegenüber magnetischen Feldern, besitzen eine hohe interne Verstärkung, eine gute Zeitauflösung und hohe Photodetektionseffizienz.

Im ersten Teil werden Messergebnisse einzelner SiPMs gekoppelt mit LYSO (Lutetium-Oxyorthosilikat) als Szintillator vorgestellt. Bei den einzelnen SiPMs handelt es sich um zwei in ihrer Einzelzellgröße unterschiedliche MPPCs (Multi-Pixel-Photon-Counter) der Firma Hamamatsu, als Szintillationskristall kam $PreLude^{TM}$ 420 der Firma St. Gobain zum Einsatz. Diese beiden Typen wurde vor allem in Hinblick auf Linearität und Energieauflösung untersucht. Außerdem wurde ein monolithisches Array von SiPMs mit jeweils 4 Reihen a 1×4 SiPMs auf die Uniformität der Verstärkung und den möglichen Einsatz für kombiniertes PET/MRI untersucht. Das Array wurde ebenfalls von der Firma Hamamatsu hergestellt, der darauf gekoppelte Block mit den Szintillationskristallen stammt von der Firma Sinocera. Dieser Detektorblock ist nach dem Prinzip der Einzelkanalauslese konzipiert. So ist auf jeden SiPM ein einzelner Szintillationskristall eins-zu-eins gekoppelt.

Ein realistisches, Monte-Carlo basiertes Modell zur Beschreibung und zum Verständnis der Vorgänge in einem SiPM wird im zweiten Teil vorgestellt. Das Modell enthält alle wichtigen Parameter eines SiPMs und berücksichtigt den darauf gekoppelten Szintillator. Es wurden der Einfluss bei Änderung der Parameter auf die Leistung des Detektors als auch mögliche Verbesserungsansätze für die Produktion von SiPMs

evaluiert. Die Wichtigkeit der einzelnen Parameter hängt dabei vom Anwendungsgebiet ab, hier wurde detailliert auf die optimalen Werte für PET eingegangen. Hierfür wurden mit dem entwickelten Modell drei verschiedene SiPMs von Hamamatsu gekoppelt mit verschiedenen für PET in Frage kommenden Szintillatoren studiert. Mit dem Modell kann so auch der passende Szintillator für bereits kommmerziell erhältliche SiPMs gefunden werden.

Although many people have influenced my life, one person has taught me more than anyone else: my mother. I therefore dedicate my thesis to my dearest mother.

Acknowledgements

Foremost I would like to thank Prof. Sybille I. Ziegler for giving me the opportunity to work in her group and letting me experience the interesting field of nuclear medicine as well as for her guidance and for sharing her immense knowledge on nuclear physics and instrumentation with me.

I am also very indebted to Prof. Stephan Paul for supporting my thesis and giving me the opportunity to work in collaboration with Physics department E18.

I also thank to my nearest coworkers Florian Schneider and Melanie Hohberg for continuous support. They were always open to every kind of discussion from which many interesting ideas arose. I learned a lot from them and we had a lot of fun.

Additional thanks go to my friend, John Lloyd Peitz for the cooperative, friendly and motivating atmosphere.

I specially thank to the colleagues from the Department of Nuclear Medicine for these years working together: Ralph Bundschuh, Arne Tapfer, Dominik Schulz, Katharina McGuire, Sebastian Fürst, Katja Zechmeister, Astrid Velroyen and Kuangyu Shi.

I would like to mention, the work with Dieter Renker was a very valuable experience. Thanks to his deep and broad knowledge of semiconductor detectors, his suggestions were always of great help.

Through the collaboration with the Experimental Particle Physics Department (F9) from Jožef Štefan Inštit I had the opportunity to test the SiPMs with a very advanced detector-test-setup. Many thanks to to Peter Križan, Samo Korpar, Rok Dolenec and Rok Pestotnik.

Posebna zahvala gre mojim starsem, sestri in partnerki za moralno podporo v vseh teh letih.

Acknowledgment goes to my funding sources, namely the Bayerische Forschungsstiftung, Deutsche Forschungsgemeinschaft and Javni sklad Republike Slovenije za razvoj kadrov in Štipendije for providing me support.

Contents

1

Introduction

1.1 Motivation

Positron Emission Tomography (PET) is a nuclear imaging technique that provides metabolic information about processes occurring in the human body (1). These images a have high clinical relevance as demonstrated in many studies. PET uses positron-emitting radionuclides that label compounds of biological interest. The ejected positron slows down and interacts with an atomic electron. The two annihilate and two 511 keV γ-rays are emitted back-to-back. A PET scanner consists of a ring of detectors surrounding the object that is to be imaged. High energy γ-rays in PET are usually detected via the scintillation detection principle. In this method the high energy photon deposits its energy in a scintillating crystal which, as a result emits a burst of optical photons which are then converted into an electrical signal by the photodetector which is read-out by additional electronics. These events are then reconstructed into a tomographic image using mathematical algorithms. The result is a spatial distribution of radiolabeled tracers in a living human body. However PET has a relatively low spatial resolution of about 1 mm and only gives rough information about the size and shape of organs. Therefore, in the past, this modality was combined with Computerized Tomography (CT) in order to provide an anatomical reference for the localization of lesions. However, PET/CT has some drawbacks and some limitations. Both methods induce a radiation exposure. CT has reduced soft tissue contrast compared to Magnetic Resonance Imaging (MRI). MRI reveals the structural details of the various organs and provides information on their physiological status and pathologies. With MRI there is no radiation exposure since this method usees magnetic fields and radio waves to probe the nuclei of hydrogen atoms existing in

the water molecules within body cells. Therefore MRI should be a better complementary modality for hybrid PET imaging. However integrating PET hardware inside of a MRI is difficult. A fundamental problem of this combination is the operation of photodetectors inside strong magnetic fields. Conversely, the PET detector ring may corrupt the performance of the MRI system.

Thanks to the development over the last years in the field of semiconductor photodetectors, fusion of PET and MRI in hardware is now possible (2, 3). Especially the Silicon Photomultiplier (SiPM) has shown great potential as a photodetector for simultaneous PET/MRI imaging, since it is insensitive to magnetic fields and has high gain, therefore operation without complicated amplification and simple readout electronics is possible. Different studies have already shown the potential of SiPMs for hybrid PET/MRI systems (4, 5, 6, 7, 8, 9, 10). However SiPMs are still relatively new detectors with a lot of potential for improvement and further development.

Many different designs of SiPMs are possible and they can be tailored quite well to the specific needs of experiments. However, the characteristics of their signal are complicated due to dark counts, strong temperature dependence, nonlinear response, optical inter-cell crosstalk and afterpulses, as well as wavelength and operation voltage dependent sensitivity. The optimization of these parameters involves many trade-offs and varies widely between applications. Some of these effects can be reduced during production and some can be optimized with carefully chosen operating parameters. Various types of SiPMs are available at the moment and there is a strong ongoing development towards improving current SiPMs (11, 12, 13, 14, 15). Therefore precise models of SiPM signal generation are necessary to find the optimal parameters for a specific task. Pioneering work has already been presented in the modeling and the theoretical analysis of SiPM signals coupled with scintillating crystals (16, 17, 18). However, these models do not include the complete characteristics of a SiPM and may therefore not offer sufficient accuracy in all cases. The goal of this study was to develop a realistic model describing the performance of SiPMs when coupled to scintillating crystals.

1.2 Overview

This thesis first describes the fundamental properties and problems of SiPMs in chapter 2. This chapter also presents a method for SiPM nonlinearity correction.

In chapter 3, measurements of single channel SiPMs from Hamamatsu coupled to LYSO scintillating crystals are presented regarding linearity and energy resol-

ution. Measurements of the gain uniformity of a 4×4 SiPM matrix, consisting of 4 monolithic rows of 1×4 SiPMs, are presented in chapter 4. The SiPM matrix was coupled to a block containing 32 scintillating crystals and investigated for the performance in PET/MRI systems.

The core of the thesis is a realistic model describing the signal of a SiPM which is presented in chapter 5. The developed model was validated by experimental dark count spectra, a low light intensity LED and the LYSO scintillating crystal. Chapter 7 studies the influence of different SiPM parameters on the detector performance with help of the developed model. The final chapter deals with the simulated performance of three different SiPMs from Hamamatsu coupled to different, potentially suitable, scintillating crystals for combined PET/MRI systems.

2

Silicon Photomultiplier

Semiconductor detector devices became available in the early 1960s. They created a lot of interest since they, compared to other detectors available at that time, hade a good energy resolution and they could be produced of small dimensions. Good energy resolution of semiconductor detectors is a consequence of a large number of electron-hole pairs (information carriers) generated by the interaction of observed radiation. The success of semiconductors started with the p-i-n (PIN) diode developed in the 1960s (19), the main drawback of this detector was its low photon detection efficiency (PDE). The next important step was the development of the avalanche photodiode (APD). As the name implies this detector uses internal avalanche multiplication, which improved the efficiency of the detector. However the photomultiplier tube (PMT) still had a higher PDE and better timing properties as an APD. It was not until in the beginning of the 21st century that semiconductor photodetectors with a PDE higher that that of a PMT were developed. These detectors are called silicon photomultipliers (SiPM, other notations are: G-APD, GM-APD, MPPC, SPAD, SSPM) and consist of an array of single-channel APDs (Avalanche Photodiode, cells) operated in limited Geiger-mode (20, 21). SiPMs combine the best of APDs and PMTs, since they are insensitive to magnetic fields but also have high internal gain and a fast response time. In addition SiPMs have numerous other advantageous properties like superior photon detection efficiency, single photon resolution, low power consumption, low operating voltage, the potential for low-cost mass production and the design of compact high resolution modules. Therefore they are good candidates for a photodetector in numerous applications. The basic principles and operation, state of the development and the problems of this device will be discussed in this chapter.

2.1 Principle of Operation

A SiPM consist of an array of single channels APDs reverse biased $10\% - 20\%$ above the breakdown voltage (V_{Bias} in figure 2.2). A strong electric field is created in each cell in a small volume close to the detector surface. In this condition the detector is in a metastable state which is maintained only as long as the detectors sensitive volume is depleted. However one single free charge carrier in the active area is enough to destabilize the detector and trigger an avalanche breakdown of a cell. The cells in the SiPM are connected parallel via integrated poly-silicon quenching resistors (R_q) which quench the avalanche and limit the current-flow (Fig. 2.1). The quenching resistor (R_q) limits the current as the voltage applied to the diode decreases. When the bias voltage drops to break down voltage V_{BD} the multiplications process stops. A triggered avalanche discharges the cell capacitance (C_C) with a time constant

$$\tau_{CDec} = R_q \cdot C_C. \tag{2.1}$$

At the same time the external current asymptotically grows to

$$I = \frac{V_{Bias} - V_{BD}}{R_q}, \tag{2.2}$$

where V_{Bias} is the operating bias voltage. As a result, the gain is obtained as capacitance of the cell (C_C) divided by the elementary charge (q_0) times the overvoltage

$$G = C_C \frac{V_{Bias} - V_{BD}}{q_0}. \tag{2.3}$$

A typical gain of SiPMs is between 10^5 and 10^6, therefore single cell SiPM pulses can be seen on the oscilloscope without amplification. After avalanche breakdown the SiPM slowly starts to recharge until the voltage across the device returns to the original bias voltage (Fig. 2.2). Different models of a SiPM were considered (22, 23), one very simple circuit is presented in figure 2.1.

When photons interact in the photodetector, the electrons or holes created drift towards the high electric field region where they are accelerated, producing an avalanche. Signals generated by a single SiPM cell in Geiger-mode have a standardized signal (S_0) with high gain, which is independent of the number of photons that initiate it. However, since the cell outputs are connected in parallel they form a summed signal which, due to the multi-cell structure, is proportional

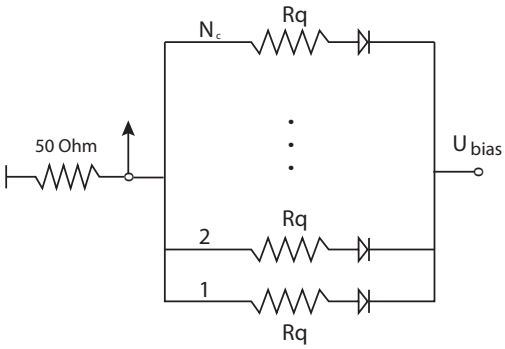

Figure 2.1: Simple equivalent circuit of the SiPM with readout.

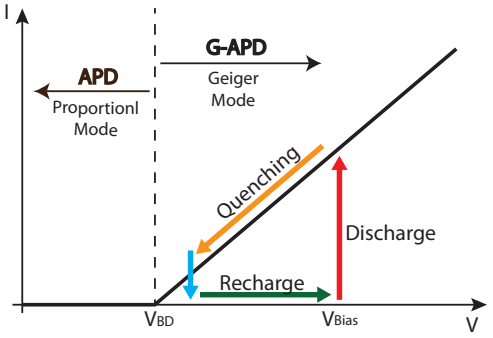

Figure 2.2: Schematic of the working principle of SiPMs.

to the incident photon flux

$$Signal = \sum_{i=1}^{n} S_0. \tag{2.4}$$

With this concept SiPMs have high gain (10^5 to 10^6), good photon detection efficiency ($> 20\%$) and good timing resolution ($< 100\ ps$).

2.2 Photon Detection Efficiency

The photon detection efficiency (PDE) of the SiPM represents the effective probability that an incident photon triggers an avalanche breakdown and depends on the wavelength of incident photons, bias voltage and temperature. The PDE in SiPM can be factorized in quantum efficiency (QE), avalanche probability (P_a) and the geometrical efficiency (GE):

$$PDE(\lambda, V_{Bias}, T) = QE(\lambda) \cdot P_a(\lambda, V_{Bias}, T) \cdot GE. \tag{2.5}$$

Geometrical efficiency is the ratio between the active and the total area of the SiPM since some parts of SiPMs are unsensitive due to the area needed between cells for separation and placement of resistors. GE is a compromise between the cell density and the PDE which needs to be optimized depending on the application. For Hamamatsu SiPMs the GE is between 30% and 60% (24). A back illuminated drift SiPM concept proposes GE at almost 100% (12, 25, 26). However functioning devices have yet to be presented. Another concept which

allows high PDE while retaining a high cell density is the fabrication of SiPMs with bulk integrated quenching resistors (14, 15, 27).

Quantum efficiency is the probability that an electron-hole pair is generated (typical values between 80% and 90%). This probability has a strong dependency on the wavelength of the incident photons due to the thin sensitive layer of SiPMs.

Avalanche probability is the probability that an electron-hole pair initiates a cell breakdown. It linearly depends on the SiPM's bias voltage as well as the position where the primary electron-hole pair is generated (28). A report on the absolute PDE measurements of different types of SiPMs for wavelengths from 350 to 1000 nm can be found in (29). What is often not included in the PDE discussions is that PDE changes with time when measuring high photon fluxes, since the cell that triggers needs a certain time to recover and its PDE is temporary lower than that of its normal operating condition. An important property of SiPMs is the fairly uniform PDE between cells as can be seen in chapter 4 and was also reported by other groups (29, 30). Variation of about 10% to 20% in PDE between cells was observed.

The PDE depends on the overvoltage where operation at higher voltages is favorable (31). Unfortunately the dark count rate, crosstalk and afterpulses increase with overvoltage as well.

2.3 Noise

A cell breakdown can be triggered by an electron-hole generated by an incident photon or by any other process which generates free charge carriers in the depleted layer of the SiPM. The latter contributes to the noise which randomly triggers cells. There are three processes responsible for noise in SiPMs: dark counts, crosstalk and afterpulses.

2.3.1 Dark Counts

Dark counts are caused by charge carriers in the depleted region due to two main processes: thermally generated electron-hole pairs and field-assisted generation of free charge carriers. The amount of thermally generated charge carriers can be reduced by cooling. Thermally generated dark counts are reduced by a factor of approximately two for every $8°C$ drop in temperature (19). Dark counts could be reduced with optimized production processes aiming to minimize the number of generation-recombination centers. At room temperature field assisted generation,

compared to thermal generation, contributes little to the dark count noise. However field assisted generation becomes the dominant source of the dark counts at temperatures below 200 K due to the suppression of thermally generated charge carriers. Field assisted generation of charge carriers can be reduced only by operating SiPMs at lower operating voltage.

The dark counts are proportional to the volume of the depleted region. Due to this effect SiPMs with smaller cells would result in better dark count rates.

Dark counts have a signal of a single cell or, due to multiple crosstalk, several times higher than a single cell pulse. However it is very unlikely that the dark count process triggers two independent cells simultaneously (Appendix C). Therefore the dark count rate falls rapidly as the threshold increases (Fig. 2.3). Each increase in the threshold for a single cell pulse amplitude decreases the dark count rate for almost an order of magnitude (Fig. 2.3). When the threshold is set to a value of four single cell pulses the dark count rate falls below 1 kHz. Typically dark count rates for SiPMs are below 1 MHz/mm^2. Therefore dark counts limit the use of SiPMs only for applications where a small number of photons needs to be detected.

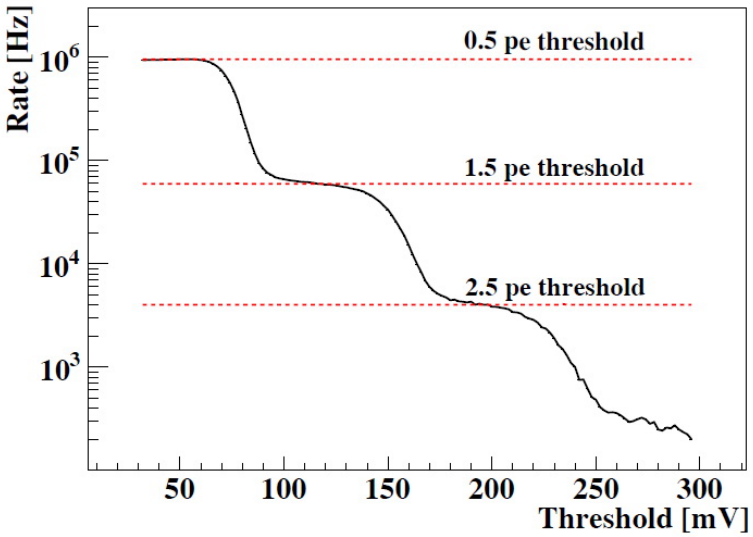

Figure 2.3: Dark count rate of a Hamamatsu MPPC S10326-11-050C operated at V_{OV}= 1.3 V as a function of the discrimination threshold. The noise rates of 0.5, 1.5 and 2.5 photoelectron threshold are indicated by the horizontal lines (taken from (29)).

2.3.2 Crosstalk

During avalanche breakdown on average 3 photons are emitted per 10^5 charge carriers crossing the p-n junction with energy higher than the band gap energy (1.14 eV) (32, 33). These photons are emitted isotropically in the SiPM. As they travel to neighboring cells they can trigger a cell breakdown, which is registered as optical crosstalk (Fig. 2.4). Crosstalk probability is proportional to the overvoltage since the number of secondary photons is proportional to the gain. This effect is additionally enhanced by a large avalanche trigger probability that also increases with overvoltage. In an experiment crosstalk probability can be calculated as the ratio between events with crosstalk (events above 1.5 cell signal) divided by the total number of counts in the dark count spectrum. By means of optical insulation between cells the crosstalk can be significantly reduced, however this affects the PDE (11). Reflective trenches can suppress the crosstalk, however they do not remove the crosstalk process in SiPMs. Significant contribution to the crosstalk comes from the light reflected internally from the bottom of the chip (34). Crosstalk can also be reduced by operating the SiPMs at lower operating voltage or by reduction of the cell capacitance.

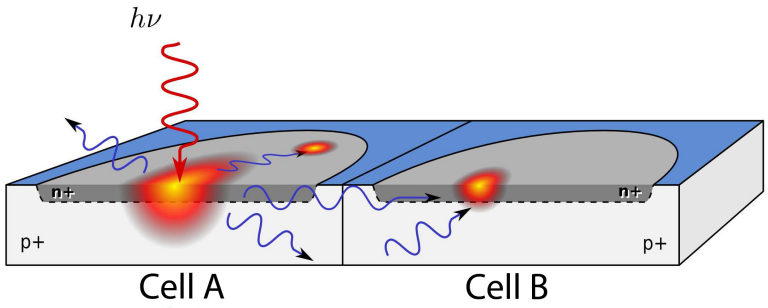

Figure 2.4: Schematic representation of optical crosstalk between two adjacent cells (plot from (34)).

2.3.3 Afterpulses

Afterpulses are generated by electrons, released during avalanche, which are trapped at lattice defects and are released shortly after the avalanche. The time at which the electrons are released varies from nanoseconds up to microseconds. Afterpulse time distribution has two components as shown in Fig. 2.5 (35). One fast, with a time constant of about 15 ns, and one slow, with time constant of 83 ns. Compared to a fully recovered cell, a carrier which is, released while the

voltage is not fully recovered, will have a smaller probability of triggering and will trigger with smaller gain. The fraction of charge created by an afterpulse can be calculated using the recovery time constant (τ_{CRec}) and the time (Δt) by which the afterpulse is delayed (Fig. 2.6)

$$G(\Delta t) = G_0(1 - exp(-\Delta t \cdot \tau_{CRec})).p \tag{2.6}$$

Afterpulses increase with the bias voltage due to the higher gain which results in a larger number of carriers available for trapping. A second effect is the higher avalanche breakdown probability for released charge carriers. Since gain and avalanche trigger probability increase linearly with overvoltage the afterpulse probability increases quadratically.

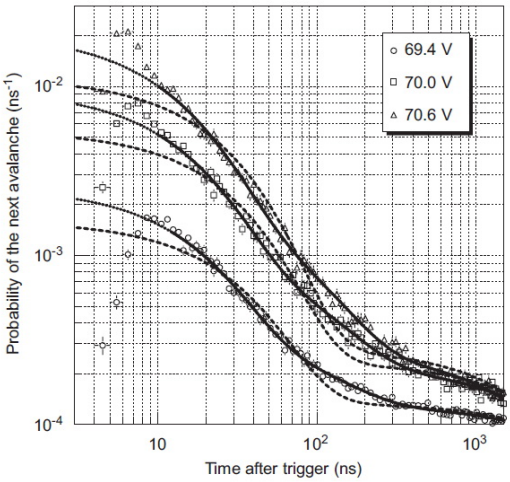

Figure 2.5: Timing distribution of afterpulses for a Hamamatsu MPPC measured at three different bias voltages (taken from (35)).

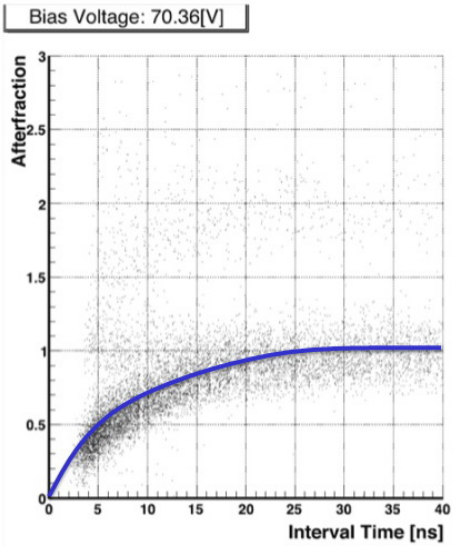

Figure 2.6: Recovery curve of Hamamatsu MPPC with 400 cells/mm^2 (taken from (36)).

2.4 Recovery Time

The cell recovers after discharge with recovery time constant τ_{CRec}. Which is the product of the cell quenching resistance (R_q) and cell capacitance (C_C). Recovery time can vary from a few nanoseconds to microseconds and is temperature dependent due to the use of polysilicon resistors in SiPMs . The recovery process

can be analyzed with help of the afterpulses since they happen in the same cell with some delay after the primary pulse. Waveform analysis is the method typically used (36). Figure 2.6 shows the dependency of the afterpulse amplitude on the delay time after the primary pulse.

2.5 SiPM Nonlinearity

As the SiPM's QE is high the primary limiting factor for PDE is geometrical efficiency which degrades with increasing number of cells. Unfortunately the dynamic range and linearity of SiPMs improves with the number of cells. The response of SiPMs is nonlinear due to the limited number of cells and finite recovery time, which considerably affects the counting capability. The SiPMs signal saturates as the number of incident optical photons in a light pulse multiplied by the photon detection efficiency begins to significantly exceed the the number of cells in a SiPM. Attention has to be paid when using bright scintillating crystals in the detection process, which is the case in modern PET.

2.5.1 Analytical SiPM Model

A simple dependency of the number of triggered cells (N_{Trigg}) on the number of the incident photons in a short light pulse with n_{ph} photons can be described by the differential equation

$$dN_{Trigg}(t) = \frac{N_C - N_{Trigg}(t)}{N_C} PDE \cdot n_{ph} \cdot dt, \tag{2.7}$$

where N_C is the number of cells in a SiPM. The solution of this differential equation, with the boundary condition that in the beginning the number of triggered cells equals zero ($N_{Trigg}(0) = 0$), is

$$N_{Trigg} = N_C \left(1 - e^{-\frac{PDE}{N_C} \cdot n_{ph}}\right). \tag{2.8}$$

This equation includes strong simplifications, since it ignores the finite recovery time of a cell and thus assumes that a cell triggers only once during a scintillation event. Therefore the pulse height is underestimated and better linearity is expected than predicted by the equation. Crosstalk events and afterpulses are also neglected in this approximation. All SiPM cells are subject to crosstalk and afterpulsing, these effects are extremely important as they increase the output

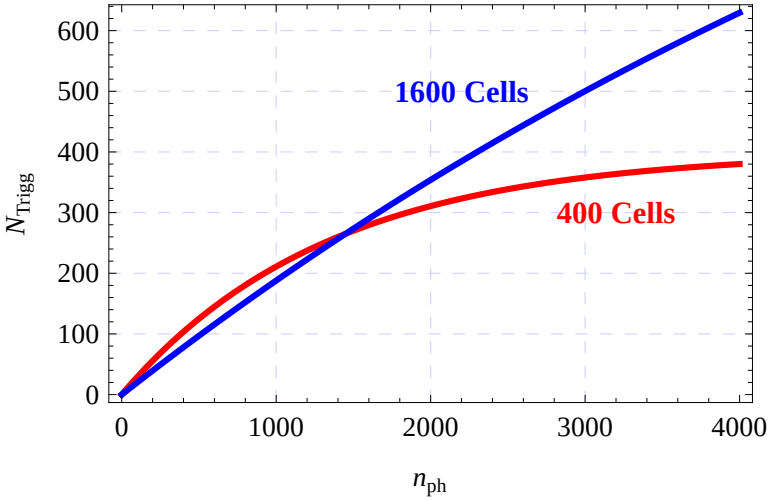

Figure 2.7: Response of SiPMs with 400 or 1600 cells as predicted by equation 2.8. The PDE assumed for the SiPM with 400 cells is 30% and for the SiPM with 1600 cells 20%.

signal and contribute to a higher nonlinear response than expected. Therefore equation 2.8 can only show trends in the SiPM response.

Figure 2.7 shows the dependency of the number of triggered cells on the number of incident photons for a SiPM with 400 and 1600 cells as predicted by equation 2.8. When the number of incident photons times the PDE starts to exceed the number of cells in the SiPM, the saturation of the SiPM dominates the response. The number of triggered cells convergates towards the total number of cells in SiPM for larger number of incident photons, since the recovery process is not included in this simple approach.

2.5.2 SiPM Nonlinearity Correction

In LYSO scintillating crystals about 15000 photons are generated by a 511 keV γ-ray depositing all its energy by photoelectric effect. Only 20% of this photons reach the photodetector (light collection efficiency). However these are still about 3000 photons and at least for SiPMs with 400 cells high nonlinear response is expected as was calculated with the simple SiPM model (Fig. 2.7) and measured with single channel SiPMs (Section 3.6). A simple method described in this chapter can be used to correct SiPMs for nonlinear response.

The dependence of the SiPMs output signal from the amount of the deposited

energy is in the simplest approximation described with an exponential function (Eq. 2.8):

$$V(E) = A\left(1 - \exp\left(-\frac{1}{N_C}\frac{E}{B}\right)\right). \tag{2.9}$$

Where E is the energy deposited in the crystal, N_C the number of cells, and A and B are free parameters. The first order of Taylor expansion of the equation 2.9 was used as an estimate for the linear response of the SiPM (Fig. 2.8)

$$V_{lin}(E) = \frac{A}{N_C B}E \tag{2.10}$$

Solving equation 2.9 for the energy E and inserting it into equation 2.10 yields equation 2.11, which is the resulting formula for the correction of the nonlinear response of the SiPM:

$$V_{corr} = -A\ln\left(1 - \frac{V}{A}\right) \tag{2.11}$$

A schematic presentation of the nonlinearity correction is shown in figure 2.8. This approach allows to correct nonlinearities of the SiPM as well as of the scintillating crystal response.

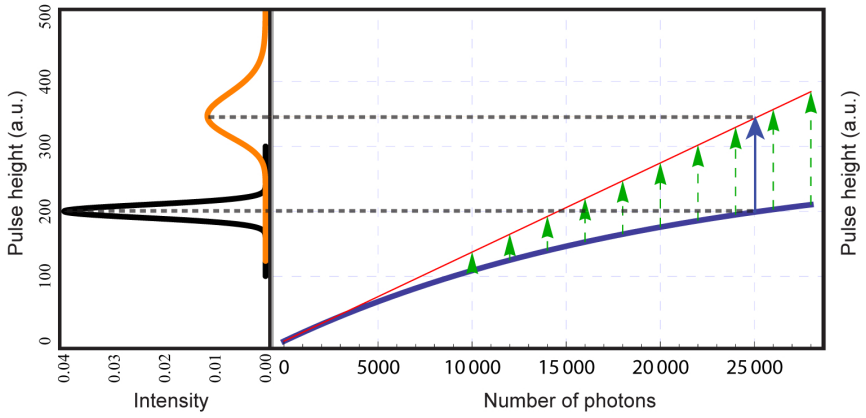

Figure 2.8: Dependency of the simulated SiPM peak position on the number of photons generated by the scintillating crystal is plotted by the blue line. The red line represents the Taylor expansion of the exponential fit of the SiPM response to the first order. On the left axis, an example transformation of a Gaussian representing the photopeak, is presented.

3

Single Channel SiPM Measurements

In this chapter the measurements of single channel SiPMs from Hamamatsu Photonics coupled to a LYSO scintillating crystal from St. Gobain also known under trademark $PreLude^{TM}$ 420 (37) are present. The properties of the LYSO are listed in table 8.2 in chapter 8. The LYSO of $1 \times 1 \times 20\,\mathrm{mm}^3$ is coupled to a SiPM with the matching active area. The scintillation photons generated in the scintillating crystal are emitted isotropically from the point of interaction with the incident radiation. As soon as the incident γ-quanta interacts more than 1 mm away from the photodetector the portion of optical photons hitting the detector without being reflected on their way (direct photons) falls below 5% due to the crystal geometry (Appendix D, solid angle). In order to improve the light collection efficiency, the scintillating crystal was wrapped in a 3M specular reflector foil (38) and coupled to the photodetector by means of optical adhesive with a refractive index of 1.6 (DELO-PHOTOBOND^{TM} 400 (39)). Two different types of SiPMs from Hamamatsu Photonics were investigated: S10362-11-050C and S10362-11-025C. Each of them with $1 \times 1\,\mathrm{mm}^2$ effective sensitive area, matching the LYSO crystal one-to-one. In figure 3.1 a picture of S10362-11-050C is shown. The S10362-11-050C has a cell size of $50\,\mu$m resulting in $400\,\mathrm{cells/mm}^2$, while S10362-11-025C has a cell size of $25\,\mu$m and $1600\,\mathrm{cells/mm}^2$.

Table 3.1 summarizes the relevant parameters of both devices for a certain overvoltage. The Hamamatsu data sheet (24) shows that the PDE of the SiPM S10362-11-025C, S10362-11-050C and S10362-11-100C at the recommended operating voltage at its maximum sensitivity is about 25%, 53% and 65% respectively. It should be noted that this data include crosstalk and afterpulses. The actual

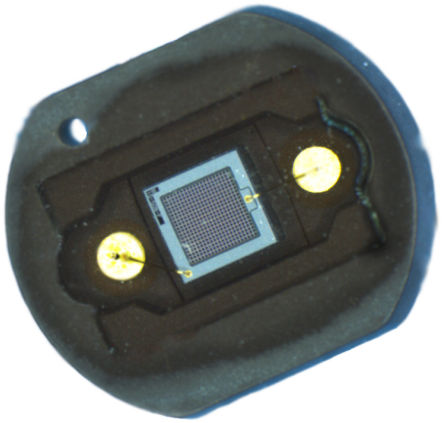

Figure 3.1: Photo of the Hamamatsu MPPC S10362-11-050C with sensitive area of $1 \times 1\,\mathrm{mm}^2$ with surrounding plastic structure and bond wires.

PDE of Hamamatsu SiPMs is therefore smaller (Table 3.1). In general, a SiPM with 1600 cells can be operated at higher overvoltage as a SiPM with 400 cells. While the SiPM with 400 cells has a higher photon detection efficiency of about 10% (29) compared to the version with 1600 cells due to its better fill factor, it suffers from nonlinearity because of a smaller number of cells. A SiPM with 400 cells has slightly higher crosstalk probability compared to the version with 1600 cells due to its higher gain. The recovery time and the decay time of a single cell

SiPM type	S10362-11-100C	S10362-11-050C	S10362-11-025C
N_C	100	400	1600
PDE	35%	30%	20%
p_{SAP}	8%*	8%	8%
τ_{SAP}	15 ns*	15 ns	15 ns
p_{LAP}	9%*	8%	7%
τ_{LAP}	80 ns*	80 ns	80 ns
p_{CT}	20%*	15%	10%
δ	3 ns*	2 ns	1 ns
τ_{CDec}	20 ns*	11 ns	5 ns
τ_{CRec}	15 ns*	9 ns	4 ns
DCR	500 kHz*	700 kHz	700 kHz

Table 3.1: Parameters of SiPMs (Hamamatsu MPPC) with 100, 400 and 1600 cells/mm^2 measured at $1p.7\,\mathrm{V}$, $2.7\,\mathrm{V}$ and $3.3\,\mathrm{V}$ overvoltage respectively (24, 29, 35, 36, 40) at room temperature. * Values are assumptions.

pulse are related to the RC time constant of the SiPM (Chapter 2). Measurements at different operating voltages for both SiPMs coupled to LYSO crystals with different radioactive sources were performed. Radioactive sources used in the measurements are listed in table 3.2. The goal of this study was to find the optimal operating voltage for both SiPM types in order to optimize energy resolution when coupled to the LYSO. The performance of the SiPM with 400 and 1600 cells/mm^2 coupled to LYSO were compared in terms of energy resolution.

Measurements were performed at room temperature with a digital oscilloscope (Infiniium 54832D, Agilent Technologies, Santa Clara, California, U.S.A.) which samples the signal at 4 GHz. The signals were analyzed using the signal height detection method. Energy spectra from the signal heights were recorded and fitted with two Gaussian functions, where one Gaussian fits the Compton edge and the second the photopeak (Fig. 3.2).

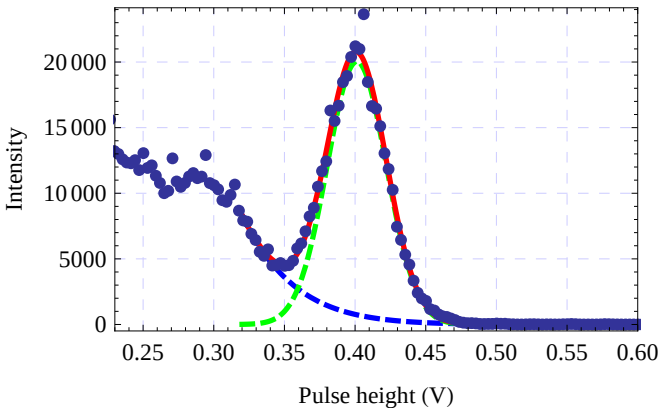

Figure 3.2: Measured spectra of the SiPM with 400 cells coupled with $1 \times 1 \times 20\,\text{mm}^2$ LYSO crystal at room temperature. Bias voltage used was 70.5 V. The green dashed line represents the Gaussian fit of photopeak, the blue line the fit of the Compton edge and the red line the sum of both Gaussians.

3.1 Peak Position Dependency on Bias Voltage

The position of the ^{18}F photopeak in the spectra measured with LYSO-SiPM is proportional to the number of triggered cells and to the gain of the SiPM. The number of triggered cells and the gain increase linearly as the bias voltage increases. Therefore the LYSO-SiPM module has a quadratic dependence of the photopeak position on the bias voltage. The photopeak position dependence of

Isotope	$E(MeV)$	$t_{1/2}$
^{57}Co	122	271.8 days
^{99m}Tc	142	6.01 hours
^{133}Ba	356	10.5 years
^{131}I	364	8 days
^{18}F	511	109.8 minutes
^{137}Cs	662	2 years

Table 3.2: Radioactive sources and their properties.

the LYSO-SiPM signal on the bias voltage was fitted with $A + B(V - V_0)^2$, where A, B and V_0 are free parameters of the fit (Fig. 3.3, 3.4).

Figure 3.3 shows the dependency of the photopeak position of the LYSO-SiPM module on the bias voltage for six radioactive sources for SiPM with 400 cells/mm^2. The experimental data correspond well with the quadratic fit model. Results of fits with coefficients of determination are collected in table B.1. The last three points in the plot of the LYSO-SiPM photopeak position for ^{18}F have wrong values due to the higher temperature during the measurement. As the temperature increases the breakdown voltage increases which results in lower gain and PDE at the same bias voltage.

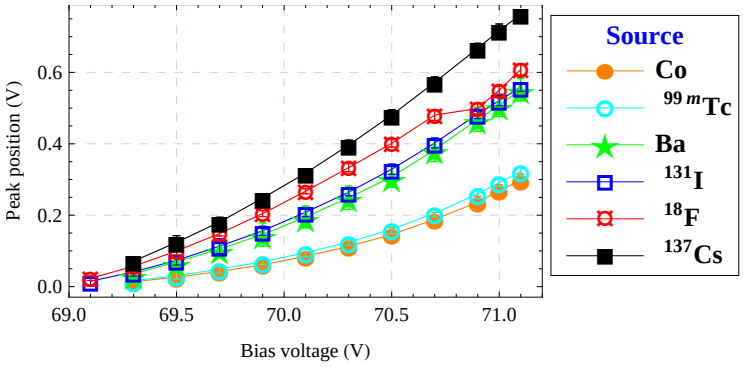

Figure 3.3: Dependency of the peak position on the bias voltage of the SiPM with 400 cells coupled to the LYSO crystal measured with different radioactive sources.

Figure 3.4 visualizes the dependency of the photopeak position on bias voltage for six radioactive sources for SiPMs with 1600 cells/mm^2. The results of the fits are collected in table B.2. Again good agreement between experimental data and quadratic fit model is observed.

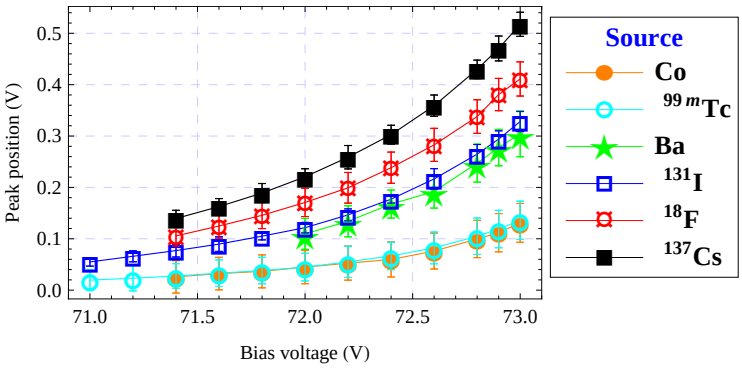

Figure 3.4: Dependency of the peak position on bias voltage of SiPMs with 1600 cells coupled to LYSO crystal measured with different radioactive sources.

Despite the fact that the gain of the SiPM with 400 cells/mm^2 is about 2.7 times as high as that of the SiPM with 1600 cells/mm^2 and the PDE is about 1.5 times as high, the peak position for both devices when coupled to LYSO shows a smaller difference. Simple calculation gives $1.5 \times 2.7 = 4.05$, where from measurements (figures 3.3 and 3.4), a quotient of about $0.22\,\mathrm{V}/0.16\,\mathrm{V} = 1.37$ is observed for ^{18}F at 70.1 V for 400 cells/mm^2 and at 72.0 V for 1600 ceills/mm^2. This is due to the fact that the SiPM with 1600 cells/mm^2 offers more cells which fire with smaller amplitude but as more of them fire under stronger illumination they can produce signals almost as high as that of the SiPM with 400 cells/mm^2. On the other hand the 400 cells/mm^2 version is also quickly saturated. If we do the same calculation for ^{99m}Tc, for the same voltages as in previous calculation, we get larger value for the quotient of the peak positions $0.08\,\mathrm{V}/0.04\,\mathrm{V} = 2$, due to the smaller number of impinging photons on the SiPMs .

3.2 LYSO-SiPM Nonlinearity

The nonlinear behaviour of the SiPM is corrected according to the method described on page 13. The nonlinear correction was performed with measurements of the response of the LYSO-SiPM detector module to incident γ-rays emitted from different radiation sources (^{57}Co, ^{99}Tc,^{133}Ba,^{131}I,^{18}F,^{137}Cs) listed in table 3.2. The results can be seen in Fig. 3.6 and 3.7. Figure 3.5 shows a typical spectra of a SiPM coupled to a LYSO, measured with the ^{18}F, before and after the correction for nonlinear effects.

Nonlinearity increases with increased bias voltage since the PDE, dark counts,

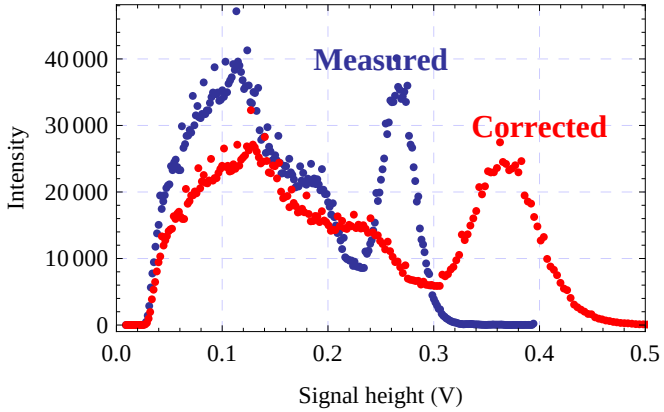

Figure 3.5: Measured spectra for a SiPM with 400 cells/mm^2 coupled to a LYSO crystal at 70.1 V at room temperature. Radioactive source was ^{18}F. Energy resolution without correction for nonlinear effects of 14% becomes in reality 21% after the correction.

crosstalk and afterpulse probability increase with applied voltage. Much stronger nonlinearity is observed in the case of the SiPM with 400 cells/mm^2 due to the 4-times smaller amount of cells but larger PDE compared to the SiPM version with 1600 cells/mm^2. High nonlinearity is measured for a SiPM with 400 cells/mm^2, which needs to be taken into account for energy resolution studies. The fitted parameter B from equation 2.9 represents the degree of nonlinearity of the detector module. Experimental values of parameter B depending on the bias voltage are presented in figures 3.8 and 3.9. As expected the parameter B decreases with bias voltage and is in general much higher for the SiPM with 1600 cells/mm^2. Parameters of the LYSO-SiPM response (Eq. 2.9) and the coefficient of linear response (k) calculated with Taylor expansion of the exponential fit to the first order are presented in table B.1 and B.2. The values of parameter B obtained with the SiPM with 1600 cells have a larger error due to the instability of the fit, since the detector shows almost linear response. After the correction of nonlinear effects direct comparison of the energy resolution for the SiPM with 400 and 1600 cells is possible.

3.3 Energy Resolution Dependency on Bias Voltage

The energy resolution is defined as the full width of photopeak at half maximum (FWHM) divided by the peak position and is an important parameter of any PET detector. In PET applications energy information allows to reduce the number of

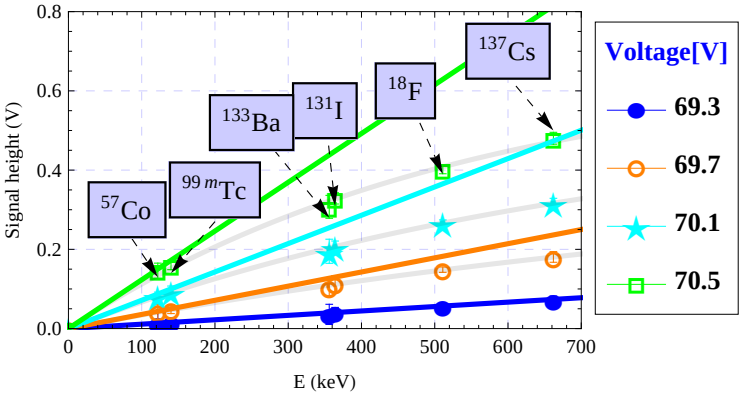

Figure 3.6: Dependency of the signal peak position from the deposited energy in the LYSO for the SiPM with 400 cells/mm^2 coupled with the LYSO crystal at different bias voltages. Gray lines represent the exponential fit to the measured data, while solid-coloured lines represent the Taylor expansion of the exponential model to the first order.

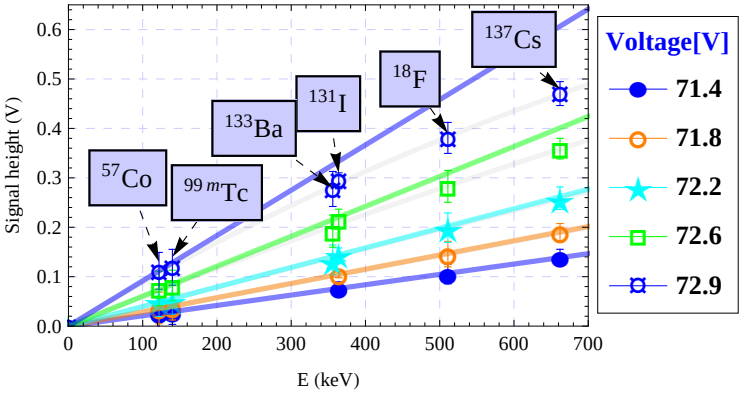

Figure 3.7: Dependency of the signal peak position from the deposited energy in the crystal for the SiPM with 1600 cells/mm^2 coupled with the LYSO crystal at different bias voltages. Gray lines represent the exponential fit to measured data, while solid-coloured lines represent the Taylor expansion of the exponential model to the first order.

detected γ-rays which underwent a Compton scattering process in the patient and would result in false lines of response (LOR) and contribute to the background noise in the image. The energy resolution of the LYSO-SiPM module depends on the number of generated scintillating photons and the property of the detector to convert the photons into a measurable signal. The number of detected photons in SiPM increases with bias voltage where the statistical error decreases. However

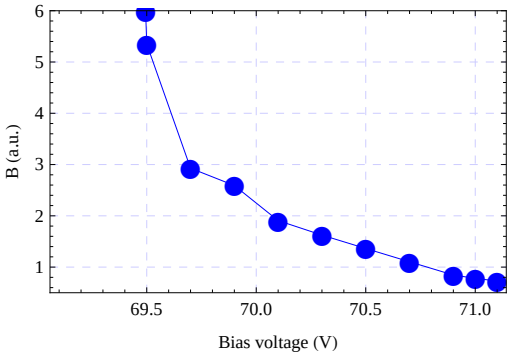

Figure 3.8: Measured dependency of the parameter B on the bias voltage for the pulse height method for the SiPM with 400 cells/mm^2).

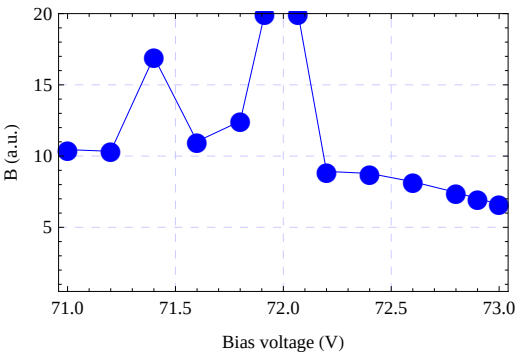

Figure 3.9: Measured dependency of the parameter B on the bias voltage for the pulse height method for the SiPM with 1600 cells/mm^2.

the noise originating from crosstalk, afterpulses and dark counts increases as well with bias voltage. Another important aspect of LYSO-SiPM energy resolution is nonlinearity, which also increases with the bias voltage as was explained above. Due to the combination of these effects there is an optimal bias voltage for the best energy resolution.

Figure 3.10 shows the dependency of the energy resolution on the bias voltage for a SiPM with 400 cells/mm^2. Strong improvement of the energy resolution with increased bias voltage is misleading due to the nonlinear response of the SiPM. SiPM signals have to be corrected for the nonlinear effects as described on page 13. The parameters required for the nonlinearity correction are presented in table B.1 and B.2. The energy resolution of the SiPM with 400 cells/mm^2 corrected for nonlinear effects can be seen in figure 3.11. The SiPM with 400 cell/mm^2 in combination with LYSO has a near constant broad minimum in the function of energy resolution versus bias voltage. Within the errors of the measurement we conclude that SiPM (400 cells/mm^2) coupled with LYSO results in 20% energy resolution for bias voltages between 69.3 and 70.7 V for ^{18}F.

The improvement of the statistical error compensates the noise due to the nonlinearity and energy resolution stays at a value of about $20 \pm 2\%$ for a SiPM with 400 cells/mm^2. The measurements with ^{137}Cs reach the best energy resolution at lower operating voltages, due to the higher energy of the emitted γ-rays from ^{137}Cs (Tab. 3.2). At voltages above 70.7 V very strong degradation of the energy resolution measured with ^{137}Cs source is observed due to saturation of the SiPM. Measurements with low energetic γ-rays (^{57}Co, ^{99}Tc) show strong

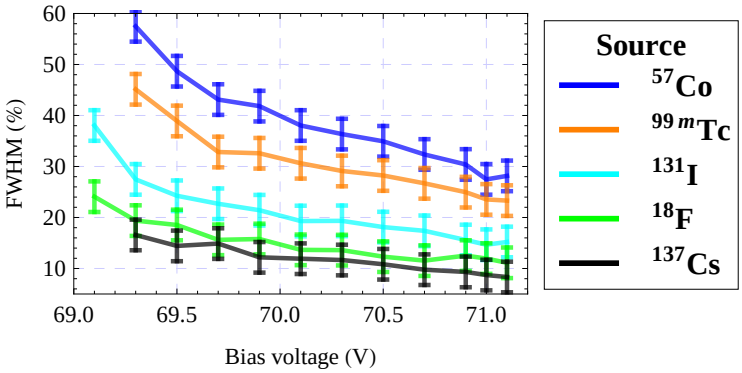

Figure 3.10: Dependency of the energy resolution on bias voltage for the SiPM with 400 cells/mm^2.

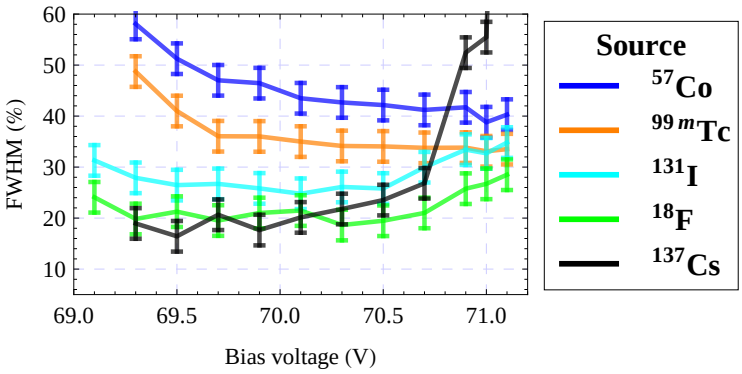

Figure 3.11: Dependency of the energy resolution on bias voltage for the SiPM with 400 cells/mm^2 corrected for nonlinear effects.

degradation of the energy resolution after correction for nonlinearity at higher operating voltages. The reason for this is partially in the increase of the PDE with the bias voltage but mostly due to the increase of the crosstalk. Optimal operating voltage for ^{57}Co and ^{99}Tc is above 71.1 V (Fig. 3.11).

The SiPM with 1600 cells/mm^2 coupled with LYSO has an energy resolution of about 22±2% in a wide range. The energy resolution does not change significantly after the correction for nonlinear effects, only when using ^{137}Cs small degeneration at higher bias voltages is observed.

The measured energy resolution for both cell densities could be improved for about 2% with better optical coupling and wrapping in reflector foil which results in better light collection efficiency (best results we could produce, (41)). However the process of coupling and wrapping in reflector foil was done by hand, which is

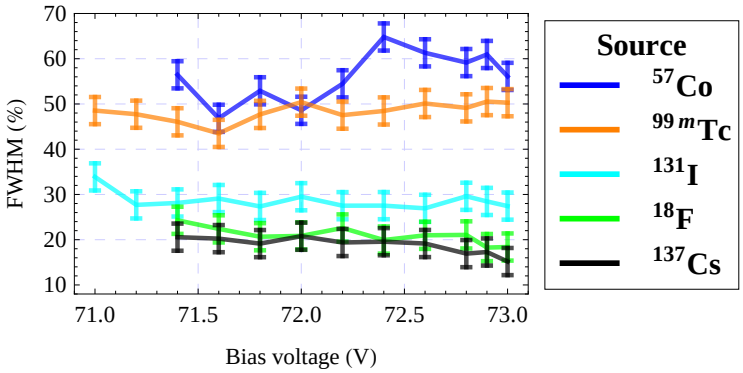

Figure 3.12: Dependency of the energy resolution on bias voltage for the SiPM with 1600 cells/mm^2 .

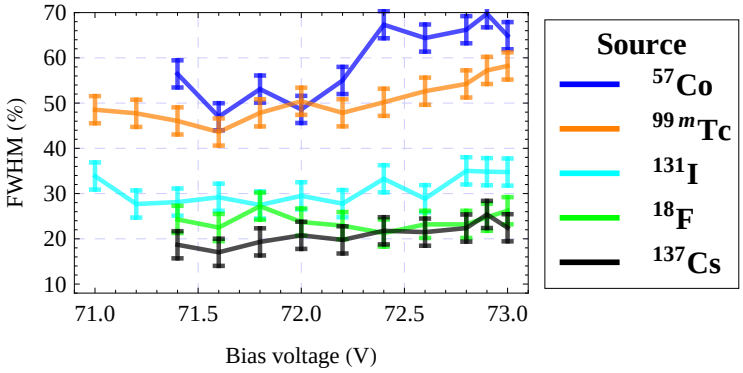

Figure 3.13: Dependency of the energy resolution on bias voltage for the SiPM with 1600 cells/mm^2 corrected for nonlinear effects.

difficult to do accurately for the crystal and the SiPM of our dimensions.

3.4 Conclusion

High nonlinearity of the SiPM with 400 cells/mm^2 when coupled to the LYSO was observed when operating the detector at the manufacturer recommended bias voltage for the PET/MR. This implies the need for a correction of the SiPMs signal for energy resolution studies. After the correction of the nonlinearity the optimal bias voltage for SiPMs for measurements with different radionuclides was extracted. After the correction of nonlinear effects the direct comparison between the energy resolution of the SiPM with 400 and 1600 cells/mm^2 could

also be performed. This comparison shows a better energy resolution of the SiPM with 400 cells, for combined PET/MR, when coupled to a $1 \times 1 \times 20\,\mathrm{mm}^3$ LYSO scintillating crystal. The best energy resolution of $18 \pm 2\%$ is measured with the SiPM with $400\,\mathrm{cells/mm}^2$ at $70.3\,\mathrm{V}$. The best energy resolution obtained with the SiPM with 1600 cells of $22 \pm 2\%$ is at $72.5\,\mathrm{V}$ bias voltage.

A comparison of this measurements with other groups is difficult due to the unique LYSO-SiPM configuration investigated by our group. There are many parameters which affect the energy resolution but are difficult to control: quality of the crystals, surface treatment, wrapping of crystals in the reflective material and optical coupling. There are different SiPMs on the market, working at different bias voltages, having different gains, dark count rates, etc. How can different devices be compared? Should they be measured at the same overvoltage or at the same gain? Which temperature should be used for the measurements? A standardized protocol for SiPM energy resolution measurements still does not exist, and at the moment each group is using their own protocols. Therefore the comparison between different measurements is only quantitative. Song et al. (42) have the detector module similar to the one presented in this work. They measured a $20 \pm 5\%$ energy resolution for the SiPM with 400 cells coupled to a LYSO crystal of $10 \times 10 \times 0.8\,\mathrm{mm}^3$ which is in accordance with the measurements presented.

4

Measurements with SiPM Matrix

Until now widely used continuous slab concept where one large scintillating crystal is readout by many detectors determines the interaction position of the γ-ray with centre of gravity algorithms. However the development of semiconductor detectors like APDs and SiPMs with their small size and high granularity allow the attachment of a small single crystal directly to one single readout detector. This so called one-to-one coupling configuration offers a very good spatial resolution which is only limited by the crystal size, and accounts for higher count rates than the continuous slab concept. The main disadvantage of one-to-one coupling is in the degradation of the sensitivity due to the reflector which has to be placed between the crystals to prevent optical crosstalk. Another disadvantage is that the number of readout channels increases rapidly which has first to do with the complexity of the system and secondly larger cost which is mainly connected with expensive readout electronics.

The subject of the investigation presented in this section was a 4×4 SiPM matrix consisting of 4 monolithic rows of 1×4 single channel SiPMs ($1 \times 1\,\mathrm{mm}^2$ each) placed on a common substrate (Hamamatsu MPPC S10984). Two different configurations were studied, one with 50 ($400\,\mathrm{cells/mm}^2$) and other with $25\,\mu\mathrm{m}$ ($1600\,\mathrm{cells/mm}^2$) cell size (Fig. 4.1). The gap between the adjacent channels inside the 1×4 row can be neglected. However there is a 1.5 mm gap between the adjacent 1×4 rows. This gap is used for the readout lines of the individual channels. The gap could be smaller than 1.5 mm, but the extra large gap in the design allows alternating readout of the crystal block of 32 crystals with two SiPM matrices from the upper and lower side with minimal dead space in between the crystals (Fig. 4.3).

The complete SiPM matrix is glued and wire-bonded on a ceramic carrier of

$4.9 \times 10.2 \times 0.9\,\mathrm{mm}^3$ which is mounted on a custom-made printed circuit board (PCB) that gives support and bias (Fig. 4.2). The PCB is directly connected to the readout electronics board (SADC, (43)). A common bias voltage is applied to each row (4 SiPM channels). An epoxy layer of 0.3 mm covers the channels and protects the surface of the SiPMs as well as the bonding wires, resulting in a total thickness of the matrix of 1.45 mm.

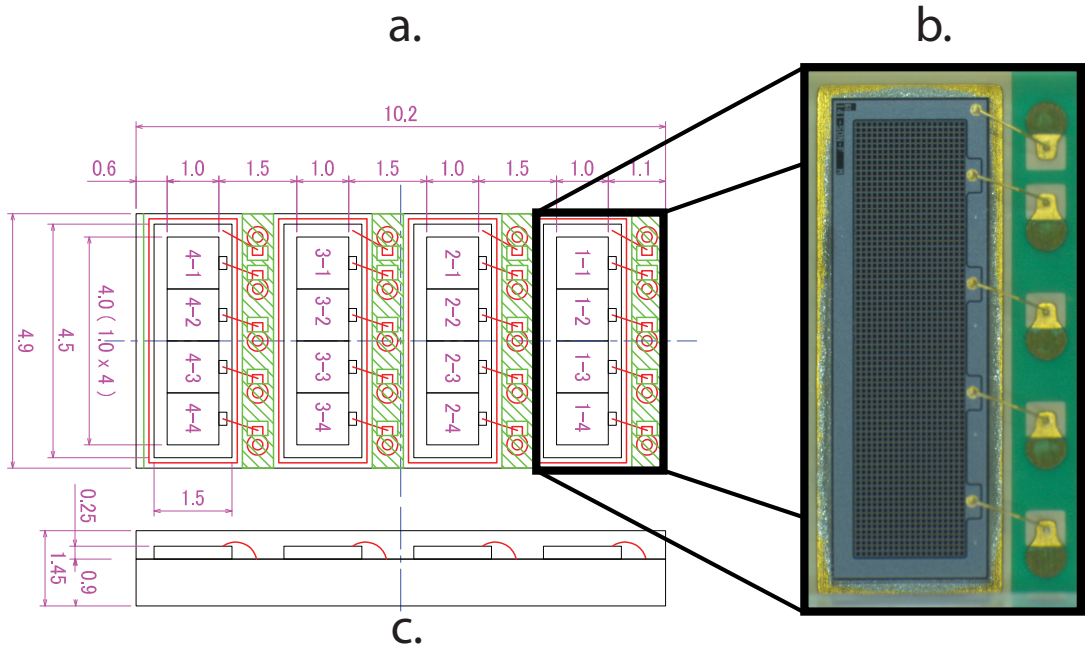

Figure 4.1: a.) A schematic representation of the 4×4 SiPM matrix from Hamamatsu Photonics (top view). b.) A picture of one 1×4 SiPMs line (MPPC S10984). c.) A schematic representation of SiPM array (side view). All dimensions are in mm.

The SiPM matrix was lit with very short (30 ps FWHM) optical pulses from an Advanced Laser Diode System Picosecond Injection Laser with a wavelength of 404 nm. The light intensity from the laser pulse was controlled by a set of neutral density filters with different transmission coefficients. The resulting laser light was conducted to the detector which was mounted on a special holder in a light-tight box, via an optical fibre. The box also shields the SiPM from electrical noise. The detector was positioned on a table which could be moved in the x, y and z direction with high precision (1 μm). The movement of the detector was controlled with a PC. Units of the movement in all three directions are measured in units where one unit represents movement of the axis for 0.3595 μm.

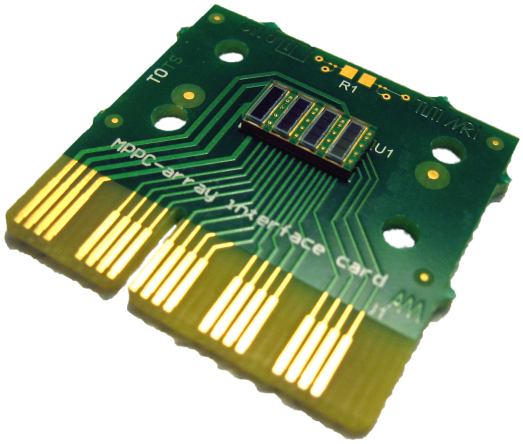

Figure 4.2: The SiPM array mounted on a custom made PCB board.

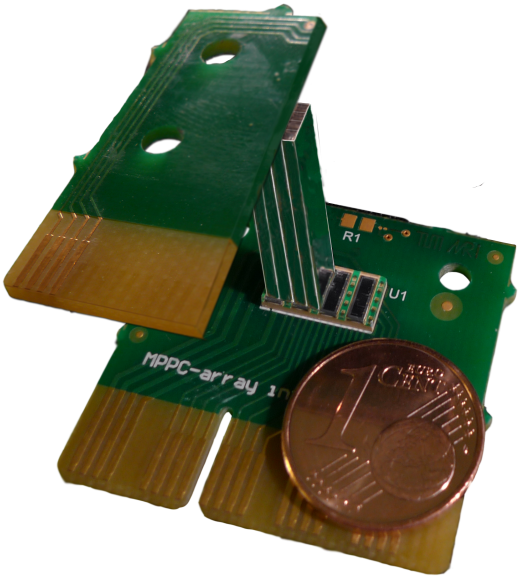

Figure 4.3: Combination of two arrays with alternating frontside-backside readout to avoid dead space.

X and y direction enabled a scan over the entire surface of the detector, while the movement in the z direction enabled the control of the laser spot size on the detectors surface, which was about 10 μm when the laser beam was in focus. The output of the SiPM matrix was amplified by an EG&G ORTEC FTA820, and later split into two parts: one fed to an analog-to-digital charge converter (LeCroy 2249A ADC) and the other to another EG&G ORTEC FTA820 amplification to a multihit TDC unit (CAEN V763A) which is controlled via Wiener PCIADA by the National Instruments LabWindows program running on the PC. Data acquisition was triggered by a delayed pulse from the laser unit. For each hit, the time of arrival as well as collected charge and position of the particular photon detector channel was measured. Temperature was monitored but not controlled, hence the temperature during the measurement varied by about 1 K. Figure 4.4 shows the schematic presentation of the setup.

The signal of the SiPM array was directly readout by an Oscilloscope (Tektronix , DPO7000) which was triggered by the delayed laser unit signal or by a threshold level set to the SiPM signal.

Figure 4.5 shows the response of the SiPM to the pulsed light source irradiating the whole surface of the detector. Due to the high gain of SiPMs there are

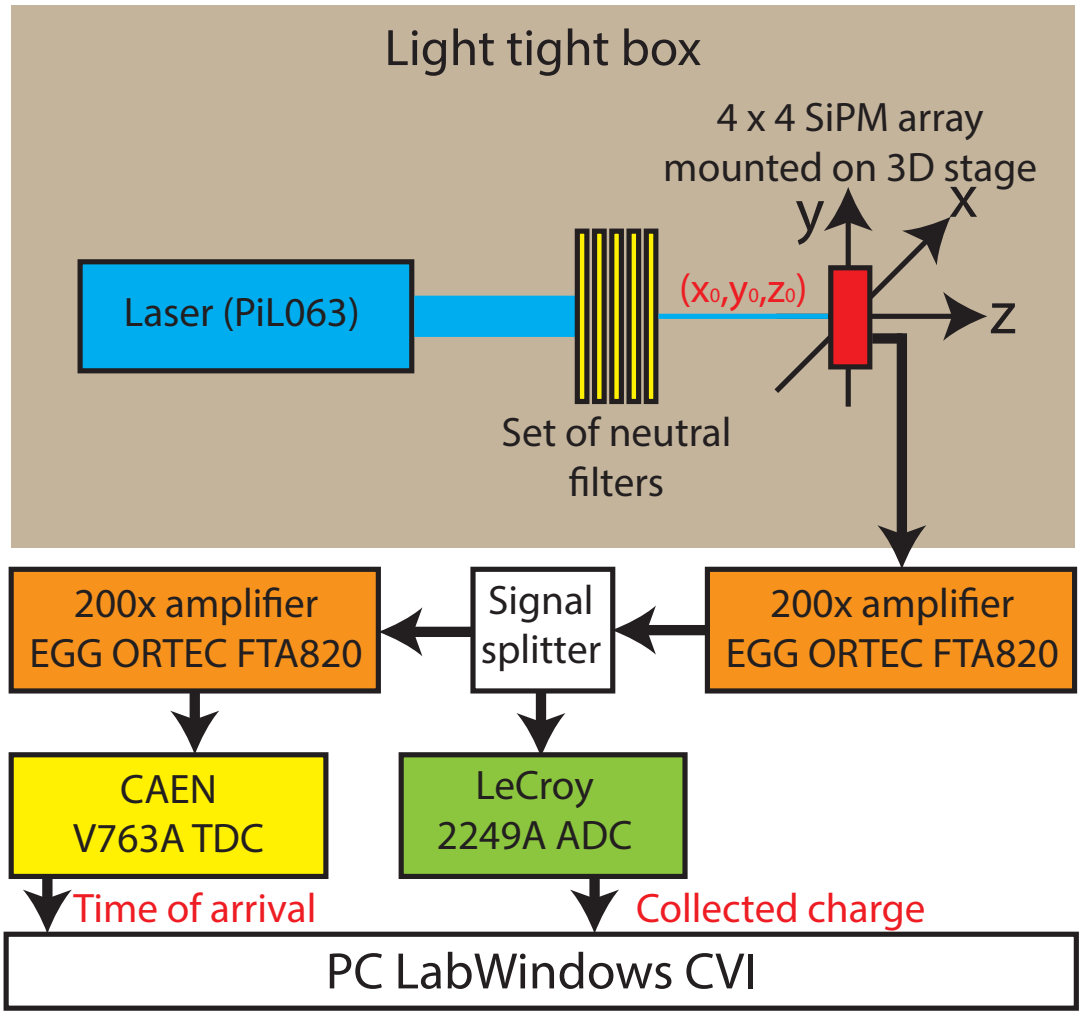

Figure 4.4: Schematic representation of the experimental setup.

measurable signals observed on the oscilloscope without the amplification. Signals for different numbers of triggered cells are well separated from each other, thus offering the possibility for single photon counting. Good separation of single cell pulses implies good gain uniformity for the whole SiPM.

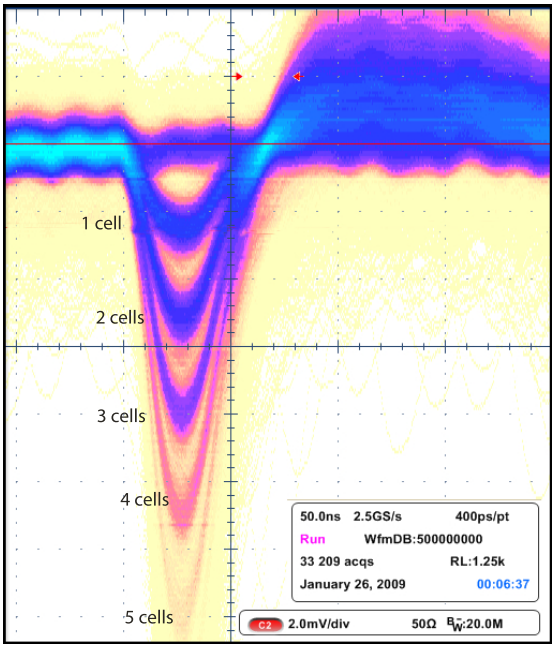

Figure 4.5: The single cell pulses response of the SiPM array with 25 μm cell size to the pulsed light source ($\lambda = 404$ nm) of low light intensity.

4.1 Positioning the SiPM Matrix in Focus of the Laser

A laser beam has a spatial profile which can be well approximated by Gaussian functions. The spot size of the beam will be at a minimum value somewhere along the beam axis. In studies where the beam size matters one has to position the detector at a distance where the laser beam has its waist. In order to find this position the SiPM was scanned by single photon pulses. The detector was scanned along a line moving across the edge of the channel 1-3 and the number of avalanches for each position was measured (Fig. 4.6). The threshold level for the collected charge was set above the noise of the electronics but below the charge collected by the single cell pulse (at about 50% of the charge produced by a fully recovered cell). Each position was measured for 5 s and the laser was triggered with a frequency of 2 kHz. The measured sensitivity profile as a function of the position of the detector was fitted with

$$N_0 + A \cdot erf(\frac{x-\mu}{\sqrt{2}\sigma}) \tag{4.1}$$

where x represents the coordinate in x direction, μ represents the position of the edge of the cell, N_0 represents the background counts and σ measures the width of the distribution which is proportional to the spot size of the laser beam at the detectors surface.

The dependency of the width of the sensitivity curve (σ) on the position of the detector on the beam axis (z) has a minimum at 29500, therefore the detector is in the focus of the laser beam at this position (Fig. 4.7).

It is important to maintain the laser in the focus over the whole surface of the SiPM matrix. This was achieved with precise assembling of the SiPM matrix to be parallel to the x and y direction of the movable table.

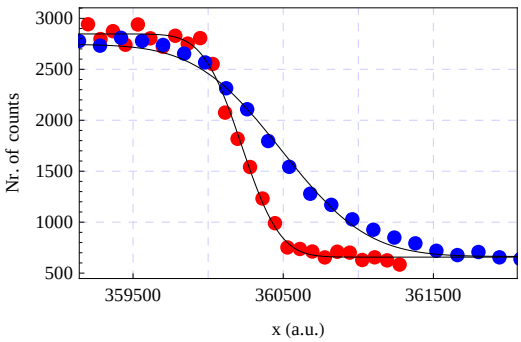

Figure 4.6: Dependency of the sensitivity profile of the SiPM with 400 cells/mm^2 from the x-coordinate for two positions of the detector on the beam axis separated by 71.9 μm (blue $z = 32000$, red $z = 30000$).

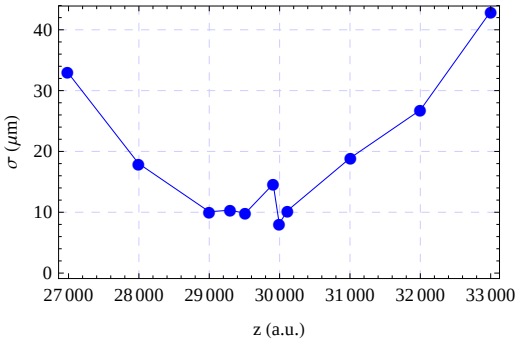

Figure 4.7: Dependency of the width of the sensitivity profile on the position of the SiPM matrix with 400 cells/mm^2 on the beam axis.

4.2 Pulse Height Dependency pon the Bias Voltage

When a cell in the SiPM breaks down a standardized signal is produced. Charge produced during breakdown is proportional to the cell capacitance (C_C) and overvoltage. The single cell gain increases therefore linearly with overvoltage.

The signal amplitude (A_i) is proportional to the capacitance of the cell (C_C) divided by the electron charge (q_0) multiplied by the overvoltage.

$$A_i \propto \frac{C_C}{q_0}(V_{Bias} - V_{BD}) \tag{4.2}$$

The SiPM matrix with 400 cells/mm^2 was placed in the focus of the laser beam and irradiated with single photons. The SiPM signals were directly fed to the oscilloscope and analysed with the pulse height detection method (oscilloscope). The response of the SiPM matrix to single photons can be seen in figure 4.8. Here single cell pulses (1 cells) and pulses with crosstalk event (2 cells) can be seen. Figure 4.9 shows the dependency of the signal height of the single cell pulses on the bias voltage for the SiPM matrix with 400 cells/mm^2. As expected linear increase of the pulse height with applied voltage which saturates at higher voltages is observed. A linear interpolation of the pulse height as a function of operating voltage can be used to determine the breakdown voltage. The breakdown voltage is determined at the point where a linear fit intersects with the x axis.

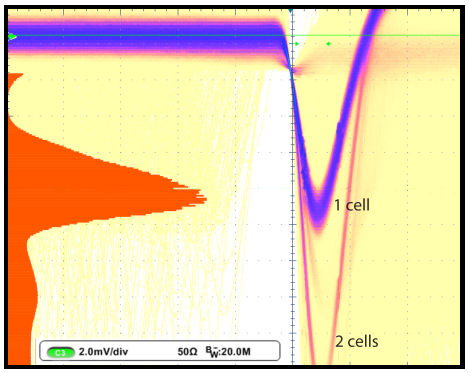

Figure 4.8: The single cell pulses and the single cell pulses with crosstalk for SiPM with 400 cells/mm^2.

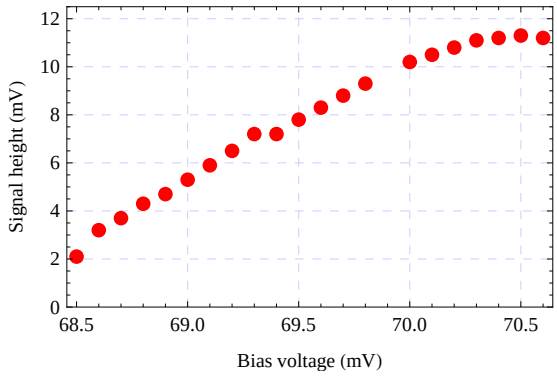

Figure 4.9: The single cell pulse height as function of bias voltage for channel one in SiPM matrix with 400 cells/mm^2. Calculated breakdown voltage is at 68.1 V.

4.3 Gain Uniformity Between Channels in the SiPM Matrix

The laser beam with low light intensity was moved along the centre of 16 channels in the SiPM matrix, and the pulse height of a single cell was measured for each channel (oscilloscope). The detector was placed in the focus of the laser beam. Each channel was operated at the prescribed bias voltage given by the manufacture. The temperature was at room temperature during the time of the measurement. The results are presented in figure 4.10, where good uniformity

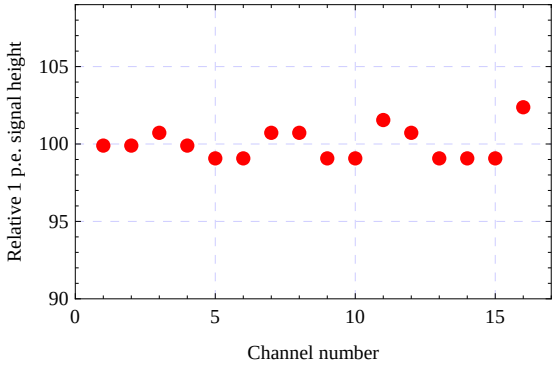

Figure 4.10: The relative Gain in the SiPM array with 400 cells/mm^2.

between the channels in the SiPM array is evident. About 3% variation in the collected charge between the channel with highest and lowest gain was measured.

4.4 Pulse Height Dependency on Incident Light Intensity

The laser beam was positioned at the centre of the SiPM channel 2-3 with 400 cells/mm^2 (Fig. 4.1) and 1600 cells/mm^2. The laser beam was out of focus at the surface of the SiPM and evenly illuminated the whole surface of the SiPM. The signals from SiPM were preamplified by a factor of about 200 and readout by the oscilloscope which was triggered by the delayed laser signal. The amount of light impinging on the SiPM was controlled by optical filters placed between the SiPM and the laser beam (transmission). The response of the SiPM to different light intensities was observed. The signal was averaged and recorded with the oscilloscope from which the pulse height was determined and plotted versus the transmission. The channel 2-3 in the SiPM array with 400 cells/mm^2 quickly underwent total saturation (Fig. 4.11) while the SiPM with 1600 cells/mm^2 saturates at higher light intensities (Fig. 4.12). At high light intensities all cells in the SiPM are triggered and always produce a signal with the same amplitude, however if there are still photons impinging on the detector after the cells have recovered they can again contribute to the signal (Fig. 4.13). The SiPM with 1600 cells/mm^2 saturates at higher light intensities not only due to the four times larger number of cells, but also due to the lower photon detection efficiency, faster recovery time and lower gain which results in lower crosstalk and afterpulse probability (Tab. 6.1). It has to be noted here that the number of photons impinging

on the observed SiPM channel may slightly differ in the case of the SiPM matrix with 400 from the 1600 cells/mm^2. This is due to the inaccuracy of the position of the SiPM matrix in the measured setup, which occurs when changing the detector.

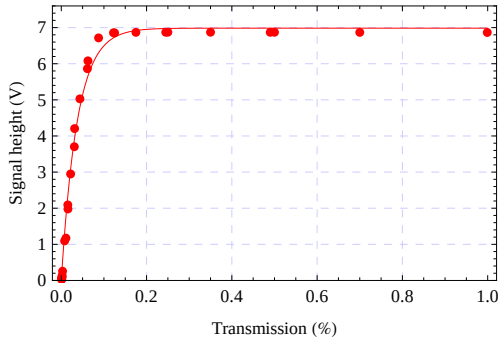

Figure 4.11: Dependency of the pulse height on the transmission for channel 2-3 in SiPM matrix with 400 cells/mm^2

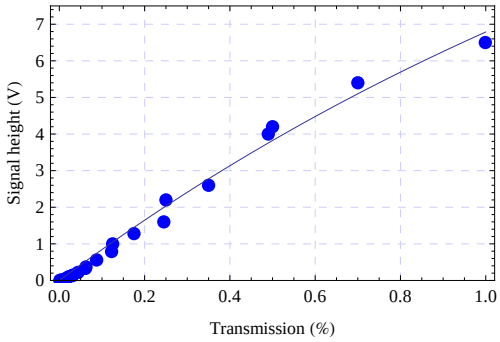

Figure 4.12: Dependency of the pulse height on the transmission for channel 2-3 in SiPM matrix with 1600 cells/mm^2

4.4.1 2D Uniformity Scan

The position dependency of the SiPM sensitivity for single photons (Fig. 4.14, 4.15) was investigated for the SiPM with 400 cells/mm^2. A single photon laser beam with a spot size of about 10 μm and λ = 404 nm was moved across the surface of the SiPM channel 2-3. The position dependent variation of the sensitivity shows the surface structure of the measured device . The SiPM response is fairly constant for different cells (Fig. 4.14), but there is more variation within the individual cells (Fig. 4.15). The loss of the sensitivity due to the quenching resistor and readout lines placed around cells can be clearly seen (Fig. 4.15).

The variation in the collected charge between single cells in one channel of the SiPM array was calculated by averaging the collected charge from the data acquisition for the positions near the centre of each cell. A variation in charge of about 1.5% was observed. A large contribution to this is due to the temperature variation during the measurement (Fig. 4.16). That was mainly due to the night-day temperature change. The measured charge was corrected with a simple linear model as described in (44). A reference temperature of 25 $^{\circ}C$ was taken. The charge that was measured at temperatures lower than 25 $^{\circ}C$ was higher due to temperature effects and vice versa. By applying different temperature coefficients,

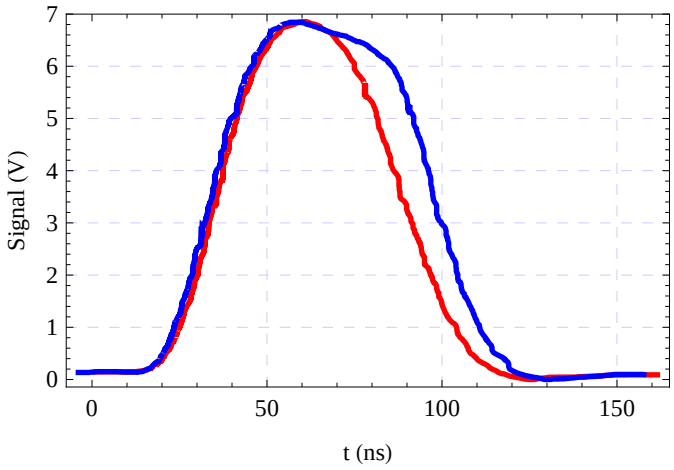

Figure 4.13: Signal at 12% transmission (red line) and 50% transmission (blue line). The pulse height saturates, however a short time after the pulse maxima first cell in the SiPM are recovered and can contribute again to the signal.

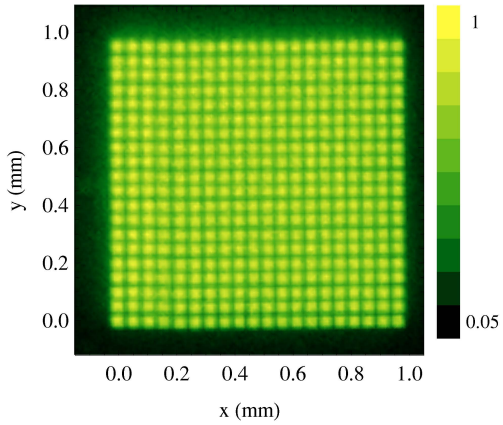

Figure 4.14: Relative sensitivity of channel 2-3 in the SiPM matrix measured at a bias voltage of 70 V, while a laser beam was moved across the SiPM. Laser beam spot size in the SiPM was about 10 μm.

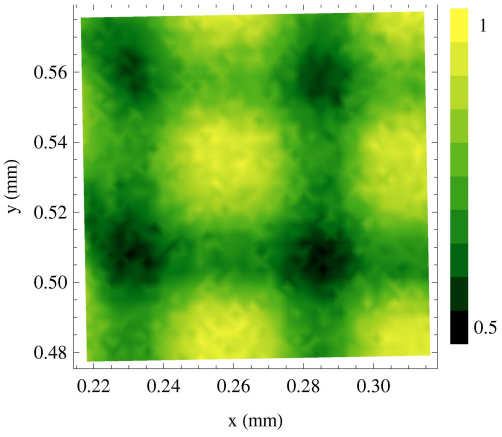

Figure 4.15: Relative sensitivity of small part of the channel 2-3 in the SiPM matrix measured at a bias voltage of 70 V, while a laser beam was moved across the small area of the SiPM. Laser beam spot size in the SiPM was about 10 μm.

the width in the distribution of the collected charge was minimized. Removal of the temperature dependence at the minimum spread was assumed, resulting in a variation of 0.9% in the collected charge. The temperature coefficient which was found to fulfil this minimum is $-1.4\%/K$, which is in good agreement with

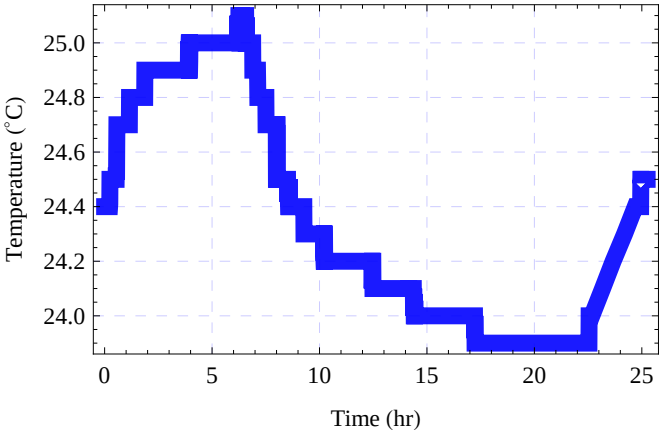

Figure 4.16: The temperature variation measured at the back of the SiPM array during a 25 hour measurement.

measurements from other groups (44). A variation in collected charge of 0.9% is negligible small compared to the statistical fluctuation of triggered cells in PET. This is due to the statistical nature of the light collection and the signal generation process. Only a fraction of the 15000 photons produced by an absorbed 511 keV γ-ray in the LYSO scintillation crystal reaches the SiPM active surface and triggers a Geiger avalanche.

4.5 SiPM Matrix Coupled to a LYSO Crystal Block

The SiPM matrix was coupled via optical grease to a scintillating crystal block of 32 crystals (SinoCeramics, Inc., Shanghai). The crystal block consists of 8×4 of $1 \times 1 \times 20\,\mathrm{mm}^3$ LYSO crystals. There should be no reflector between the crystals in a column, and 250 μm of barium sulfate ($BaSO_4$) powder between adjacent crystal rows (Fig. 4.17). Each crystal in the crystal block can be individually readout in a one-to-one coupling configuration with two SiPM matrices as described on page 27. The crystal block offers superior spatial resolution ($<$ 1 mm) with a high fill factor of 70%.

Barium sulfate is a diffuse reflector with reflectivity of more than 90% which strongly depends on the thickness of the reflector layer. A disadvantage of this type of reflector is the reduction of the total reflectivity. However, the advantage of barium sulfate is its easier handling compared to other reflector materials,

which is handy when building complex crystal blocks. The complete crystal block was wrapped in an aluminium foil which is a specular reflector with reflectivity of about 98%. As can be seen in figure 4.17 there is some misplacement in position of the crystals and there is a thin layer of the $BaSO_4$ between the crystals in the 1×4 columns. This results in a reduction of the total reflectivity and a misplacement between crystals and the SiPM matrix active area.

The crystal block was coupled to only one 16 channel SiPM matrix at one side and readout with a sampling ADC module (SADC, (43)). Radioactive source used for this measurement was ^{18}F, which was placed away from the crystal so that equal illumination of the crystal block can be assumed. SADC trigger levels were set to the SiPM signals of all individual channels slightly above noise and readout by a PC, which recorded the channel number, time and the pulse height for each event.

Although SiPM channels have good uniformity (section 4) we do not get a measurable photopeak when the histogram of pulse heights of all SiPM channels is plotted (Fig. 4.18). However, the sum of the signals which occur in a time window of 5 ns shows a photopeak with 25% energy resolution (Fig. 4.19). This value is not corrected for nonlinearity.

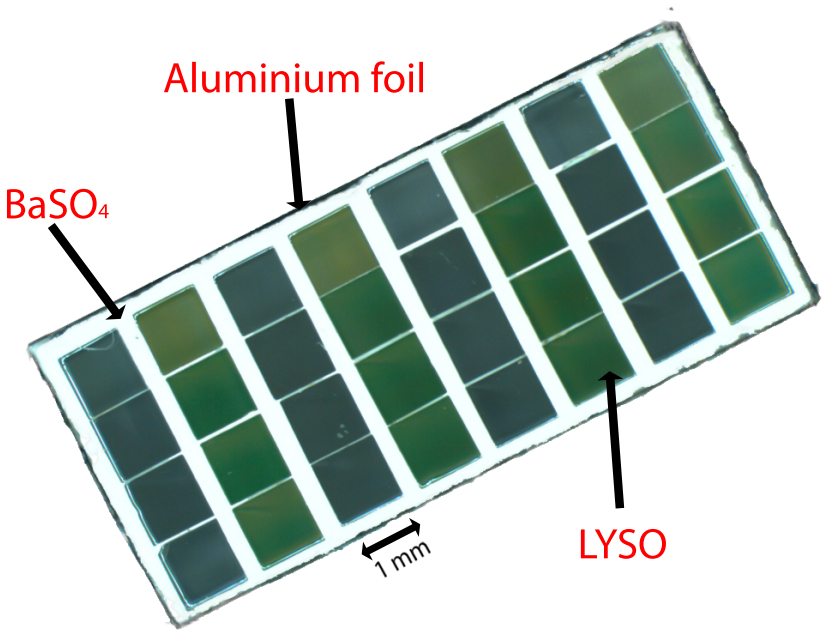

Figure 4.17: 4×8 LYSO crystal block from SinoCeramics inc. with barium sulfate as a reflector. Crystal-block is wrapped into aluminium foil.

The visibility of the photopeak of 511 keV only in the sum of channels can be explained by two facts: first there is a large crosstalk of the scintillating photons in the detector module and second by Compton scattering.

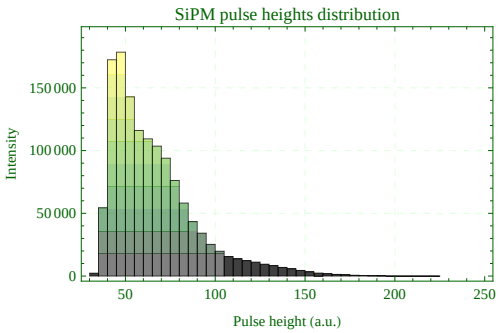

Figure 4.18: Pulse height distribution of single channel in SiPM matrix with 400 cells/mm^2 coupled with the LYSO crystal block.

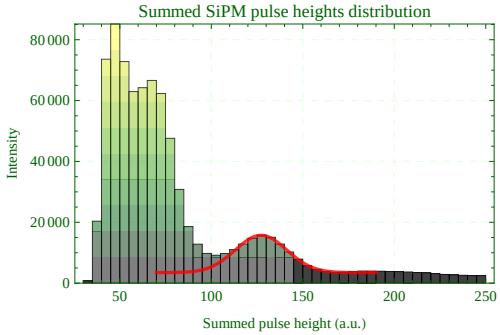

Figure 4.19: Summed pulse height distribution of SiPM matrix with 400 cells/mm^2 coupled with the LYSO crystal block.

In only 70% of all triggered events one SiPM-channel was triggered. For the remaining 30% more than one SiPM-channel was triggered in a time window of 5 ns (Tab. 4.1).

Nr. of triggered channels	1	2	3	4	5
Probability (%)	70.0	17.0	6.5	6.6	0.2

Table 4.1: Distribution of the number of triggered channels in the SADC.

Figure 4.20 shows the distribution of two channels trigger in a time window of 5 ns for the SiPM matrix with 400 cells/mm^2. The width of the lines connecting two channels is proportional with the number of times the two channels have triggered together. Connecting lines are normalized to the the total number of triggered channels when two cells trigger. Similar data in case three and four channels triggering simultaneously are presented in figure 4.21 and 4.22. It is observed that the channels in the SiPM column trigger very often together and the upper columns trigger much more often than the lower columns (Fig. 4.23). The reason for this can be found in the displacement of the crystal block. It was seen by the microscope that the crystals are not perfectly aligned in height, therefore one side of the crystal block was closer to the SiPM surface than the other, resulting in a larger spread of the scintillating photons on the detectors surface. Since the cells more often trigger together when they are in the same

column than cells from adjacent columns it can be conclude that the main reason is not Compton scattering but the crosstalk of optical photons, especially in the crystal columns with a very thin layer of barium sulfate in between. The thin layer of barium sulfate which has a thickness of less than 5 μm can not successfully reflect optical photons and only reduces the total reflectivity compared to a design whit a thin layer of air between the crystals.

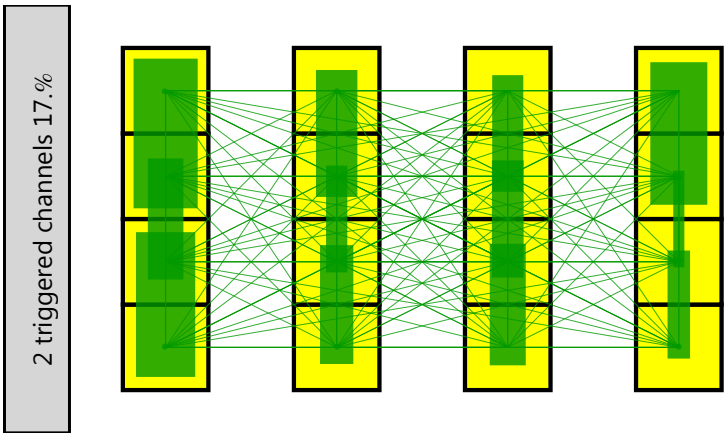

Figure 4.20: Representation of two simultaneously triggered channels. The width of the lines is proportional to the frequency connecting channels triggered together.

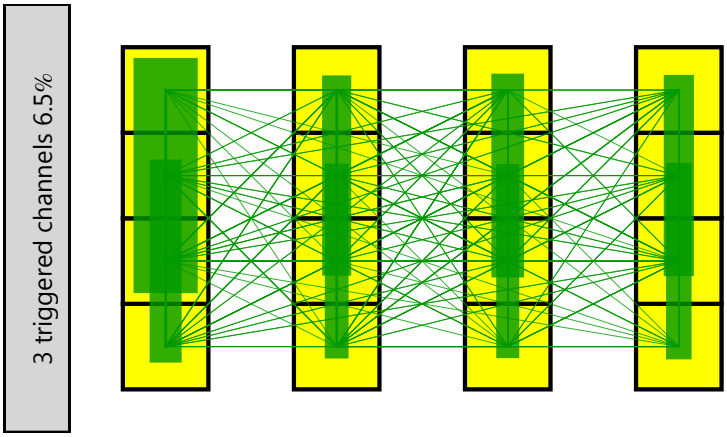

Figure 4.21: Representation of three simultaneously triggered channels. The width of the lines is proportional to the frequency connecting channels triggered together.

The channels in the middle of the 1×4 rows trigger the most times since they collect light from all of their neighboring channels. Channels on the edges have

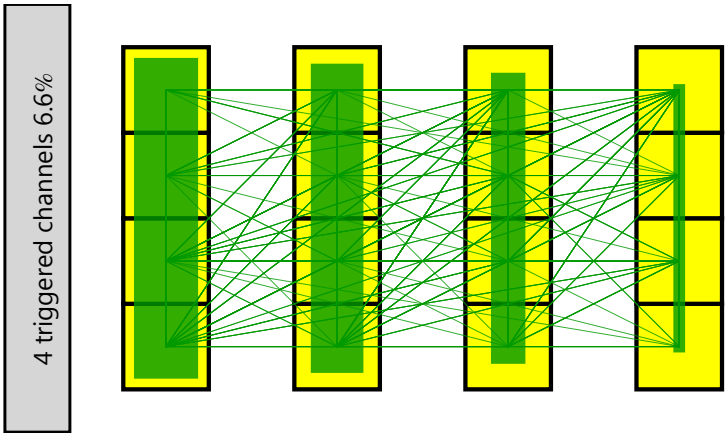

Figure 4.22: Representation of four simultaneously triggered channels. The width of the lines is proportional to the frequency connecting channels triggered together.

only one nearest neighbour and therefore do not fire so often (Fig. 4.23). This dependency is lost if only the channel with the highest amplitude is taken into account in case when multiple channels trigger simultaneously in a time window of 5 ns (Fig. 4.24).

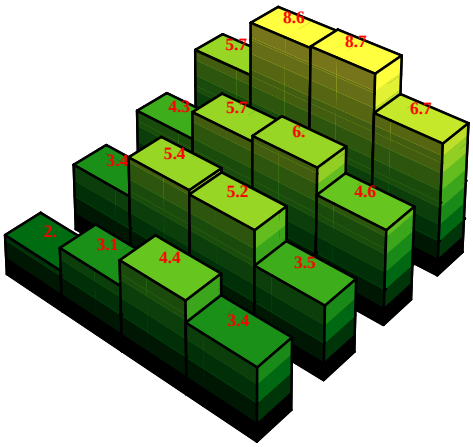

Figure 4.23: Trigger probability for certain channel in SiPM matrix with 400 cells/mm^2.

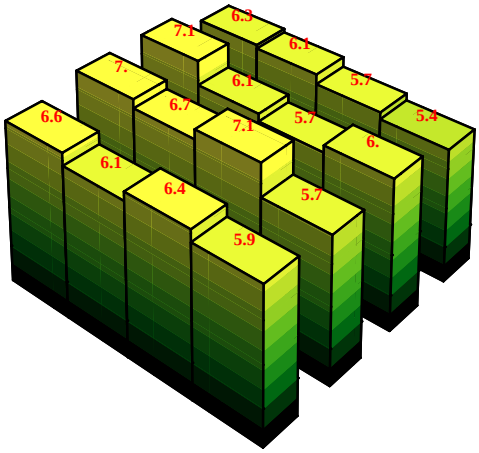

Figure 4.24: Trigger probability for certain channel in SiPM matrix with 400 cells/mm^2. For events where multiple channels triggered in the time window of 5 ns only the channel with the highest amplitude has been taken into account.

4.6 Conclusion

The SiPM matrix shows a good spatial uniformity of the sensitivity and gain between individual channels and is therefore appropriate for the PET/MR. Additionally the individual cells have a small variation in gain and therefore offer a single photon resolution.

The linear dependency of the gain with the bias voltage was observed. The measured gain variation of -1.4% with the temperature is low, however some temperature stability of SiPMs in the PET/MR system will be necessary. An alternative approach maintaining gain stability is by compensating the temperature effects by the adjustment of the bias voltage of the SiPM (45).

The tested LYSO crystal-block of 32 crystals does not fulfil the desirable accuracy which leads to a misplacement of the block with respect to the SiPM array. Another problem of the scintillating crystal block is the barium sulfate reflector which fills the space in between the channels in columns and degenerates the total reflection. A third problem of the crystal is the horizontal misplacement which adds an extra gap between the crystals and the detector, resulting in a spread of optical photons to the neighbouring SiPM channels. Despite the large optical crosstalk in the crystal block and the spread of light due to the epoxy layer and horizontal misplacement of the crystal block, the identification of the γ-interactions in the crystal is still possible, and 25% energy resolution by summing up the signals of the neighboring crystal can be achieved.

To optimally use the one-to-one coupling configuration it will be necessary to reduce the thickness of the epoxy layer covering the surface of the SiPM, to prevent light shearing at the output of the crystal. The use of reflective foils as a reflector would complicate the construction of the crystal block but would result in a better light collection efficiency and a reduction of the optical crosstalk.

5

Monte-Carlo SiPM Model

The measurements described in the previous chapters demonstrate the complex signal generation in SiPM-crystal combinations. In this chapter a realistic model describing the signal of a SiPM which includes characteristics specific to the SiPM is presented. The model is based on a statistical analysis and includes all important parameters of a SiPM: crosstalk, afterpulses, dark counts, quantum efficiency, Geiger discharge probability, geometrical fill factor, gain variation between cells and SiPM cell recovery. The goal was to establish a model that includes simulations of all SiPM parameters without strong simplifications. In this study, MPPCs (Hamamatsu Photonics, Japan) were used as a starting point.

Figure 5.1 depicts a schematic overview of the SiPM response simulation. The crystal properties and the photon tracking have been simulated using GEANT4 simulation software (46, 47). As its output, GEANT4 generates a list of arrival times and coordinates of the photons striking the surface of the SiPM. A custom written code was used for the SiPM response simulation. A photon which reaches the active surface of the SiPM at a certain time (t_i) triggers an avalanche breakdown of the hit cell with a certain probability. This includes two terms: quantum efficiency and probability for Geiger discharge. In case of an avalanche, a mathematical signal is modelled (S_i), considering a fast linear increase of the signal (δ) and an exponential decay versus time (τ_{CDec}), with a gain (G_i) depending on the recovery state of the cell (Fig. 5.2):

$$S_i(t) = \begin{cases} 0, & t < t_i \\ G_i(t_i)\left(\frac{t}{\delta} - \frac{t_i}{\delta}\right), & t_i \leq t \leq t_i + \delta \\ G_i(t_i)\exp\left(-\frac{t-t_i-\delta}{\tau_{CDec}}\right), & t \geq t_i + \delta \end{cases} \tag{5.1}$$

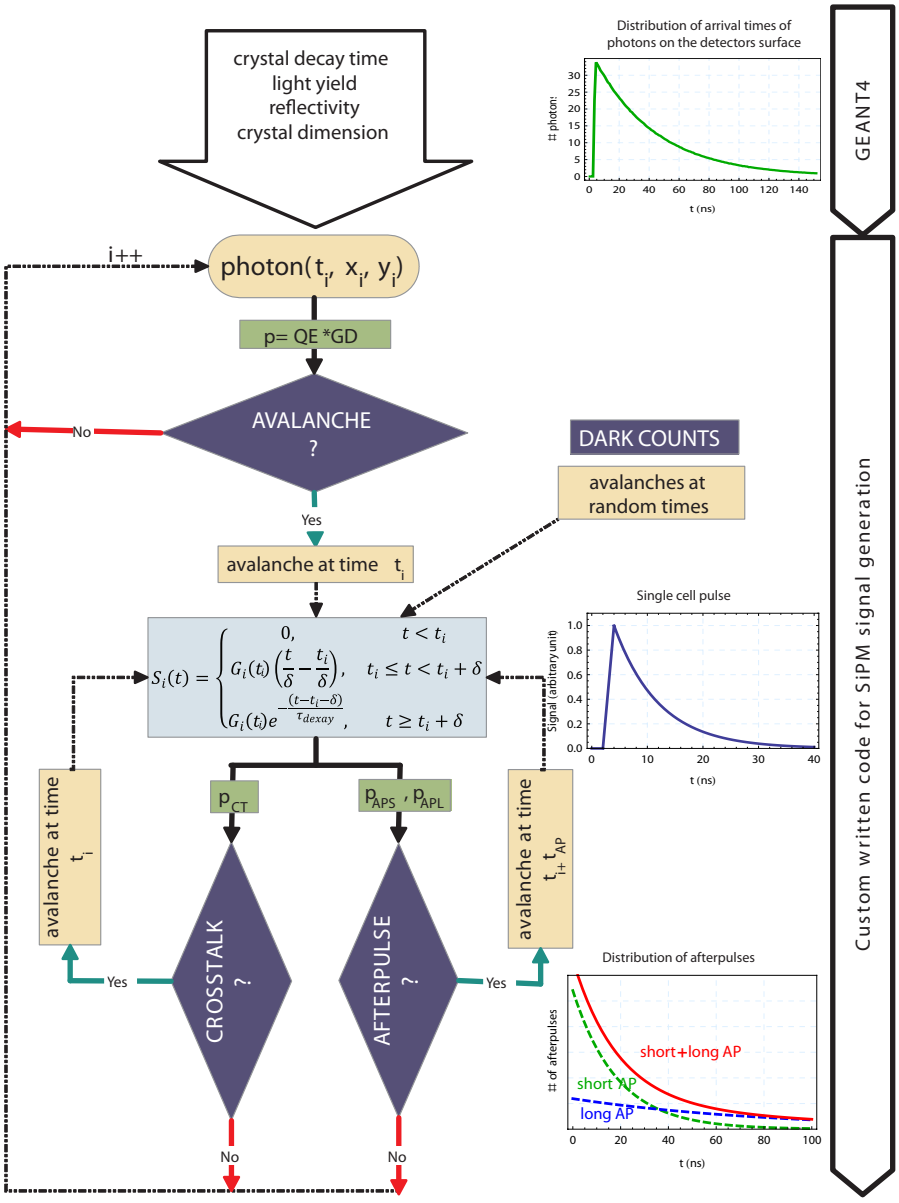

Figure 5.1: Schematic overview of the SiPM response. The crystal properties and the photon tracking have been simulated using the GEANT4 simulation software while a custom written code was used for the SiPM response simulation using Wolfram Mathematica. The avalanche probability includes the quantum efficiency and the Geiger discharge probability. Afterpulses with short and long time constants are included in the model. The crosstalk probability depends on the number of the nearest neighbours. The gain (G_i) depends on the recovery state of a single cell in the SiPM.

Due to differences in the thickness of the SiPM as well as the edge effects, the gain of individual cells may vary depending on the geometrical position of the cell in the SiPM (29). The gain variation between the cells is small (Fig. 5.3). However, the position dependent gain causes the primary and the crosstalk avalanches to be correlated, leading to additional spread in the distribution of the total charge. This effect can be observed by the pulse height distribution of the dark counts. The widths of the peaks corresponding to different numbers of triggered cells does not follow the expected square root dependency due to the correlation in gain between adjacent cells. A Gaussian profile of gain over the SiPM surface producing a single cell gain variation of 5% RMS was assumed for the simulation (Fig. 5.3).

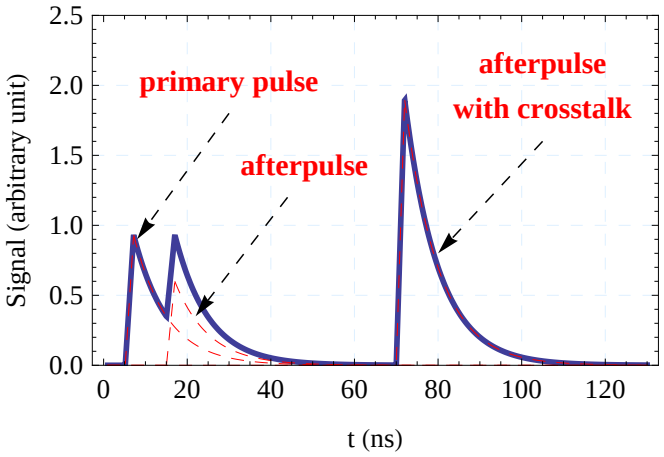

Figure 5.2: Output signal of the SiPM versus time plotted by a blue line representing the sum of single cell pulses (dashed line). The primary pulse had an afterpulse after a short time, which therefore triggered with reduced gain. The SiPM cell was triggered again at 70 ns with a full pulse (dark count or afterpulse). Since this event also produced a crosstalk event, the amplitude is twice as high.

During recovery, the cell can be triggered by impinging photons, crosstalk, afterpulses or dark counts but with a reduced gain and reduced probability (Fig. 5.2) (35, 36). This phenomenon is important for the light detection when the expected number of fired cells is not small compared to the number of cells in the SiPM and if the scintillation light emission decay time is comparable to the SiPM recovery time.

Once the cell has fired, there is a certain probability (p_{CT}) that one of the photons that was emitted during the avalanche triggers one of the adjacent cells (crosstalk). A crosstalk pulse has the same amplitude as a normal avalanche

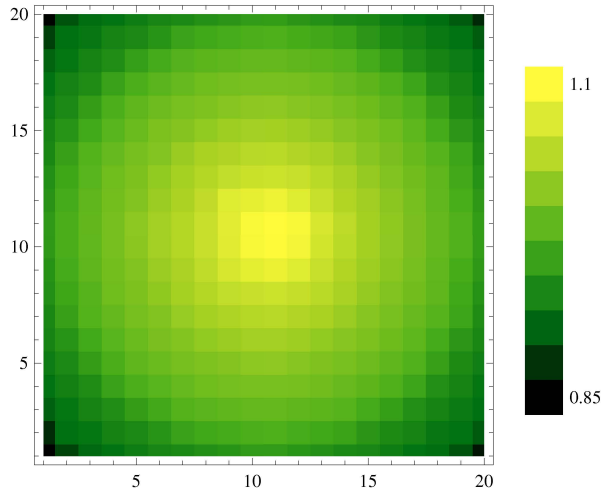

Figure 5.3: Gain map model of a SiPM with 5% gain variation.

and happens almost simultaneously with the original pulse. Higher values were reported for the crosstalk probability in the centre of the SiPM where cells have a higher number of neighbours (29). In the simulation it was assumed that crosstalk increases proportionally to the number of nearest neighbours.

The third process included in the simulations is afterpulsing (Fig. 5.2). The mechanism responsible for this phenomenon is not yet completely clear. However, it seems that afterpulses are primarily caused by charge carriers which are trapped at lattice defects in the semiconductor (48, 49). Once the trapped charge carrier is released it can cause another avalanche and is recognized as an afterpulse. As reported in (35), the afterpulse timing distribution is best described with two exponential functions, one short (p_{SAP}) with about a $\tau_{SAP} = 15\,\text{ns}$ and one long (p_{LAP}) with a $\tau_{LAP} = 80\,\text{ns}$ time constant. Both components were included in the simulation.

The simulated SiPM signal is the sum of all single-cell pulses. Two different aspects of signal analysis were compared: signal integration and pulse height detection. The pulse height detection method needs a lot of computer power since the sum of many functions as described in equation 5.1 needs to be calculated. On the other hand the pulse integration

$$
\begin{aligned}
I_{total} &= \int_0^\infty \sum S_i(t)dt \\
&= \int_0^\infty \left(\sum_{i=1}^{n} G_i(t_i)(\frac{t}{\delta} - \frac{t_i}{\delta})(H(t-t_i) - H(t-t_i-\delta) \right. \\
&+ \left. G_i\left(t_i\right) \exp\left(-\frac{t-t_i-\delta}{\tau_{CDec}} \right) H(t-t_i-\delta) \right) dt
\end{aligned}
$$

can be simplified into

$$
I_{total} = (\tau_{CDec} + \delta) \sum_{i=1}^{n} G_i(t_i), \tag{5.2}
$$

which is a simply sum over all triggered cells with weighted gain multiplied by the sum of cell decay time and signal rise time.

6

Experimental SiPM Model Validation

The developed SiPM model has been evaluated with two types of experiments with well-known experimental conditions. First the response of the SiPM illuminated with a blue LED of low intensity was measured. The SiPM response was simulated under similar conditions. In the second experiment, the SiPM dark count spectrum was measured and also compared to the corresponding simulation.

6.1 Experimental Setup

The setup was housed in a light-tight box at room temperature. A blue LED (wavelength 400 nm) evenly illuminated the SiPM surface through an optical fibre with a trigger frequency of 1 kHz. The LED pulse duration defined the number of photons hitting the SiPM. With short pulses ($\tau \approx 5\,\mathrm{ns}$) a small number of fired cells in the SiPM could be reached (< 10). Measurements were performed with a Hamamatsu S10362-11-050C MPPC ($400\,\mathrm{cells/mm^2}$) (24). Photodetector signals were amplified with the AMP-0611 (Photonique, Woodford Green, United Kingdom) and integrated with the timing filter amplifier Ortec 454 (ORTEC, Oak Ridge, Tennessee, U.S.A.).

6.2 Model Validation

A small number of simultaneous photons (< 10) randomly hitting the surface of the SiPM was simulated and from this hit-distribution the SiPM model was calculated and compared with the measurements. The SiPM parameters used for the simulation are shown in table 6.1. Figure 6.1 shows the measured spectrum of the SiPM with 400 cells/mm^2 illuminated with a LED emitting about 8 photons toward the SiPM surface per event. The signal integration window was set to 20 ns. Therefore, a large number of afterpulses were neglected in the measurements and the long afterpulse component was excluded in the simulations (p_{LAP}= 0). Figure 6.2 shows a good agreement between the measured and the simulated probability distribution of the number of triggered cells.

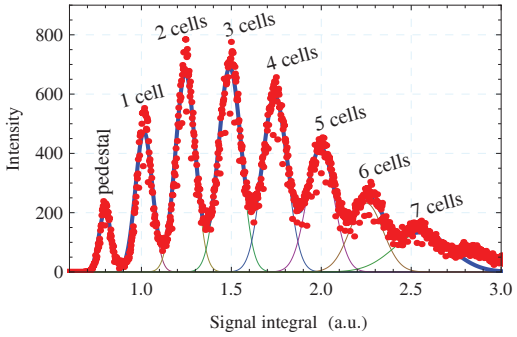

Figure 6.1: Measured spectrum of the S10362-11-050C at 70.3 V illuminated with a blue LED. The signal was integrated with a time window of 20 *ns*. Red dots represent the experimental data, and the blue line represents the sum of eight Gaussian fits.

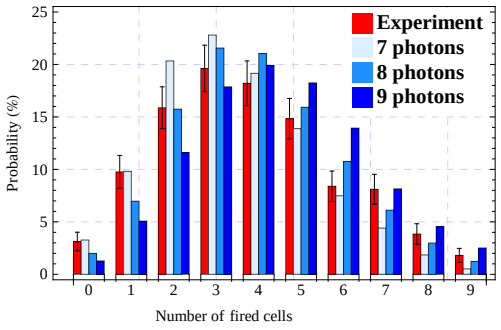

Figure 6.2: Experimental distribution of the number of fired cells (Fig. 6.1) compared to the simulation. For the simulation 7, 8 or 9 photons were randomly propagated to the SiPM surface. SiPM parameters used for the simulation were: p_{CT} = 15%, p_{SAP}= 8%, p_{LAP}= 0% and PDE= 30%.

N_C	PDE	p_{SAP}	τ_{SAP}	p_{LAP}	τ_{LAP}	p_{CT}	δ	τ_{CDec}	τ_{CRec}	DCR
400	30%	8%	15 ns	8%	80 ns	15%	2 ns	11 ns	9 ns	500 kHz
1600	20%	8%	15 ns	7%	80 ns	10%	1 ns	5 ns	4 ns	700 kHz

Table 6.1: Parameters of SiPMs with 400 and 1600 cells/mm^2 measured at 2.7 V and 3.3 V overvoltage respectively at room temperature (24, 29, 35, 36, 40).

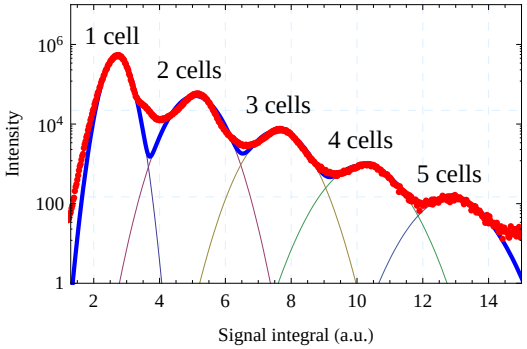

Figure 6.3: A histogram of the measured distribution of fired cells without a light source (dark counts) for S10362-11-050C at 70.3 V. Red dots represent the experimental data, and the blue line represents the sum of five Gaussian fits.

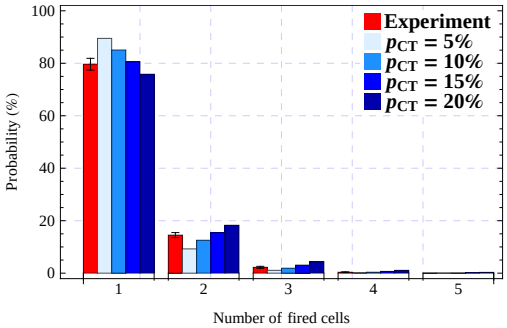

Figure 6.4: The experimental distribution of fired cells (Fig. 6.3) compared to the simulations with different crosstalk probabilities. SiPM parameters used for the simulation were: p_{SAP} = 8%, p_{LAP}= 0% and PDE = 30%.

The second set of measurements was performed without any light source. The detector was at room temperature and the spectrum of dark counts, afterpulses and crosstalk has been measured (Fig. 6.3). The integration method with an integration time of 20 ns was used for the signal analysis. Simulations under similar conditions have been performed but the signal integration method over the complete signal was used for the analysis. The afterpulse amplitude distribution depends on the afterpulse time constants (τ_{SAP}, τ_{LAP}) and the recovery time constant of the cells (τ_{CRec}). An afterpulse can have an amplitude of up to a fully recovered cell discharge. Therefore, the afterpulses cause a signal with an amplitude in between the amplitudes of completely recovered cell pulses, while crosstalk results in a pulse with a higher number of triggered cells. A 9 ns recovery time has been used for Hamamatsu S10362-11-050C devices (Tab. 6.1). Because of the very short recovery time we would expect to have more pulses with a high amplitude similar to the amplitude of two triggered cells. This can be seen in the simulation but not in the experiment, due to the integration time of 20 ns in the experiment. Therefore in the experiment, only afterpulses which occur shortly after the primary avalanche are included. The histogram of the distribution of fired cells without light source was fitted with five Gaussian functions, from which the probability of a certain number of cells was calculated. Figure 6.4 shows the measured probability of fired cells compared with the simulation, where the crosstalk probability has been varied between 5% and 20%. Figure 6.5 shows a

more quantitative study of the deviation of the probability for a certain number of fired cells. The sum of squares of the deviation of the probability predicted by the simulation to the measured probability, is plotted as a function of the crosstalk. The deviation reaches a minimum at 15% crosstalk probability, which is in accordance with the reported crosstalk probability for this device (Tab.3.1). From these studies, we conclude the validity of the model describing the SiPM signal generation.

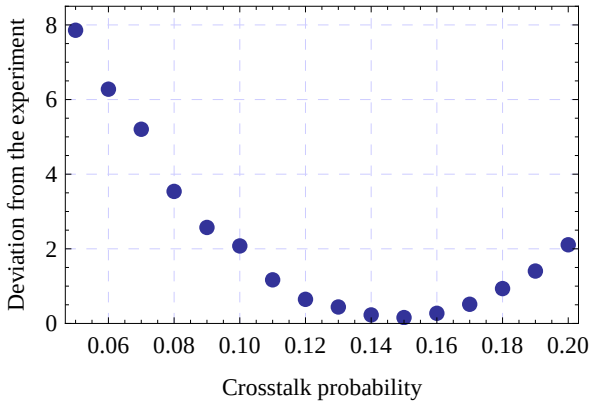

Figure 6.5: Sum of squares for the deviations of the predicted probability (simulation of the SiPM response) from the measured probability (S10362-11-050C), as a function of crosstalk probability. Simulated data with 15% crosstalk probability shows the best agreement with the experiment.

7

Simulation of a SiPM Coupled to Scintillating Crystal

For the following studies scintillators emitting light in the visible region were considered. The amount of light emitted is ideally proportional to the amount of energy that is deposited in the scintillator. With this concept, a high efficiency for the detection of γ-rays and, at the same time, good energy resolution can be achieved. For PET imaging, a high-Z (high interaction probability of 511 keV γ-rays and low Compton scattering), dense scintillation material with fast emission of a large number of light photons is advantageous. When using SiPMs for detecting the scintillation light, the brightness of the scintillating material and its decay time in combination with the photon detection efficiency (PDE) of the SiPM are expected to determine the energy and time resolution of the detector. For an optimal energy and time resolution, further demands on the SiPM performance arise considering the cell size of SiPMs, which affects the linearity and dynamic range. A scintillating material with high light output needs a SiPM with high number of cells to avoid saturation and non-linear behaviour. However high cell density has the disadvantage of a smaller PDE since the geometrical fill factor decreases for currently available standard SiPMs. On the other hand, smaller cells have a smaller capacitance, and therefore a smaller gain, resulting in less crosstalk and afterpulses. In addition, the relation of the number of scintillation photons and number of cells influences the SiPM signal. Further optimizations involve the influence of overvoltage, fill factor, crosstalk, afterpulses, etc. Higher overvoltage results in better Geiger discharge probability and the PDE increases, however the crosstalk and dark count rate increase as well. The gain also increases with overvoltage. Crosstalk can be reduced with optical trenches in between the

cells (50). However, the PDE is reduced as well, since the fill factor decreases. There are cross correlations, for example: optical trenches reduce crosstalk, which allows the increase of the overvoltage improving the PDE and the gain. Thus, when optimizing SiPM performance, the best parameter combination will depend on the specific application.

	Larger cell size		Higher overvoltage		Trenches	
PDE	$\oplus$	Better fill factor	$\oplus$	Geiger efficiency	$\ominus$	Reduced fill factor
Crosstalk			$\ominus$	Increased	$\oplus$	Reduced
Dynamic range	$\ominus$	Less cells				
Linearity	$\ominus$	Less cells	$\ominus$	Increased PDE	$\oplus$	Reduced PDE
Dark counts			$\ominus$	Increased		
Gain	$\oplus$	Larger capacitance	$\oplus$	$Q = C \cdot \Delta U$		

Table 7.1: Optimization matrix of SiPM parameters.

SiPMs are very compact detectors and hence offer the opportunity of a one-to-one coupling configuration, in which a small scintillating crystal is optically coupled to one SiPM. This configuration offers the best possible spatial resolution and was the focus of this study. Optical photons generated by interaction of γ-rays inside the scintillating crystal do not always reach the active surface of the detector due to the light absorption within the scintillator and losses on the surface of the scintillator. Which strongly depend on the wrapping and the geometry of the crystal. Thus, only a fraction of the generated light reaches the SiPM active surface. Transport of optical photons was simulated with the ray-tracing software GEANT4 (46, 47). The simulated crystal had a size of $1 \times 1 \times 20\ mm^3$ and was wrapped in reflective foil with a wavelength-dependent reflectivity spectrum (based on the spectrum in the data sheet (38)). The crystal material simulated was LYSO, with 43 ns decay time and a light yield of 28000 $photons/MeV$. There was a layer of 300 μm epoxy between the crystal and the SiPM. The interaction points of the γ-rays in the crystal were simulated with an exponentially decreasing probability. The GEANT4 simulation calculated a collection efficiency of 18% for the described crystal (41). The non-proportionality of the light yield in the scintillating crystal was not included in the simulation.

SiPM Monte-Carlo simulations were performed to predict the influence of various parameters on the energy resolution of this LYSO-SiPM detector module. A predefined number of photons with exponential distribution of arrival times and a time constant of 43 ns were assumed to hit the SiPM surface from which the SiPM signal was modelled. 5000 events were simulated for each parameter set to

obtain sufficient statistical accuracy for the simulated data. The time required on a Quad-Core PC to simulate a single parameter set is about 5 minutes. The SiPM parameters used for the simulations are collected in table 3.1. Each parameter has been varied in a certain range while others were fixed at the reported values for Hamamatsu MPPCs. The variation of the SiPM response is due to the statistics of the number of initially triggered cells, crosstalk, afterpulses and dark counts, which are influenced by the cell recovery time. The SiPM response was corrected at the end for non-linear effects as described on page 13. The parameters A and B (equation 2.9) were calculated from the best fit to the simulated data of the SiPM response for different energy depositions.

The energy resolution studies of a LYSO-SiPM module with a crystal of the same dimensions as mentioned, wrapped into a 3M reflector foil, was experimentally investigated with the pulse height detection method and are presented in chapter 3. This data can be compared with the SiPM-LYSO model predictions where the crosstalk probability was varied from 0 to 27% (Fig. 7.1 and 7.2). The parameter B for the SiPM with 400 cells/mm^2 has a value of 1.84 in the simulation for 15% crosstalk probability (Fig. 7.1). About the same value for parameter B was obtained from the experiment at 70.3 V (Fig. 3.8). Good agreement between simulation and experiment is also observed for the configuration with 1600 cells/mm^2 (Fig. 3.9 and 7.2).

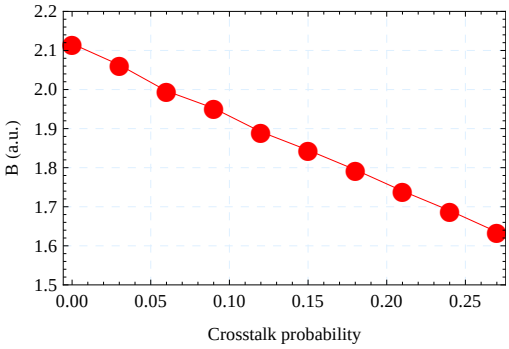

Figure 7.1: Simulated dependency of the parameter B on the crosstalk probability for the pulse height method for SiPM with 400 cells/mm^2.

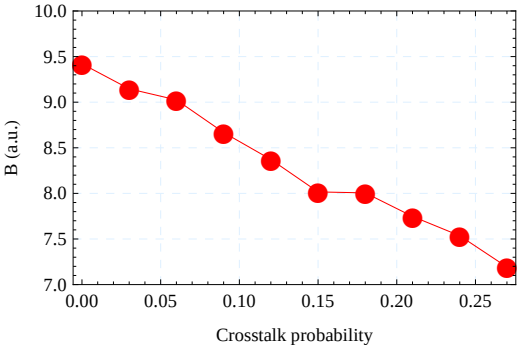

Figure 7.2: Simulated dependency of the parameter B on the crosstalk probability for the pulse height method for SiPM with 1600 cells/mm^2.

Figure 7.3 shows the results of the simulated energy resolution as a function of generated scintillation photons. With an increased number of photons, the energy resolution improves for both cell densities. However, the superior energy

resolution at high energies is misleading due to the saturation of the SiPM. After the correction of non-linear effects, the simulated energy resolution for SiPM with 400 cells/mm^2 becomes minimal between 15000 and 25000 photons. In this area, the improvement of the statistical error compensates the degradation of the SiPM response due to the non-linearity and the energy resolution stays at a value of about 15% for SiPM with 400 cells/mm^2. Saturation of the SiPM with 1600 cells/mm^2 occurs only with a higher number of photons, which were not simulated. From this study we conclude that SiPMs with 400 cell/mm^2 are a better choice for the readout of $1 \times 1 \times 20$ mm^3 LYSO crystals in terms of energy resolution, despite the four times smaller number of cells and thus nonlinear behaviour. A higher PDE of the SiPM with 400 cells/mm^2 results in better energy resolution for up to 28000 optical photons generated in the scintillating crystal. At higher numbers of photons the SiPM with 1600 cells/mm^2 would be superior.

The simulated energy resolution of 15% for a SiPM with 400 cells/mm^2 and 18% for a SiPM with 1600 cells/mm^2 for 15000 photons generated in the crystal are slightly, but systematically below the experimental values of 18% and 22% for 511 keV photons undergoing photoelectric effect in LYSO (Tab. 7.2). This can be explained by the fact of using a linear dependency for the number of scintillation photons on the deposited energy in the model, while the number of generated photons is varying in the experiment due to the nonlinearity and non-homogeneity of the crystal. This non-proportionality of the light yield is a fundamental limitation to the intrinsic energy resolution. LYSO has an intrinsic energy resolution of about 8.3% for 511 keV photons (51). However, the model shows the trends and influences of different parameters on the performance of LYSO-SiPM modules, which is of main interest for their optimization.

A rough estimate of the SiPM response to different crystals can be made from figure 7.3. A BGO crystal (52) with about 8000 photons/MeV and a decay time of 300 ns would result in rather poor energy resolution due to the low light yield. Lately discovered LaBr (53) offers new perspectives in PET due to its high light yield of about 60000 photons/MeV and a short decay time of 35 ns. In this case SiPM with 400 cells/mm^2 would limit the performance due to the non-linearity, a configuration with 1600 cells/mm^2 would be advantageous.

Monte-Carlo simulations were performed to predict the influence of different parameters on the energy resolution of the crystal-SiPM combination. In total 500 parameter sets were investigated in this study. For each parameter set 5000 photoelectric interactions of γ-rays were simulated. Simulations were performed for different energies of γ-rays which generated from 3000 to 27000 photons in

SiPM Type	N_C	Simulation		Experiment	
S10362-11-050C	400	10	15*	12	18*
S10362-11-025C	1600	17	18*	20	22*

Table 7.2: Comparison of measured and simulated energy resolution (FWHM (%)) for SiPM with 400 and 1600 cells/mm^2. * Data corrected for the nonlinear effects.

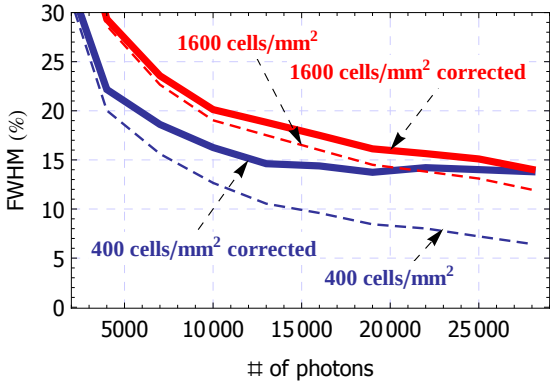

Figure 7.3: Simulated energy resolution versus the number of generated optical photons in the scintillating crystal for a SiPM with 400 (blue) and 1600 cells/mm^2 (red). Simulated energy resolution was corrected for nonlinear effects. The following parameters were assumed: decay constant of crystal 43 ns, short afterpulse probability 8%, long afterpulse probability 8%, crosstalk probability 15%, recovery time constant of cell 9 ns and 4 ns for SiPM with 400 and 1600 cells/mm^2, respectively.

the crystal.

The afterpulse probability was varied in a range from 0 to 20%, while other SiPM parameters were fixed at the reported values for Hamamatsu MPPCs. Figures 7.4-7.7 show the contour plots of the corresponding energy resolution for SiPMs with 400 and 1600 cells/mm^2 for the pulse height detection and integration method. The energy resolution is corrected for nonlinear effects. Contour lines as a function of afterpulse probability and the number of the photons generated in the crystal represent regions with constant energy resolution. When the lines are close together it implies a steep gradient. For contour lines which are parallel to the x-axis no dependency on the parameter plotted on that axis is evident. With an increased number of generated photons in the crystal the influence of the afterpulses on the energy resolution for the integration method increases, and the energy resolution degrades by about 0.5% at 8% afterpulse probability

for both cell densities at 15000 photons (Fig. 7.4, Fig. 7.6). However, there is no influence of the afterpulses on the pulse height detection method, even at high photon fluxes (Fig. 7.5, Fig. 7.7). This is because the afterpulses significantly affect the signal of the SiPM only after the pulse maximum.

Afterpulses prolong the recovery time of the detector, which may be an issue when the time between events would be comparable to the crystal decay time. This was not the case in the simulation and is also not expected to happen in PET.

The simulations show that crosstalk does not play an important role for the energy resolution of the LYSO-SiPM module (effects below 2%, Fig. 7.8-7.11). Although the crosstalk should preferably be small, devices with a crosstalk of up to 27% should still be suitable for PET.

The cell recovery time was varied from 3 to 100 ns. For small light intensities only a slight decrease in signals with both analysis methods when increasing the recovery time was observed. With an increased number of photons in the crystal, the influence of the recovery time becomes more important and governs the performance of the detector. In Fig. 7.12 and Fig. 7.13 a strong dependency of the energy resolution for a SiPM with 400 cells/mm^2 can be seen. Due to the short recovery time, the Hamamatsu MPPCs with only 400 cells/mm^2 perform well at higher photon fluxes. Fig. 7.14 and Fig. 7.15 show the influence of the cell recovery time on the SiPM with 1600 cells/mm^2. There is little influence on the pulse height detection method and no influence on the integration method.

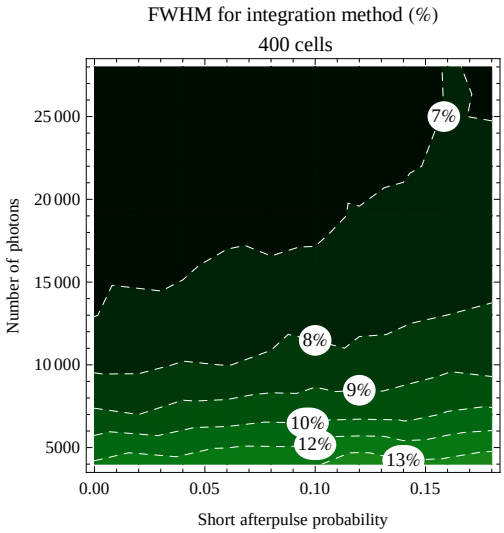

Figure 7.4: Simulated energy resolution as a function of the afterpulse probability and the number of photons generated in the scintillating crystal for a SiPM with 400 cells/mm^2.

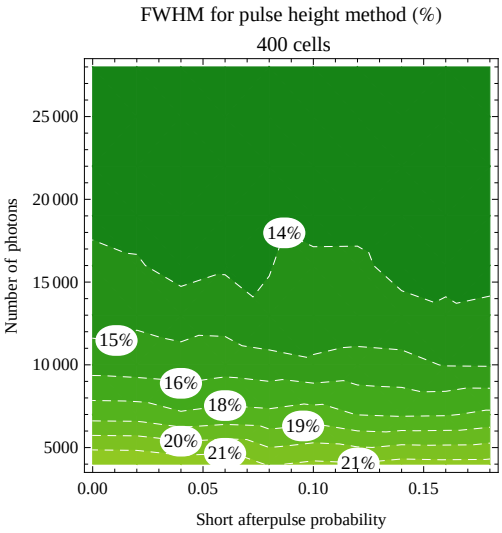

Figure 7.5: Simulated energy resolution as a function of the afterpulse probability and the number of photons generated in the scintillating crystal for a SiPM with 400 cells/mm^2.

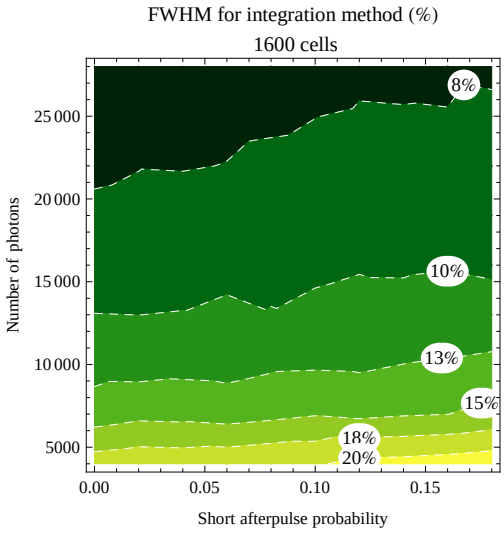

Figure 7.6: Simulated energy resolution as a function of the afterpulse probability and the number of photons generated in the scintillating crystal for a SiPM with 1600 cells/mm^2.

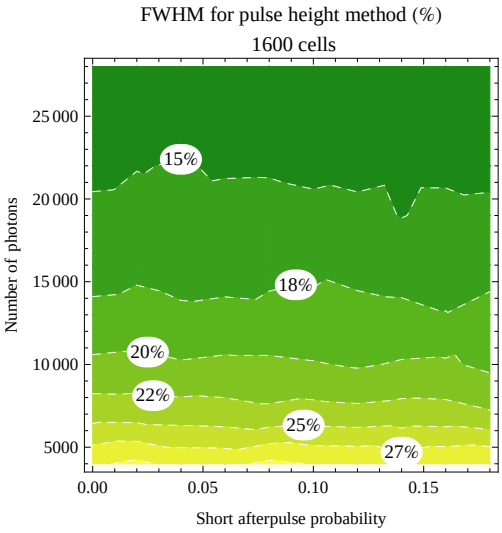

Figure 7.7: Simulated energy resolution as a function of the afterpulse probability and the number of photons generated in the scintillating crystal for a SiPM with 1600 cells/mm^2.

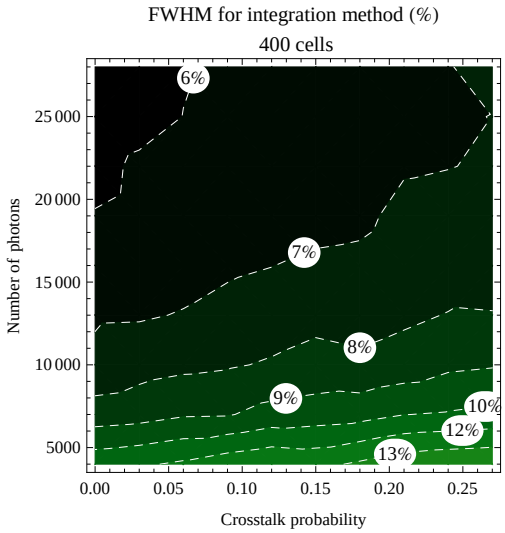

Figure 7.8: Simulated energy resolution as a function of the crosstalk probability and the number of photons generated in the scintillating crystal for a SiPM with 400 cells/mm^2.

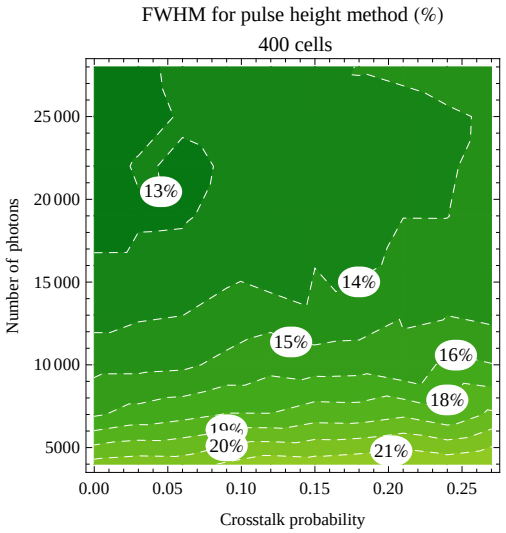

Figure 7.9: Simulated energy resolution as a function of the crosstalk probability and the number of photons generated in the scintillating crystal for a SiPM with 400 cells/mm^2.

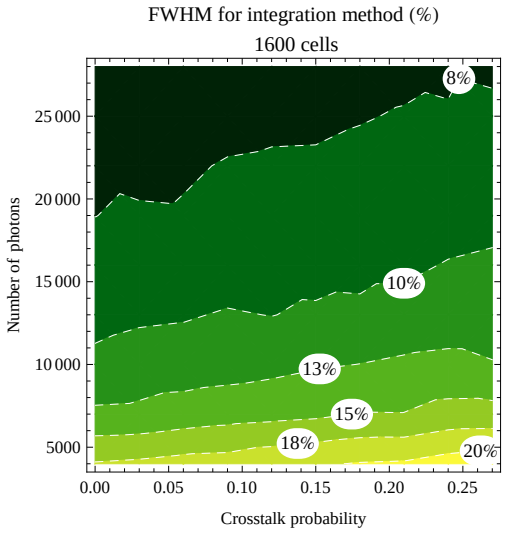

Figure 7.10: Simulated energy resolution as a function of the crosstalk probability and the number of photons generated in the scintillating crystal for a SiPM with 1600 cells/mm^2.

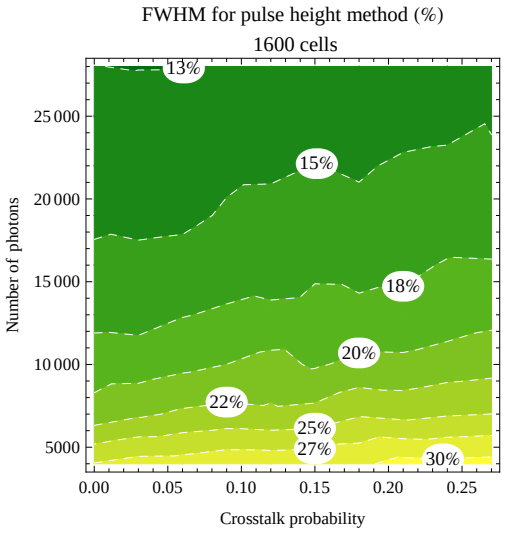

Figure 7.11: Simulated energy resolution as a function of the crosstalk probability and the number of photons generated in the scintillating crystal for a SiPM with 1600 cells/mm^2.

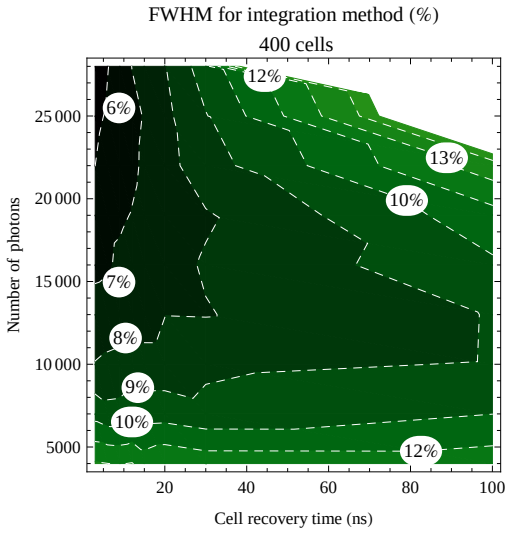

Figure 7.12: Simulated energy resolution as a function of the cell recovery time and the number of photons generated in scintillating crystal for a SiPM with 400 cells/mm^2.

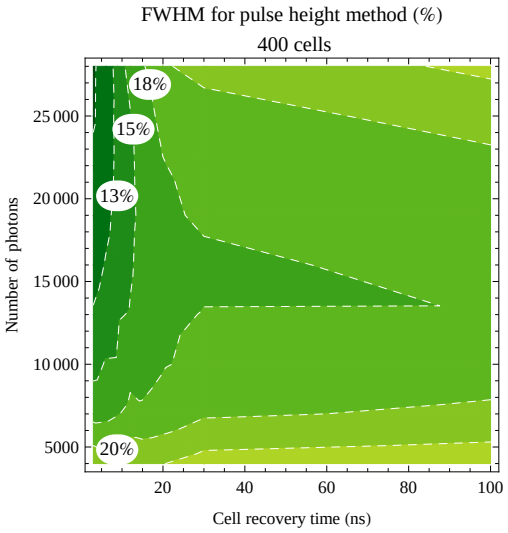

Figure 7.13: Simulated energy resolution as a function of the cell recovery time and the number of photons generated in the scintillating crystal for a SiPM with 400 cells/mm^2.

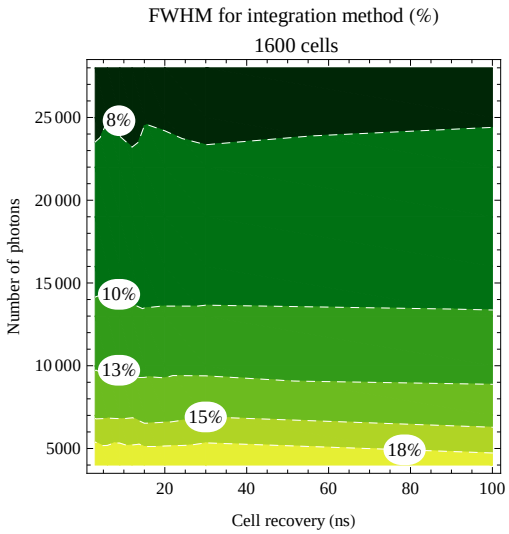

Figure 7.14: Simulated energy resolution as a function of the cell recovery time and the number of photons generated in the scintillating crystal for a SiPM with 1600 cells/mm^2.

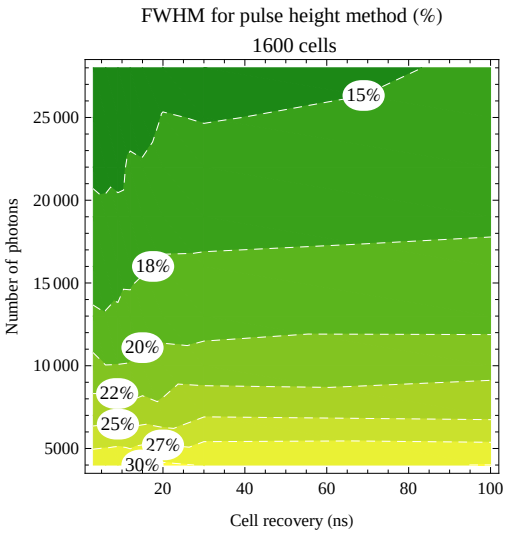

Figure 7.15: Simulated energy resolution as a function of the cell recovery time and the number of photons generated in the scintillating crystal for a SiPM with 1600 cells/mm^2.

7. SIMULATION OF A SIPM COUPLED TO SCINTILLATING CRYSTAL

8

Performance of SiPMs Coupled to Different Scintillation Crystals

A number of silicon photomultipliers (SiPMs) as well as scintillating crystals which are potentially suitable for combined PET/MRI are available. Different combinations of them lead to different performance of detector modules. With the help of the SiPM model described in chapter 5 a series of scintillating crystals coupled to three different Hamamatsu MPPC detectors are discussed in this chapter regarding their energy resolution (Tab. 8.1). The response of SiPMs coupled to four different crystals irradiated by γ-rays was simulated and investigated. The energy of incident γ-rays ranged from 0.1 MeV up to 1 MeV in step of 0.05 MeV.

SiPM / Crystal	S10362-11-025C (1600 cells)	S10362-11-050C (400 cells)	S10362-11-100C (100 cells)
BGO	15.7%	26.2%	29.0%
LaBr	16.6%	28.8%	34.8%
NaI	17.6%	30.6%	35.5%
LYSO	17.9%	30.7%	34.7%

Table 8.1: Effective photon detection efficiency for the investigated SiPMs and different coupled scintillators often used for PET.

The scintillating crystals used in this study show spectral response ranging from 270 to 900 nm. The spectrum of the emitted light from some of the more commonly used crystals for PET is shown in figure 8.1. The peak sensitivity for the investigated SiPMs is at 440 nm (29) which does not correspond with

the emission spectra of some scintillating crystals. From emission spectra of the scintillation crystals and sensitivity of the SiPMs the relative PDE was calculated for each crystal-SiPM combination (Tab. 8.1). Relevant properties of common crystals used for PET are shown in table 8.2.

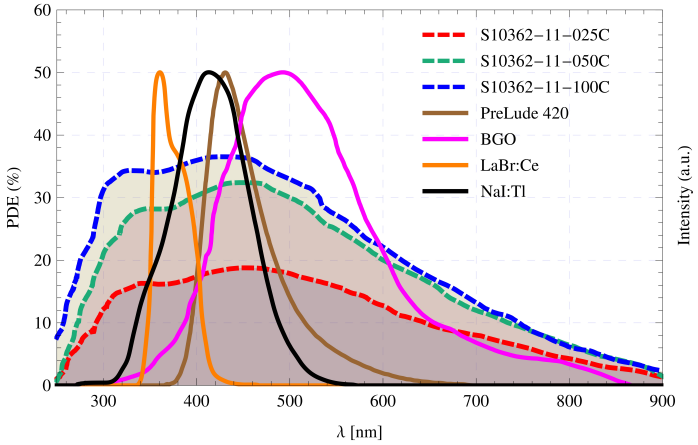

Figure 8.1: Normalized emission spectra of BGO, LaBr, NaI and LYSO together with the wavelength dependent photon detection efficiency for three different SiPMs (24, 29, 37, 54).

The effective photon detection efficiency was calculated as

$$\mathrm{PDE}_{\mathrm{eff}} = \frac{\int \mathrm{PDE}_{\mathrm{SiPM}(\lambda)} \cdot w_{\mathrm{crystal}}(\lambda) d\lambda}{\int w_{\mathrm{crystal}}(\lambda) d\lambda} \tag{8.1}$$

where $w_{crystal}(\lambda)$ stands for the emission spectra of the crystal and $\mathrm{PDE}_{\mathrm{SiPM}}(\lambda)$ photon detection efficiency of the SiPM.

8.1 Scintillation Crystals

The scintillation process is one of the most powerful methods for detection of 511 keV photons. Scintillators are materials which produce flashes of light when they absorb radiation. The light is emitted isotropically and the amount of the light emitted is proportional to the energy deposited in the crystal. Various types of scintillators are discussed in this chapter. In general, a good scintillator should have the following properties:

- The material should have high stopping power for incident photons (sensitivity).
- High conversion efficiency to convert the energy of the incident photons into scintillation photons (energy spectroscopy).
- The crystal should be transparent to its own scintillation light to allow transmission of the light.
- The light yield of the crystal should be linear with the deposited energy (energy spectroscopy).
- The rise and decay time of the induced light emission should be short in order to get good time resolution and to have high count rate capability.
- The material should be resistive to radiation damage.
- The material should be able to be produced in larger sizes and complex geometry.
- The index of refraction of the scintillator should match the photodetector (light collection efficiency).
- The wavelength of emitted optical photons should match the spectral sensitivity of the photodetector (photon detection efficiency).

Property / Crystal	Density (g/cm^3)	Light Yield (Photons/MeV)	Refractive Index	Attenuation Length (mm)	Wavelength of Max. Emission (nm)	Decay Time (ns)	Z_{eff}	FWHM (%) at 662 keV
BGO	7.13	8200	2.15	11	480	300	76	9
LaBr	5.1	60000	1.9	22.3	370	25	47	3
NaI	3.67	37700	1.85	29	415	230	51	6
LYSO	7.1	32000	1.81	12	420	41	65	8

Table 8.2: Properties of common scintillators for PET (37, 52, 53, 55).

There is no optimal crystal which would combine all parameters described above so compromises have to be made. A compromise between the crystal parameters needs to be chosen for each application.

8.1.1 NaI

NaI scintillation properties were discovered in 1948 and despite the decades of research in other scintillation materials, NaI is still a frequently used scintillator. The most notable property of NaI is its excellent light yield and small non-proportionality of its scintillation response with deposited energy. Therefore NaI offers good energy resolution for the scintillation detection principle. NaI is hygroscopic and must in generally be handled with protection, enclosure in a air-tight box assures long time operation performance. The relatively long decay time (230 ns) of NaI is a strong drawback for PET since it affects timing performance and results in dead time. Another drawback is the long scintillation component (0.15 s) which makes NaI unsuitable for applications where single-photon sensitivity is needed. Another drawback of NaI is low density and low effective Z resulting in poor sensitivity for 511 keV γ-rays.

8.1.2 BGO

BGO ($Bi_4Ge_3O_{12}$) used to be the PET scintillator for many years. BGO is a dense material (7.13 g/cm^3) with a high effective atomic number (76) therefore its advantage is a high photoelectric conversion efficiency of γ-rays. However BGO crystals suffer from slow decay time of scintillating light (300 ns) which results in poor timing resolution and consequently leads to a long coincidence time window ($>$ 10 ns) and larger dead time. The peak emission wavelength of BGO crystals (480 nm) does not perfectly match the SiPM peak sensitivity. The light yield of BGO crystals of 8200 photons/MeV is far below the brightest scintillating crystals which limits the timing and energy resolution. However due to BGO's good linearity the energy resolution of BGO can compete with some much brighter crystals (56).

8.1.3 LYSO

A new generation of PET scanners is based on the Cerium-doped Yttrium Orthosilicate (LYSO). LYSO emits optical photons in wavelengths ranging from 370 to 630 nm with a maximum at 425 nm which corresponds with the peak sensitivity of the SiPM. The advantages of the LYSO crystal is its high light yield output of about 32000 photons/MeV, fast decay time (40 ns) and high density (7.3 g/cm^3). However the energy resolution of LYSO is significantly worse than expected by Poisson statistics. This is due to non-proportionality. The number of generated

optical photons per unit energy deposited in the LYSO depends on the energy of the particle that excites it. A 511 keV photon starts the excitation process by either generating an energetic Compton electron or an electron by photoelectric interaction. The generated electron excites the crystal but also produces secondary energetic electrons with lower energy. Due to the random nature of the distribution of secondary electrons the light yield of the crystal varies for the same incident gamma photons which are source of intrinsic energy resolution of the scintillating crystals. The intrinsic energy resolution of LYSO crystals varies strongly between manufactures. The best LYSO crystals are made by Saint-Gobain, their LYSO crystal is known under the name $PreLude^{TM}$ 420 and has intrinsic energy resolution of about 8% for 622 keV γ-rays. Other manufactures are above this value and reach up to 20% in intrinsic energy resolution.

8.1.4 LaBr

LaBr is the brightest crystal presented in this work. With about 60000 photons/MeV emitted and a decay time constant of only 25 ns it offers excellent energy and time resolution. Major disadvantage of LaBr is its high hygroscopy and low density. To protect it from the air humidity, it must be housed in an air tight protective enclosure, which limits the fill factor when arranging the crystals in an array to provide position sensitivity. Another drawback of LaBr is a low probability for photoelectric effect due to the low effective atomic number (47).

8.2 Results of Simulations

In the simulation, a certain energy was deposited in scintillating crystals from which a number of optical photons were simulated with exponential timing distribution. The generation of optical photons in the scintillator does not include the nonlinear behaviour of the deposited energy transfer into optical photons. Optical photons were collected at the SiPM surface with a probability of 20% (light collection efficiency (41)). From photons hitting the sensitive surface the response of the SiPM with 100, 400 and 1600 cells/mm^2 was calculated with the model presented in chapter 5. The typical parameters for SiPMs as presented in table 3.1 were used. For each data point in the simulation 5000 events were simulated. The SiPM response was fitpted with the NonlinearModelFit function implemented in Wolfram Mathematica which minimizes the sum of the squares of the residuals of the fitted data from the theoretical curve. This function returns

best-fitting parameters together with standard errors of the fitted parameters which were used for the error bars. The simulations for all combinations of the scintillating crystals and SiPMs for all energies takes around 3 days on a Quadcore 3GHz PC. The presented results of the simulations are corrected for nonlinear effects of the SiPM.

Figure 8.2 and 8.3 show the averaged waveforms (over 5000 events) of the SiPM pulses, with different SiPMs coupled to different scintillating crystals and 511 keV incident photons. Full energy deposition was assumed (photoelectric effect). In figure 8.2 scintillating crystals with fast decay constants (LaBr and LYSO) are presented whereas figure 8.3 shows waveforms for the slower scintillating crystals BGO and NaI. For fast scintillators a maximum in the signal between 12 an 30 ns is observed. For slow crystals a maximum occurs in a wider interval between 20 and 100 ns.

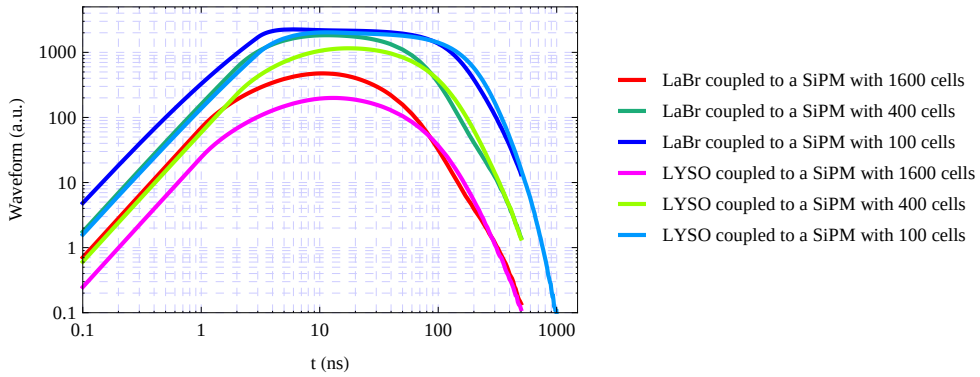

Figure 8.2: Waveforms of fast scintillators coupled with three different SiPMs for 511 keV γ-rays photoefect.

A wide interval implies poor time resolution and problems for the pulse height detection method. When coupling a scintillator with a short decay time and a high light yield, for example LaBr to a SiPM with 100 cells/mm^2, signal saturation is observed (dark blue line in figure 8.2). Here most cells in the SiPM are fired before 3 ns, however as they recover there is still a lot of light which immediately triggers the recovered cells and that results in a broad maximum of the signal. It is clear that in such case the determination of energy deposited in the crystal is very limited and only reasonable with the integration method.

Figures 8.4 to 8.7 show the dependency of the time at witch the SiPM pulse maxima occurs on the deposited energy in different crystals for the pulse height

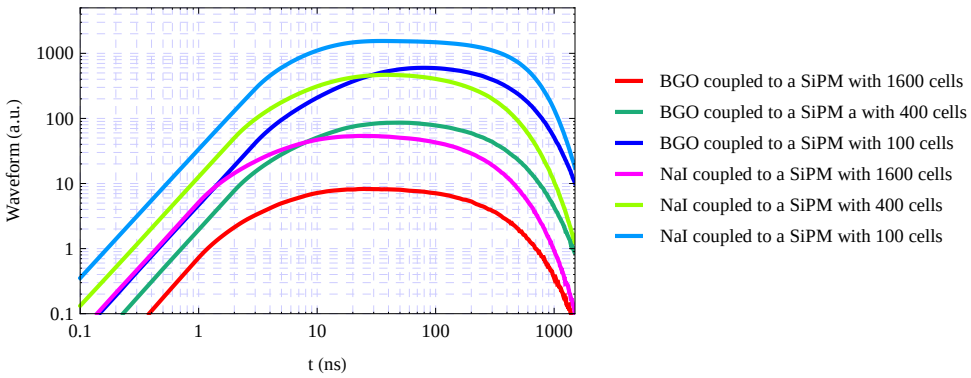

Figure 8.3: Waveforms of slow scintillators coupled with three different SiPMs for 511 keV γ-rays photoefect.

detection method. For SiPMs coupled with BGO crystals a broad distribution of the time of the pulse maxima for both configurations with 400 and 1600 cells can be seen. For 400 cells the pulse maximum occur at about 90 ns, for 1600 cells at 50 ns and for 100 cells at 10 ns. The SiPM with 100 cells have a time of pulse maximum fastest with the smallest broadening because of the longest recovery time, highest PDE, fastest rise time and longest decay time of the single cell signal (Tab. 3.1). For 1600 cells the distribution of times of the pulse maximum is asymmetrical with a tail to the later times of the pulse maxima. This tailing or asymmetry of the distribution causes inaccuracy in the gaussian fit (Fig. 8.4) which is wider and shifted.

Figure 8.5 shows the time of pulse maxima dependency for SiPMs coupled with LaBr. For SiPM with 1600 cells the pulse height maximum position does not change significantly with the deposited energy, only the distribution is narrower. The pulse height maximum time decreases with energy for 400 cells and 100 cells. In the latter it results in a well defined time of the pulse maximum. The reason for this is the saturation of the signal. The pulse height maximum occur at about 6 ns for the SiPM with 100 cells, at 13 ns for 400 cells and 11 ns for 1600 cells. Similar behavior can be observed with NaI and LYSO (Fig. 8.6 and 8.7). The occurrence and stability of the pulse maxima is important for the energy determination with the pulse height detection method.

In figures 8.8 and 8.9 the dependency of the SiPM signal with 1600 cells on the energy deposited in different crystals is seen in the pulse height detection and integration method. Both methods show a linear dependency of the signal

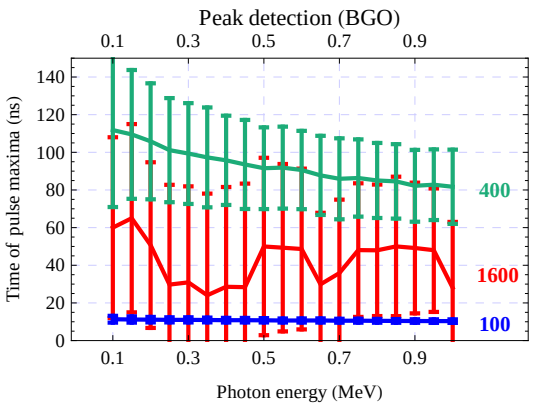

Figure 8.4: Time of pulse maxima versus energy deposited in the BGO crystal for SiPMs with 100, 400 and 1600 cells.

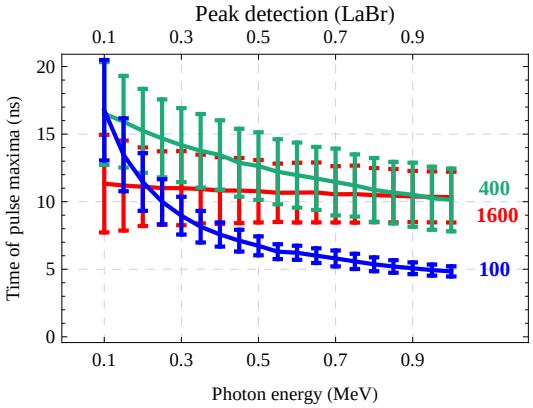

Figure 8.5: Time of pulse maxima versus energy deposited in the LaBr crystal for SiPMs with 100, 400 and 1600 cells.

on deposited the energy even in case of the brightest scintillator. For the signal integration method the signal is proportional to the light yield of the crystal. In case of the pulse height detection method the decay time of the crystal significantly affects the signal. The LYSO crystal with 32000 photons/MeV results in a larger signal than the NaI which emits 37000 photons/MeV. One reason for this behaviour is higher effective PDE of the S10362-11-025C SiPM coupled with the LYSO crystal compared to a coupling with the NaI crystal due to the wavelength sensitivity of the SiPM. However the variation of 0.3% in PDE can not explain the much higher signal of the LYSO crystal in figure 8.8. The effect mainly responsible for this behaviour is the much shorter decay time of the LYSO crystal which strongly affects the pulse height. Since the 1600 cell SiPM single cell pulse has a short decay time (4 ns) the cells which are triggered only affect the summed SiPM for a short time period. For the LaBr crystal there is a huge number of cells fired at the beginning which form a steep and high pulse. In case of NaI the photons impinging onto the SiPM surface arrive with a wider time distribution and therefore the summed pulse builds up more slowly resulting in smaller amplitude.

Figures 8.10 to 8.13 show the nonlinear behaviour of the SiPM signals as a function of deposited energy. In case of the integration method the NaI crystal shows the highest signal as is observed in figure 8.11 and 8.13. The explanation for this is found in the short recovery time (< 20 ns) of the SiPMs compared to the decay time of the NaI crystal (230 ns). Therefore many cells are able to fire

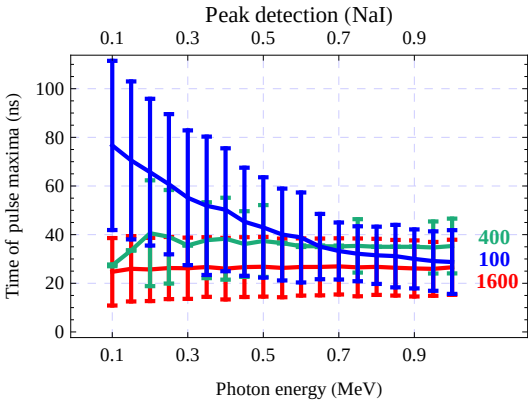

Figure 8.6: Time of pulse maxima versus energy deposited in the NaI crystal for SiPMs with 100, 400 and 1600 cells.

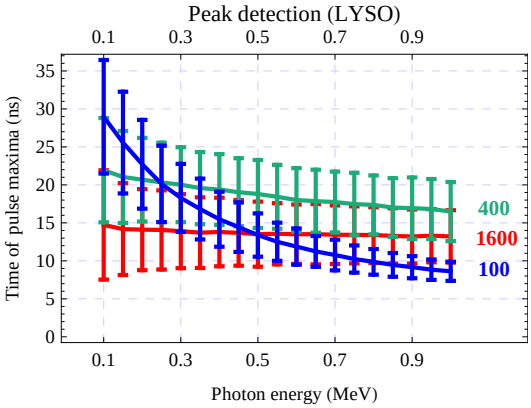

Figure 8.7: Time of pulse maxima versus energy deposited in the LYSO crystal for SiPMs with 100, 400 and 1600 cells.

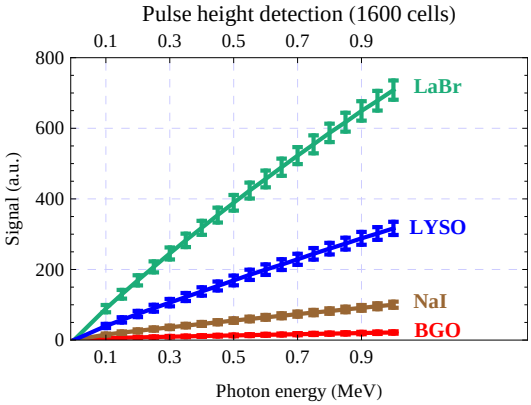

Figure 8.8: Simulated pulse height dependency as a function of the energy deposited in four different crystals for the SiPM with 1600 cells/mm^2.

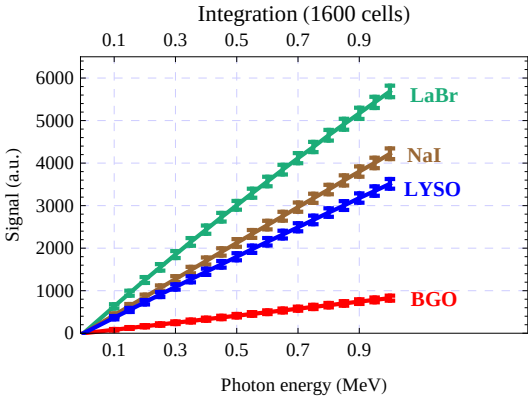

Figure 8.9: Simulated total collected charge as a function of the energy deposited in four different crystals for the SiPM with 1600 cells/mm^2.

more then once with full amplitude. This is however not the case for LYSO and LaBr crystals due to their short decay times (41 ns, 25 ns).

Figure 8.12 shows the complete saturation of the SiPM at higher energies for the pulse height detection method when coupling LaBr, LYSO or NaI crystals to the 100 cell SiPM. Similar behaviour is observed in figure 8.13, only that here the nonlinearity of the detector module combination with the NaI crystal is improved due to the fast recovery process of the SiPM.

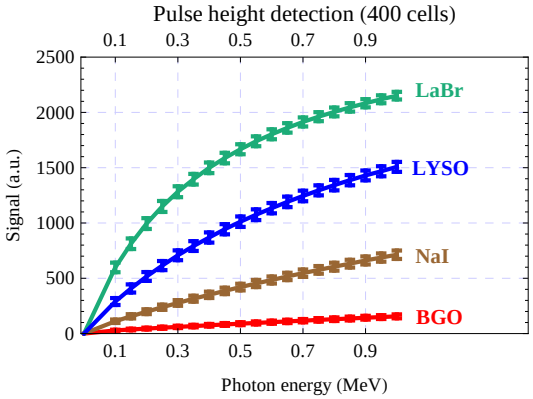

Figure 8.10: Simulated pulse height dependency as a function of the energy deposited in four different crystals for the SiPM with 400 cells/mm^2.

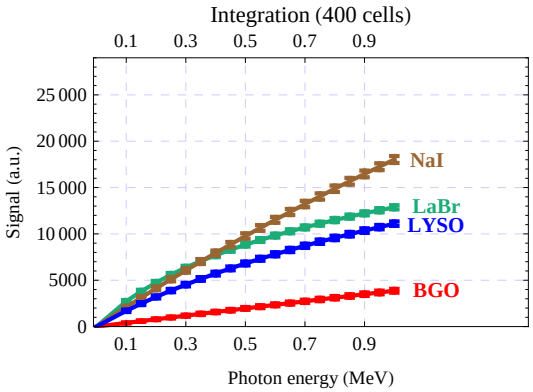

Figure 8.11: Simulated total collected charge as a function of the energy deposited in four different crystals for the SiPM with 400 cells/mm^2.

Figures 8.14-8.19 show the simulated dependency of the energy resolution on the energy of incident γ-rays for three types of SiPMs from Hamamatsu coupled to different scintillating crystals . Two methods were used for the signal analysis: pulse height detection and signal integration. For the S10362-11-025C pulse height detection method shows better performance with fast scintillating crystals (LYSO) compared to the slower crystal with higher light yield (NaI). On the other hand in case of the integration method NaI gives slightly better energy resolution than the LYSO due to the higher light yield. One missing aspect which has to be considered is that the intrinsic energy resolution has to be added to the simulated energy resolution in order to fairly compare different crystals. The intrinsic energy resolution for the investigated crystals is presented in table 8.2, however only measurements for 622 keV can be found in the literature. The degradation of the energy resolution of BGO crystal at higher energies (Fig. 8.14) for the pulse height detection method is due to the slow decay time of the BGO crystal which in combination with the lower PDE of S10362-11-025C results in an unstable pulse height.

For S10362-11-050C the degradation of the energy resolution for both methods at higher energies is observed (Fig. 8.16 and 8.17). That is especially significant when coupling SiPMs with LaBr due to the high light yield of the crystal and lower number of cells of this SiPM type.

S10362-11-100C with only 100 cells suffer from strong nonlinearities when

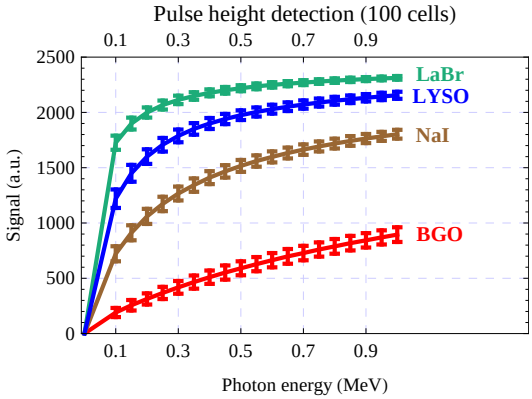

Figure 8.12: Simulated pulse height dependency as a function of the energy deposited in four different crystals for the SiPM with 100 cells/mm^2.

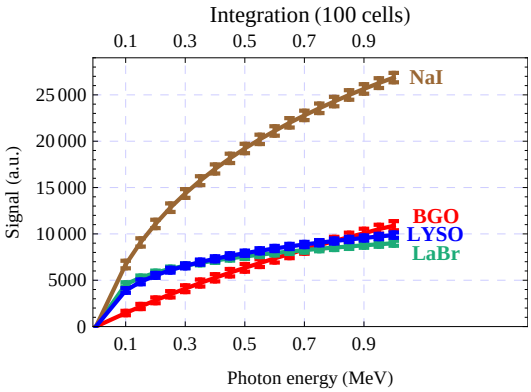

Figure 8.13: Simulated total collected charge as a function of the energy deposited in four different crystals for the SiPM with 100 cells/mm^2.

coupled to NaI, LYSO or LaBr (Fig. 8.18 and 8.19). Nonlinear behaviour makes this type of detector unsuitable for PET when using bright scintillating crystals. NaI shows better performance in case of the integration method due to the recovery process of the SiPM and longer decay time of the crystal. In this case many cells in SiPM fire more than once and by this the dynamic range is increased and the linearity is improved. The cells that fire multiple times also contribute to better counting statistics. In general the integration method results in better energy resolution.

Figures 8.20 and 8.21 compare the performance of the three SiPM types coupled to BGO crystals for pulse height detection and integration method. Since the BGO crystal has only 8000 photons/MeV the best energy resolution is observed with the SiPM with 100 cells for the pulse height detection method. Whereas for the integration method at γ-ray energies above 0.6 MeV the SiPM with 400 cells performs better due to the nonlinear behavior of the configuration with 100 cells. The SiPM with 1600 cells has an unstable pulse height when coupled to the BGO due to low light intensity and long decay time of the scintillator. The consequence is an insufficient energy determination for the pulse height detection method. However with the integration method an energy resolution of about 25% was achieved in the simulation for 511 keV γ-rays.

Figures 8.22 and 8.23 compare the performance of three SiPM types coupled

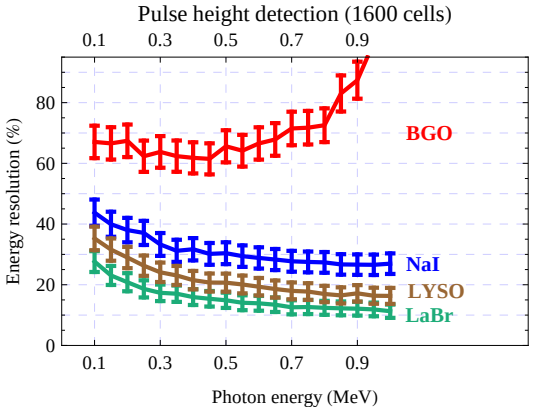

Figure 8.14: Simulated energy resolution for SiPMs with 1600 cells as a function of energy deposited in scintillating crystal for the pulse height detection method.

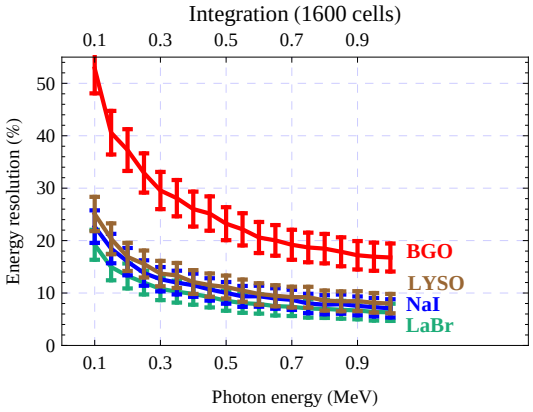

Figure 8.15: Simulated energy resolution for SiPMs with 1600 cells as a function of the energy deposited in the scintillating crystal for the integration method.

to LaBr crystal for the pulse height detection and integration method. The best SiPM candidate for the redout of the setup with the LaBr crystal should be a detector with a number of cells between 400 and 1600. The configuration with 100 cells is left out of consideration as it shows strong nonlinearity. For the pulse height detection method the configuration with 400 cells shows better energy resolution up to about 550 keV due to higher PDE. At energies above 550 keV the configuration with 1600 cells is advantageous since the nonlinearity begins to affect the 400 cells configuration significantly. PET with the demand to detect 511 keV γ-rays is therefore close to the point where both configurations show similar performance (about 15%) in terms of energy resolution. Similar behaviour is observed for the integration method, while the energy resolution of this method is superior (about 9%).

Figures 8.24 and 8.25 show the energy resolution dependency of different SiPM types when coupled to a NaI crystal for the pulse height detection and integration method. The best energy resolution for the pulse height detection method is simulated with the 400 cell SiPM configuration at energies above 350 keV. At energies below this value the SiPM with 100 cells would be advantageous due to the higher PDE. However at energies above 350 keV the SiPM with 100 cells has a strong nonlinear response where the SiPM with 1600 cells has a rather poor energy resolution due to its lower PDE. Despite the fact that the NaI crystal has a high light output, the SiPM with 400 cells does not show saturation problems

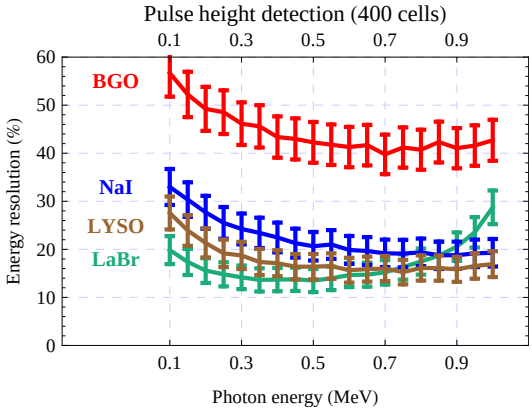

Figure 8.16: Simulated energy resolution for SiPMs with 400 cells as a function of the energy deposited in the scintillating crystal for the pulse height detection method.

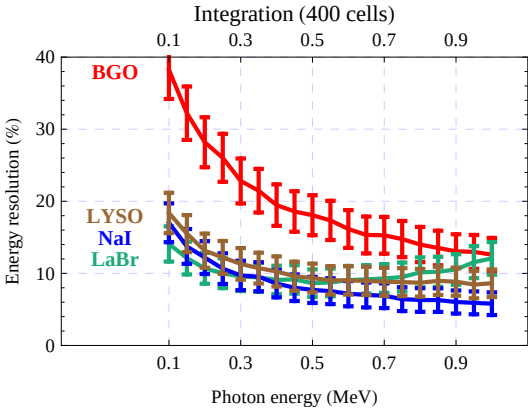

Figure 8.17: Simulated energy resolution for SiPMs with 400 cells as a function of the energy deposited in the scintillating crystal for the integration method.

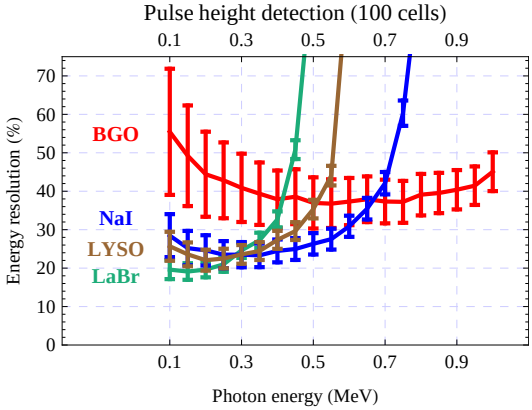

Figure 8.18: Simulated energy resolution for SiPMs with 100 cells as a function of the energy deposited in the scintillating crystal for the pulse height detection method.

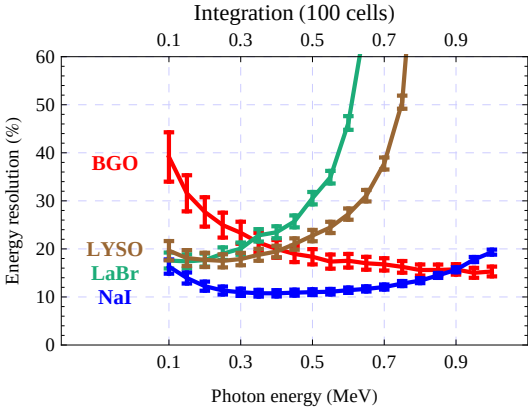

Figure 8.19: Simulated energy resolution for SiPMs with 100 cells as a function of the energy deposited in the scintillating crystal for the integration method.

due to the long decay time of the NaI scintillator. In case of the integration method the SiPM with 400 cells is superior to the other analyzed SiPM types in the complete simulated energy range due to its best compromise between PDE and number of cells. The SiPM with 100 cells does not saturate as strongly in the integration method as in pulse height detection method.

Figures 8.26 and 8.27 show the energy resolution dependency of different SiPM

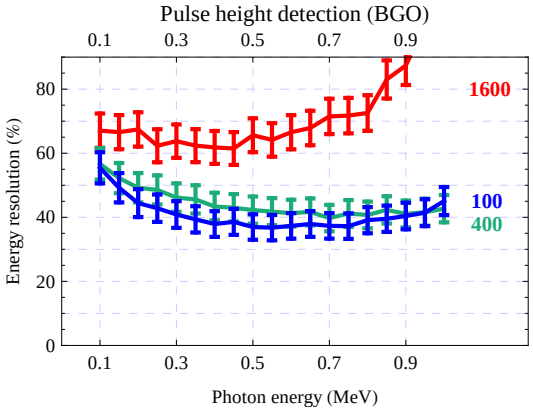

Figure 8.20: Simulated energy resolution for BGO scintillator coupled to different SiPM detectors for pulse height detection method.

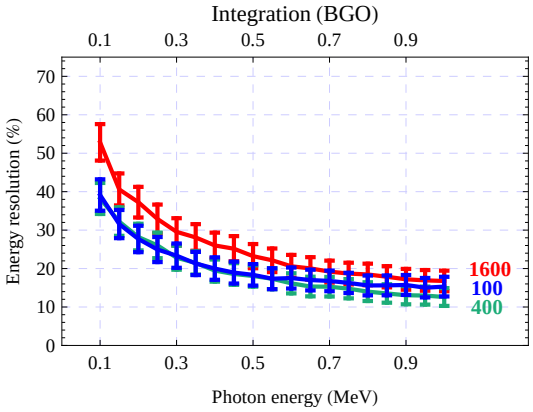

Figure 8.21: Simulated energy resolution for BGO scintillator coupled to different SiPM detectors for integration method.

types when coupled to the LYSO scintillator for the pulse height detection and integration method. Here the SiPM with 400 cells is the best choice for readout in both signal analysis methods. However the integration method results in better energy resolution of about 9% at 511 keV whereas 16% is simulated for the pulse height detection method.

8.3 Conclusion

The simulation of the energy resolution of common crystals for PET in combination with three SiPM types from Hamamatsu Photonics shows promising results for the use of SiPMs as detectors for PET. The simulation can predict and explain the behaviour of detector modules. SiPMs with 400 cells are advantageous photodetectors for PET in combination with LYSO and NaI compared to configurations with 100 and 1600 cells for the pulse height detection method. The best candidates for the readout of BGO are SiPMs with 100 cells resulting in a 37% energy resolution for 511 keV γ-rays. For LaBr SiPMs with 400 and 1600 cells show a similar performance in terms of energy resolution at 511 keV. The best energy resolution of about 14% for 511 keV γ-rays for the pulse hight detection was simulated with LaBr. In combination with 400 or 1600 cell SiPM it has its best energy resolution for the integration method of about 8%. As expected the integration method performs better in terms of energy resolution than the pulse height detection method. Despite the fact that SiPMs have high gain

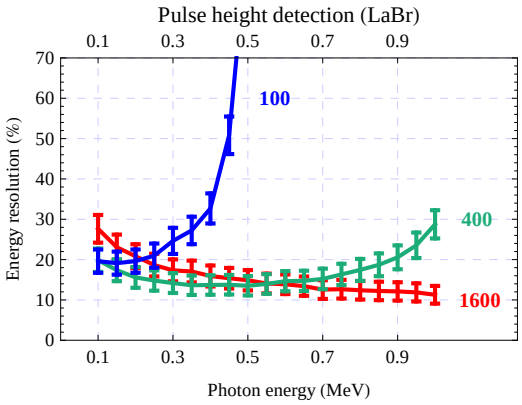

Figure 8.22: Simulated energy resolution for LaBr scintillator coupled to different SiPM detectors for pulse height detection method.

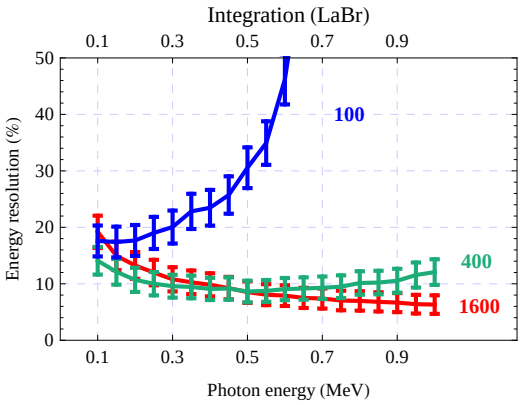

Figure 8.23: Simulated energy resolution for LaBr scintillator coupled to different SiPM detectors for integration method.

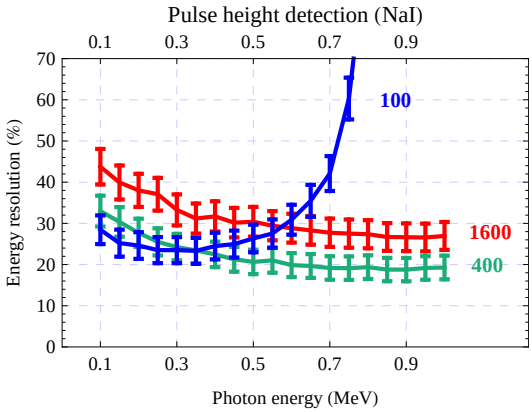

Figure 8.24: Simulated energy resolution for NaI scintillator coupled to different SiPM detectors for pulse height detection method.

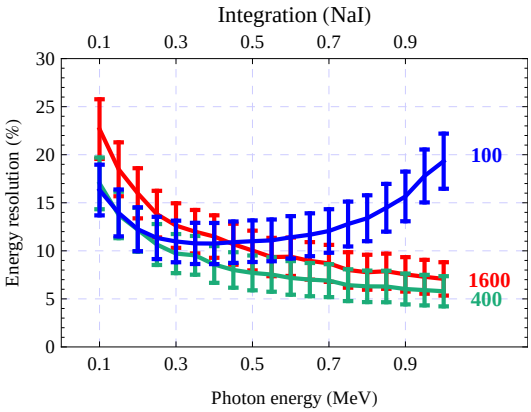

Figure 8.25: Simulated energy resolution for NaI scintillator coupled to different SiPM detectors for integration method.

and consequently strong signals the SiPM signal may be negatively affected by the electronic noise which is not included in the simulation and would affect the integration method stronger than the pulse height detection method.

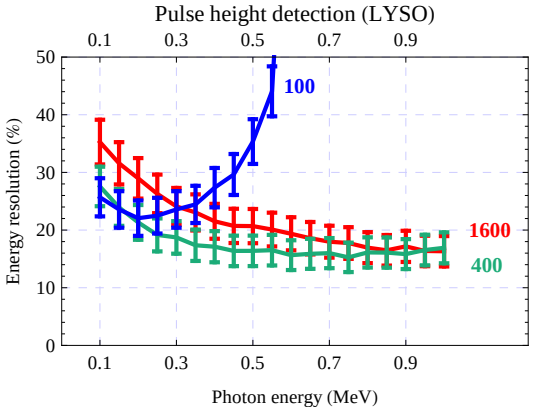

Figure 8.26: Simulated energy resolution for the LYSO scintillator coupled to different SiPMs detectors for the pulse height detection method.

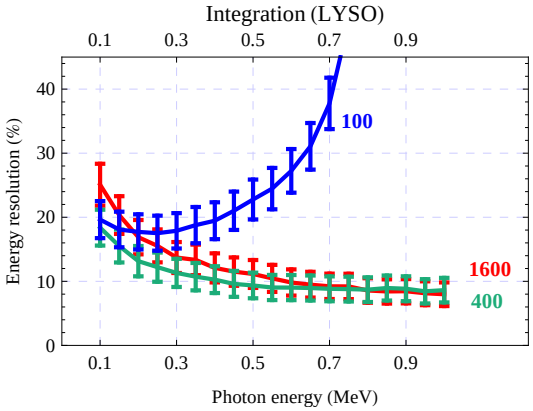

Figure 8.27: Simulated energy resolution for the LYSO scintillator coupled to different SiPMs detectors for the integration method.

p

8. PERFORMANCE OF SIPMS COUPLED TO DIFFERENT SCINTILLATION CRYSTALS

9

Summary and Conclusion

Silicon Photomultipliers (SiPMs) are very promising photodetectors for a number of applications due to their several attractive features. They present the most appropriate candidate for combined PET/MR since they fulfil all the important requirements of such a system. They have a good photon detection efficiency, high gain, good timing performance are compact detectors and are insensitive to magnetic fields.

Measurements with single channel SiPMs coupled to a LYSO scintillating crystal show a strong nonlinear behaviour for the SiPM with 400 cells/mm^2 when operated at the manufacturer recommended bias voltage. Despite the rather poor light collection efficiency of only 20%, which is mainly the consequence of the long tiny crystal used, the number of photons impinging the photodetector times the SiPM's PDE still exceeds the number of cells in this SiPM type. However the energy resolution of the version with 400 cells is still slightly better than that of the SiPM with 1600 cells when coupled to a LYSO crystal after the correction for nonlinear effects. The best energy resolution of $18 \pm 2\%$ was measured with the SiPM with 400 cells at 70.3 V.

The investigated SiPM matrix from Hamamatsu Photonics shows a good spatial uniformity of the sensitivity and gain between individual channels. However some problems of the one-to-one coupling concept arise when coupling the matrix to the scintillation crystal block from Sinocera. Due to the relatively thick epoxy layer of the matrix there is disturbing crosstalk of optical photons between the adjacent cells. There is also crosstalk between the scintillating crystals in the crystal matrix due to the thin layer of reflector material ($BaSO_4$). The last problem is the misalignment of the crystal matrix to the SiPM matrix. Despite all of these facts the crystal identification is still possible by selecting the SiPM chan-

nel with the strongest signal. However the energy resolution degrades drastically compared to single channel SiPM redout. In the SiPM matrix the photopeak can only be determined if the sum of simultaneously triggered channels is calculated. It has to be noted that the Sinocera scintillation crystals, used in the Matrix, have the intrinsic energy resolution of about 20% whereas a LYSO crystal, used for single channel measurements, has a 9% intrinsic energy resolution for 511 keV photons. The investigated SiPM matrix fulfils all expectations and can be used in an PET/MR system with either temperature stabilization or compensation of temperature changes with bias voltage. While a thinner epoxy layer in the SiPM matrix would slightly improve the detector module there is a need for a better LYSO crystal-block for an efficient one-to-one coupling configuration.

The response of the SiPM is affected by many parameters which have complicated dependencies on the temperature and bias voltage. When using SiPMs for the detection of scintillation photons the relationship between incident light and the SiPM's response is nonlinear. To understand and predict the complex SiPM response the analytical and Monte-Carlo based research models have been developed. Analytical models (18, 57, 58) to describe the SiPM signal have the advantage of shorter calculation times for large parameter sets compared to the Monte-Carlo models. However it is difficult to include a large number of processes that occur in SiPMs in analytical models therefore they may be limited in their general applicability. On the other side Monte-Carlo models offer limitless options with regard to the number of effects which can be included and therefore present an important alternative. The first Crystal-SiPM simulation model aiming at performance study developed by Henseler et al. (16) reveals the influence of some basic parameters of SiPMs on PET in terms of the energy and timing performance. However some important SiPM processes are missing in this simplified model. One important effect, only partially included, is the recovery time. Hoverer as the decay time of LYSO is larger than typical recovery times of SiPMs, the recovery process needs to be modeled precisely. Retier et at. (59) simulated the response of SiPMs in a low light environment. Under this condition the saturation effects are not important and were not considered in their model. The focus of their study was the variation of SiPM parameters with bias voltage. The Monte-Carlo based statistical model to study the performance of SiPMs presented in this thesis, simulates all relevant SiPM parameters without any strong simplification.

The Monte-Carlo based SiPM model has been successfully validated with the dark count spectra as well as single photon LED spectra. The combined LYSO-

SiPM model has shown good accordance with the experimental data and offers the possibility to search for the optimal parameters and limitations of SiPM based detector modules. Afterpulses and crosstalk have little influence on the detector performance in terms of energy resolution, while the recovery time governs the performance of the SiPM with 400 cells/mm^2. The model offers the possibility to investigate different configurations of any scintillating crystal coupled to different SiPMs. We used it for a $1 \times 1 \times 20\,\mathrm{mm}^3$ LYSO crystal coupled to Hamamatsu MPPCs with 400 and 1600 cells/mm^2 designed for small animal PET applications. This Crystal-SiPM model with study of influence of different parameters on the energy resolution has been published in (60).

When comparing different types of commercially available SiPMs from Hamamatsu, the S10362-11-050C is advantageous for the readout of the PET with LYSO and NaI. The S10362-11-100C is the best choice when BGO would be used as the scintillating crystal. For LaBr crystals the S10362-11-025C and S10362-11-050C show a similar performance in energy resolution for 511 keV photons. The best energy resolution of all investigated combinations of about 8% is achieved in two cases: when combining the LaBr crystal with the S10362-11-025C and when coupling the NaI crystal with the S10362-11-050C, as in these two cases the integration method results in better performance.

Typical dark count rates for the SiPMs which are below 1 MHz/mm^2 at room temperature are irrelevant for applications in which the expected number of photoelectrons is large compared to one. For general applicability, dark counts were included in the model by including avalanches at random times.

The model established in this study includes almost all relevant SiPM parameters. However, some effects are still missing. The model includes only statistical contributions to the noise of the SiPM; the electronic noise, non-linearity of the crystal and inhomogeneity of the crystal were not considered for this study. One effect of the crosstalk which was not included in the simulations is the additional heating of the detector which affects the overvoltage and indirectly the gain and photon detection efficiency. Another point may be the dependency of the photodetector's quantum efficiency on the angle of impact of the photons (61).

SiPMs are subjects of strong investigation and development at the moment. Better understanding of some effects may lead to the improvement of modeled processes. New measurements will lead to a better accuracy of the model. While for the newly developed SiPM types new processes may be needed in the model.

Appendix A

Basic Variables and Functions of the Simulation Model

This chapter describes the model's basic functions with their functionality, input as well as output parameters.

A.1 Variables

SimPar
: List of parameters to be simulated. List ist automatically distributed between all available kernels. Each parameter set in the list has the following elements:
$Index$, N_C, τ_{Cry}, LY, E, GE, τ_{CRec}, P_a, QE, p_{SAP}, p_{LAP}, p_{CT}, σ_{SiPM}, LCE, δ, τ_{CDec}.

stat
: Number of events to be calculated for each parameter set.

N_C
: Number of cells of the SiPM.

τ_{Cry}
: Crystal decay time constant in nanoseconds.

LY
: Crystal light yield.

A. BASIC VARIABLES AND FUNCTIONS OF THE SIMULATION MODEL

photons
: Matrix of the incident photons on the active surface of the SiPM. List has following form

$$photons = \begin{bmatrix} x_1 & y_1 & t_1 \\ x_2 & y_2 & t_2 \\ \vdots & \vdots & \vdots \\ x_n & y_n & t_n \end{bmatrix}$$

E
: Energy deposited in the crystal in keV.

GE
: Geometrical efficiency of the SiPM.

τ_{CRec}
: Single cell recovery time.

P_a
: Probability for geiger discharge.

QE
: Quantum efficiency.

p_{SAP}
: Probability for an afterpulse with a short time constant process.

p_{LAP}
: Probability for an afterpulse with a long time constant process.

p_{CT}
: Crosstalk probability.

LCE
: Light collection efficiency.

δ
: SiPMs single cell rise time.

τ_{CDec}
: SiPMs single cell decay time.

Index

Index of simulated parameter set.

BPrintAvalanches

If set to *True* the function SiPMAvalanches generates an *avalanches.txt* file which includes the time, gain and type (triggered by photon, dark count, crosstalk or afterpulse) for each avalanche.

SiPM

Matrix in which all avalanches (time, gain) for all cells in SiPM are stored. The matrix has following form

$$SiPM = \begin{bmatrix} \begin{bmatrix} t_{111} & A_{111} \\ t_{112} & A_{112} \\ \vdots & \vdots \\ t_{11n} & A_{11n} \end{bmatrix} & \begin{bmatrix} t_{122} & A_{121} \\ t_{122} & A_{122} \\ \vdots & \vdots \\ t_{12n} & A_{12n} \end{bmatrix} & \cdots & \begin{bmatrix} t_{1k1} & A_{1k1} \\ t_{1k2} & A_{1k2} \\ \vdots & \vdots \\ t_{1kn} & A_{1kn} \end{bmatrix} \\ \begin{bmatrix} t_{211} & A_{211} \\ t_{212} & A_{212} \\ \vdots & \vdots \\ t_{21n} & A_{21n} \end{bmatrix} & \begin{bmatrix} t_{221} & A_{221} \\ t_{222} & A_{222} \\ \vdots & \vdots \\ t_{22n} & A_{22n} \end{bmatrix} & \cdots & \begin{bmatrix} t_{2k1} & A_{2k1} \\ t_{2k2} & A_{2k2} \\ \vdots & \vdots \\ t_{2kn} & A_{2kn} \end{bmatrix} \\ \vdots & \vdots & \ddots & \vdots \\ \begin{bmatrix} t_{N11} & A_{N11} \\ t_{N12} & A_{N12} \\ \vdots & \vdots \\ t_{N1n} & A_{N1n} \end{bmatrix} & \begin{bmatrix} t_{N22} & A_{N21} \\ t_{N22} & A_{N22} \\ \vdots & \vdots \\ t_{N2n} & A_{N2n} \end{bmatrix} & \cdots & \begin{bmatrix} t_{Nk1} & A_{Nk1} \\ t_{Nk2} & A_{Nk2} \\ \vdots & \vdots \\ t_{Nkn} & A_{Nkn} \end{bmatrix} \end{bmatrix}$$

A.2 Functions

Response[*SimPar*, *index*, *stat*, *BSignalAnalysis*, *BPrintAvalanches*]

The main function of the simulation of the SiPM performance. This function calls all other functions to generate SiPM avalanches (*SiPMAvalanches*) from which the mathematical SiPM signal is generated and analysed using peak detection and integration method (*SiPMSignalAnalysis*). Function repeats the simulation for each parameter set for number of times defined by the parameter *stat*. Results of simulation are fitted with gaussian functions and parameters of fits are stored in an out.txt file for later analysis.

A. BASIC VARIABLES AND FUNCTIONS OF THE SIMULATION MODEL

SignalAnalysis[$avalanches$, τ_{CRis}, τ_{CDec}, t_{min}, t_{max}, dt]
Generates a mathematical signal from a list of avalanches. The signal is then analysed using pulse height detection and integration method.

RandomPhotons[N_C, $nrPhotons$, t_{max}, GE]
Generates list of uniformly distributed photons between time t_{min} and t_{max}.

RandomPhotonsExp[N_C,τ_{Cry}, $nrPhotons$, GE]
Generates list of exponentially distributed photons with decay time constant τ_{Cry}.

SingleAvalancheSignal[t, δ, τ_{CDec}, t_i, G]
Returns signal of single cell with linear rise time and exponential decay time.

Neighbours[x_i,y_i,N_C]
Returns the nearest and second nearest neighbours of the cell (x_i, y_i) in SiPM with N_C cells.

Amplitudes[N_C, σ]
Generates a gaussian profile for SiPM cell gain.

NLModel[$Nrphotons$, N_C, A, B]
Fits model for SiPM response (Eq. 2.10).

NLCorrection[k, A, B, N_C, V_i]
Corrects the SiPM's nonlinear response (Chapter 2.5.2).

V_{bias} (V)	A	B	$10^3 * k$
69.1	7.74×10^7	1.37×10^6	0.0442
69.3	30.2	1.34	0.111
69.5	5.35	0.466	0.218
69.7	2.93	0.418	0.357
69.9	2.59	0.523	0.505
70.1	1.91	0.545	0.715
70.3	1.62	0.614	0.946
70.5	1.36	0.671	1.23
70.7	1.1	0.719	1.63
70.9	0.845	0.724	2.14
71.	0.781	0.759	2.43
71.1	0.728	0.797	2.74

Table B.1: Fitted parameters of nonlinear response of the LYSO-SiPM peak position measured at different bias voltages for S10362-11-050C (400 cells/mm^2).

V_{bias} (V)	A	B	$10^3 * k$
71.	1.04×10^7	2.49×10^6	0.149
71.2	1.35×10^7	3.86×10^6	0.179
71.4	7.27×10^6	2.43×10^6	0.209
71.6	30.8	12.2	0.247
71.8	24.4	11.2	0.288
72.	2.87×10^7	1.52×10^7	0.331
72.2	13.2	8.34	0.396
72.4	2.32	1.86	0.5
72.6	1.8	1.75	0.606
72.8	0.927	1.18	0.798
72.9	0.768	1.13	0.916
73.	0.663	1.1	1.04

Table B.2: Fitted parameters of nonlinear response of the LYSO-SiPM peak position measured at different bias voltages for S10362-11-025C (1600 cells/mm^2).

Appendix B

Tables of Measurements

B.1 Tables of Measurements of a Single Channel SiPMs Coupled to the $LYSO$

Table B.2 shows the fitted parameters of the nonlinear response model of the LYSO-SiPM for pulse the height detection method. Measurements were performed at different bias voltages. Details about the measurements are presented in chapter 3

SiPM: S10362-11-50C , Source: Co, Energy: 122 keV
Coefficient of determination R^2: 0.999635

	Estimate	Standard Error	t-Statistic	P-Value
A	0.016	0.00402	3.98	0.00405
B	0.0721	0.00385	18.7	6.93×10^{-8}
V_0	69.1	0.0598	1160.	3.53×10^{-22}

SiPM: S10362-11-50C , Source: ^{99m}Tc, Energy: 140 keV
Coefficient of determination R^2: 0.999668

	Estimate	Standard Error	t-Statistic	P-Value
A	0.0178	0.00449	3.96	0.00418
B	0.0753	0.00402	18.7	6.8×10^{-8}
V_0	69.1	0.0616	1120.	4.46×10^{-22}

SiPM: S10362-11-50C , Source: Ba, Energy: 356 keV
Coefficient of determination R^2: 0.999903

	Estimate	Standard Error	t-Statistic	P-Value
A	0.00348	0.00872	0.398	0.701
B	0.0929	0.00391	23.8	1.04×10^{-8}
V_0	68.7	0.0663	1040.	8.47×10^{-22}

SiPM: S10362-11-50C , Source: ^{131}I, Energy: 364 keV
Coefficient of determination R^2: 0.999964

	Estimate	Standard Error	t-Statistic	P-Value
A	−0.0229	0.00499	−4.59	0.00132
B	0.0809	0.00182	44.3	7.56×10^{-12}
V_0	68.4	0.0393	1740.	3.51×10^{-26}

SiPM: S10362-11-50C , Source: ^{18}F, Energy: 511 keV
Coefficient of determination R^2: 0.998799

	Estimate	Standard Error	t-Statistic	P-Value
A	−0.294	0.175	−1.68	0.127
B	0.0379	0.0118	3.21	0.0107
V_0	66.2	1.21	54.6	1.17×10^{-12}

SiPM: S10362-11-50C , Source: ^{137}Cs, Energy: 662 keV
Coefficient of determination R^2: 0.999981

	Estimate	Standard Error	t-Statistic	P-Value
A	−0.139	0.0163	−8.56	0.0000268
B	0.0754	0.0025	30.2	1.58×10^{-9}
V_0	67.6	0.0864	783.	7.95×10^{-21}

Figure B.1: Results of the fits of the quadratic model of the photopeak dependency on bias voltage. The measured photopeak positions are uncorrected for nonlinear effects.

SiPM: S10362-11-25C , Source: Co, Energy: 122 keV
Coefficient of determination R^2: 0.997607

	Estimate	Standard Error	t-Statistic	P-Value
A	0.0298	0.00285	10.4	0.0000161
B	0.0423	0.00605	7.	0.000212
V_0	71.5	0.108	660.	4.83×10^{-18}

SiPM: S10362-11-25C , Source: ^{99m}Tc, Energy: 140 keV
Coefficient of determination R^2: 0.997587

	Estimate	Standard Error	t-Statistic	P-Value
A	0.023	0.00224	10.3	2.81×10^{-6}
B	0.0324	0.00338	9.59	5.06×10^{-6}
V_0	71.2	0.0926	768.	5.45×10^{-23}

SiPM: S10362-11-25C , Source: Ba, Energy: 356 keV
Coefficient of determination R^2: 0.999644

	Estimate	Standard Error	t-Statistic	P-Value
A	0.0977	0.0146	6.69	0.00259
B	0.113	0.0218	5.2	0.00653
V_0	71.6	0.167	428.	1.79×10^{-10}

SiPM: S10362-11-25C , Source: ^{131}I, Energy: 364 keV
Coefficient of determination R^2: 0.998956

	Estimate	Standard Error	t-Statistic	P-Value
A	0.0635	0.00454	14.	2.06×10^{-7}
B	0.069	0.00563	12.3	6.41×10^{-7}
V_0	71.1	0.081	878.	1.65×10^{-23}

SiPM: S10362-11-25C , Source: ^{18}F, Energy: 511 keV
Coefficient of determination R^2: 0.99969

	Estimate	Standard Error	t-Statistic	P-Value
A	0.108	0.0069	15.6	1.09×10^{-6}
B	0.093	0.00754	12.3	5.31×10^{-6}
V_0	71.2	0.0847	841.	8.89×10^{-19}

SiPM: S10362-11-25C , Source: ^{137}Cs, Energy: 662 keV
Coefficient of determination R^2: 0.999787

	Estimate	Standard Error	t-Statistic	P-Value
A	0.14	0.00779	17.9	4.15×10^{-7}
B	0.11	0.0079	14.	2.28×10^{-6}
V_0	71.2	0.0772	921.	4.68×10^{-19}

Figure B.2: Results of the fits of the quadratic model of the photopeak dependency on bias voltage. The measured photopeak positions are uncorrected for nonlinear effects.

Appendix C

Dark Counts

Figures C.1 and C.2 show the dependency of the probability for a certain number of triggered cells in the time window for dark counts. Dark count rate was set to 1 MhZ. Crosstalk and afterpulses are excluded form this calculation. Figure C.2 shows that probability for more than 1 triggered cell in a time window below 100 ns is under 10%. The probability for more than two triggered cells is negligible.

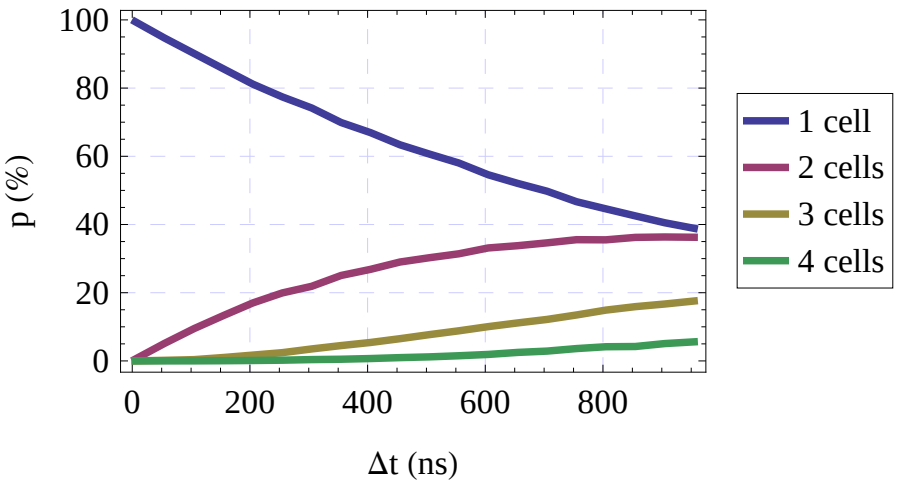

Figure C.1: Simulated dependency of probability for a certain number of triggered cells due to the dark counts in the time window. Dark count rate of 1 MhZ was used but all other effects were excluded from the simulation (crosstalk, afterpulses).

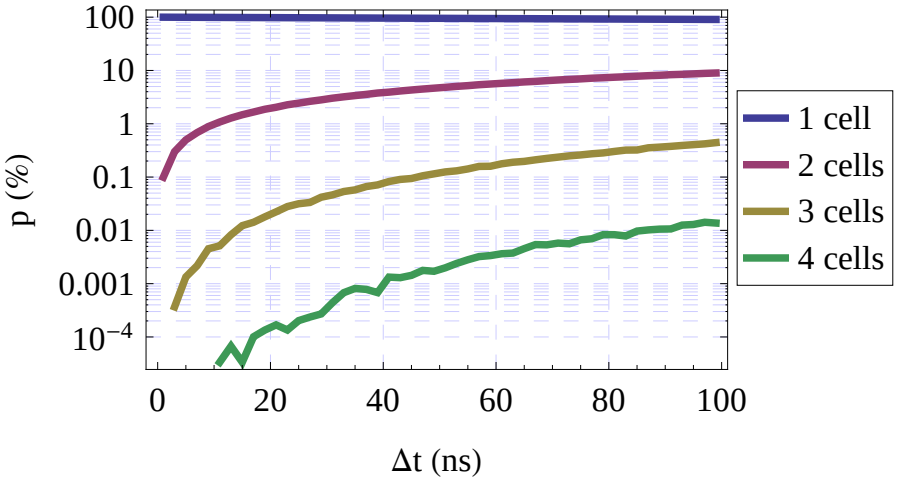

Figure C.2: Simulated dependency of probability for a certain number of triggered cells due to the dark counts in the time window. Dark count rate of 1 MhZ was used but all other effects were excluded from the simulation (crosstalk, afterpulses).

Appendix D

Direct Photons

Consider a 511 keV photoelectric absorbtion at a certain position in the crystal. The scintillating photons are emitted with equal probability in every direction and only some of them directly hit the detector. That portion is equal to the fractional solid angle covered by the detector. The solid angle is defined by

$$\Omega = \iint_S \frac{\mathbf{r} \cdot \mathbf{dS}}{r^3}. \tag{D.1}$$

Consider interaction of the photon in the crystal at position $(x_0,\ y_0\ , z_0)$, and the geometry of the crystal and detector as shown in figure D.1. Equation D.1 can then be rewritten to

$$\Omega = \int_{-\frac{a}{2}}^{\frac{a}{2}} \int_{-\frac{a}{2}}^{\frac{a}{2}} \frac{z_0}{\left((x-x_0)^2 + (y-y_0)^2 + (z-z_0)^2\right)^{\frac{3}{2}}} dxdy \tag{D.2}$$

which can be integrated numerically. In figure D.2 results for the equation D.2 are presented. Here the data for crystal intersection as presented in figure D.1 by the brown surface can be seen. Due to the symmetry the same plot is true for the y axis. At the interaction points of the γ-photon 2 mm away from the detector less than 2% of generated photons directly hit the detector.

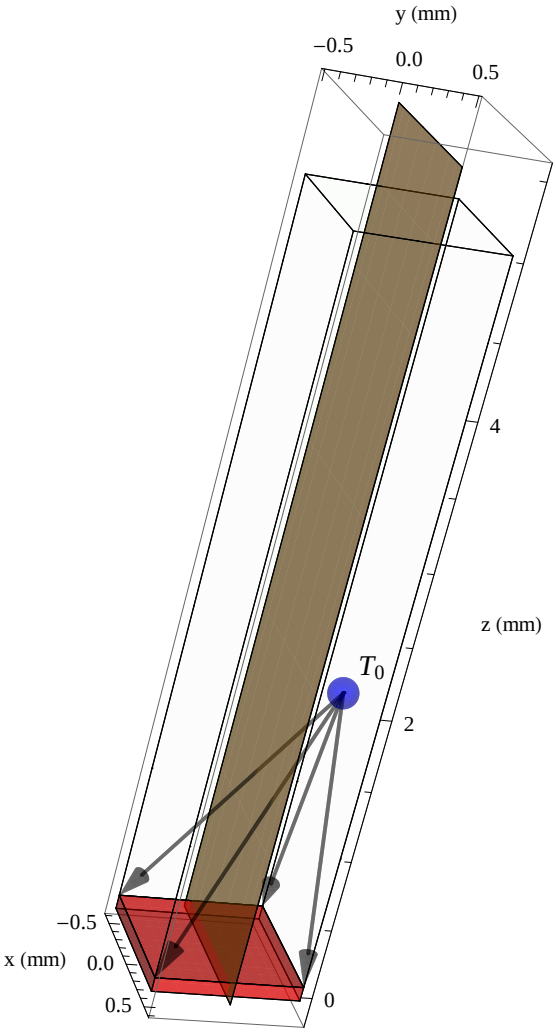

Figure D.1: A rectangular detector of $a \times a$ placed under the scintillating crystal. Gamma interaction point located at A_0 above a detector with rectangular aperture is plotted by a red square.

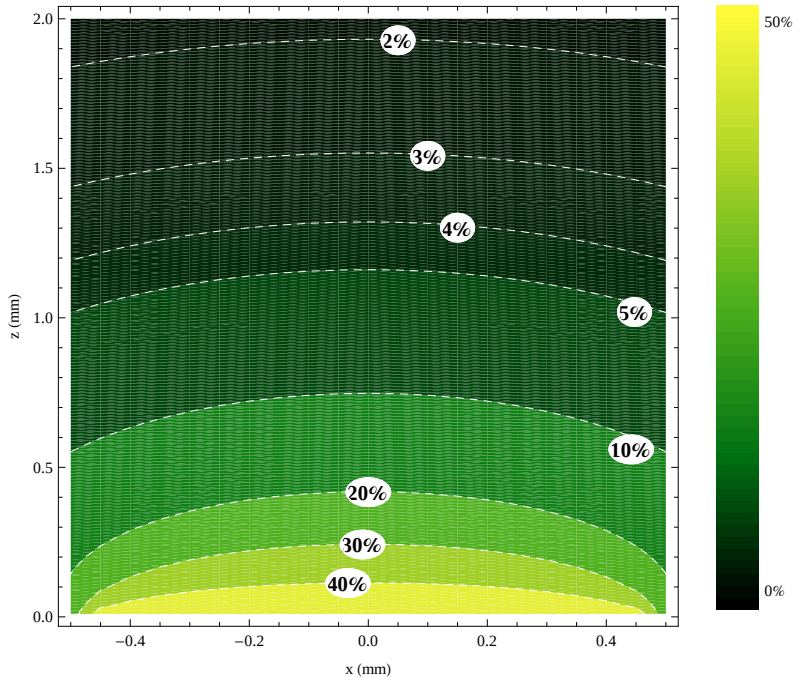

Figure D.2: Part of the direct photons depending on the position in the crystal (scan over the brown plane in figure D.1).

Appendix E

Publications and Active Participation in Academic Conferences

I **Pulko, J.**, F. R. Schneider, A. Velroyen, D. Renker, and S. I. Ziegler., **A Monte-Carlo model of a SiPM coupled to a scintillating crystal**, JINST 7 P02009p

II **Pulko, J.**, A. Verloyen, et al. (2010), **Ein Monte-Carlo basiertes Modell fr die Signalbildung eines Silizium-Photomultipliers**, Deutsche Gesellschaft fr Medizinische Physik, Freiburg, Prsentation

III **Pulko, J.**, A. Verloyen, et al. (2010), **Monte Carlo Based Study on Influence of SiPM Specification on Detector Performance for PET/MR**, Nuclear Science Symposium, Knoxwille, Prsentation

IV **Pulko, J.**, M. Hohberg, et al. (2010), **Monte Carlo based study on influence of SiPM specification on detector performance for PET/MR**, SNM Annual Meeting, Salt Lake City, Prsentation

V **Pulko, J.**, M. Hohberg, et al. (2009), **Monte-Carlo simulations of LYSO-SiPM Module**, Nuclear Science Symposium Conference, Orlando, Poster

VI **Pulko, J.**, S. Fuerst, et al. (2009), **Ein neuartiges Detektormodul basierend auf Einzelkanal-Auslese von LYSO-Kristallen mit einer**

Matrix von Silizium-Photomultipliern, Deutschen Gesellschaft fr Nuklearmedizin, Leipzig, Prsentation

VII **Pulko, J.**, R. Dolenec, et al. (2009), **Surface scan of Hamamatsu** 1×4 **SiPM array**, 11th European Symposium on Semiconductor Detectors, Vildbad Kreuth, Poster

VIII **Pulko, J.**, S. Fuerst, et al. (2008), **Erste Studie eines neuen PET-Detektormoduls, basierend auf der Einzelauslese von** $1 \times 1\,\mathrm{mm}^2$ **LYSO-Kristallen mit monolithischen Arrays von SiPMs**, Deutsche Gesellschaft fr Medizinische Physik, Oldenburg, Poster

IX Fuerst, S., **Pulko, J.**, et al. (2008), **First Studies of a Novel PET Detector Module Based on Individual Redout of** $1 \times 1\,\mathrm{mm}^2$ **LSYO Crystals by Monolithic Array of SiPMs**, Nuclear Science Symposium Conference, IEEE, Dresden, Poster

Glossary

C_C

SiPM Cell Capacitance. 6, 11, 32

DCR

Dark Count Rate. 16, 50

GE

Geometrical Efficiency. 7, 85, 86, 88

G

SiPM Gain. 6, 11, 88

N_C

Number of Cells in SiPM. 12, 14, 16, 50, 57, 85, 88

P_a

Probability for an avalanche. 7, 85, 86

QE

Quantum Efficiency. 7, 85, 86

R_q

Quenching resistance. 6, 11

S_0

Standardized SiPM signal. 6, 7

V_{BD}

Breakdown Voltage. 6, 32

V_{Bias}

BiasVoltage. 6, 7, 32

V_{OV}

Overvoltage. 9, 101

δ

SiPM single cell rise time. 16, 43, 47, 50, 85, 86, 88

τ_{CDec}

SiPM single Cell decay time. 6, 16, 43, 47, 50, 85, 86, 88

τ_{CRec}

SiPM single Cell recovery time. 11, 16, 50, 51, 85, 86

τ_{LAP}

Long Afterpulse time constant. 16, 46, 50, 51

τ_{SAP}

Short Afterpulse time constant. 16, 46, 50, 51

p_{CT}

Crosstalk probability. 16, 45, 50, 85, 86

p_{LAP}

Probability of an afterpulse with long time constant. 16, 46, 50, 51, 85, 86, 105

p_{SAP}

Probability of an afterpulse with short time constant. 16, 46, 50, 51, 85, 86, 105

q_0

Elementary charge $1.602176565 \times 10^{-19}$ coulombs. 6, 32

ADC

Analog to Digital Converter. 29, 38

APD

Avalanche Photodiode is a highly sensitive semiconductor electronic device that exploits the photoelectric effect to convert light to electricity. 5, 6

BGO

Bismuth Germanium Oxide scintillation crystal. 56, 63–66, 68–70, 72, 73, 76, 83, 107, 108

CT

Computed Tomography is a medical imaging technique used to generate a three-dimensional image of the inside of an object from a large series of two-dimensional X-ray images taken around a single axis of rotation. 1

FWHM

Full Width at Half Maximum. 20, 28, 57, 111

G-APD

Geiger-mode Avalance Photodiode is a photodetector built from an avalanche photodiode (APD) array on common silicon substrate operated in Geiger mode. 5

GEANT4

Geometry and Tracking, MC simulation software. 43, 44, 54, 104

GM-APD

Geiger-mode Avalance Photodiode is a photodetector built from an avalanche photodiode (APD) array on common silicon substrate operated in Geiger mode. 5

LaBr

Cerium-doped Lanthanum Bromide scintillation crystal. 56, 63–65, 67–74, 76, 77, 83, 107, 108

LCE

Light Ccollection Efficiency. 85, 86

LED

Light-Emitting Diode. 3, 49, 50, 82

LOR

Line Of Response is a straight line connecting two detectors triggered in a coincidence. 21

LY

Light Yield is the number of photons emitted per unit of deposited energy. 85

LYSO

Cerium doped Lutetium Yttrium Orthosilicate scintillation crystal ($Ce : Lu_{2(1-x)}Y_{2x}SiO_5$). 2, 3, 13, 15, 17–23, 37–39, 42, 54–56, 58, 63–73, 76, 78, 81–83, 89, 102, 104, 107, 108, 111

MPPC

Multi-Pixel Photon Counter is a photodetector built from an avalanche photodiode (APD) array on common silicon substrate substrate operated in Geiger mode. 5, 9, 11, 16, 27, 28, 43, 49, 55, 57, 58, 63, 83, 101, 103

MRI

Magnetic Resonance Imaging is a medical imaging technique used in radiology to visualize detailed internal structures. 1–3, 63

NaI

Thallium doped Sodium Iodide scintillation crystal. 63–66, 68–77, 83, 107, 108

PCB

Printed Circuit Board. 28

PDE

Photon Detection Efficiency. 5, 7, 8, 10, 12, 13, 15, 16, 18–20, 23, 50, 53, 54, 56, 64, 69, 70, 72, 74, 75, 101, 105

PET

Positron Emission Tomography is nuclear medicine imaging technique that produces a three-dimensional image or picture of functional processes in the body. 1–3, 12, 20, 37, 53, 56, 58, 63–66, 73, 74, 76, 83, 111

PIN

A diode with a wide, lightly doped 'near' intrinsic semiconductor region between a p-type semiconductor and an n-type semiconductor region. 5

PMT

Photomultiplier Tube. 5

$PreLude^{TM}$ 420

Cerium doped Lutetium Yttrium Orthosilicate scintillation crystal ($Ce : Lu_{1.8}Y_{0.2}SiO_5$). 15, 67

S10362-11-025C

$1 \times 1\,\mathrm{mm}^2$ SiPM form Hamamatsu Photonics with $25\,\mu$m cell size on ceramic holder. 15, 16, 57, 63, 70, 72, 83, 89, 111

S10362-11-050C

$1 \times 1\,\mathrm{mm}^2$ SiPM form Hamamatsu Photonics with $50\,\mu$m cell size on ceramic holder. 15, 16, 49–52, 57, 63, 72, 83, 89, 101, 105, 111

S10362-11-100C

$1 \times 1\,\mathrm{mm}^2$ SiPM form Hamamatsu Photonics with $100\,\mu$m cell size on ceramic holder. 15, 16, 63, 72, 83

SADC

Sampling Analog to Digital Converter. 38, 39, 111

SiPM

Silicon Photomultipliers is a photodetector built from an avalanche photodiode (APD) array on common silicon substrate operated in Geiger mode. ii, 2, 3, 5–24, 27–39, 41–46, 49–61, 63, 64, 66–78, 81–83, 85–89, 101–108, 111

SPAD

Single Photon Avalanche Diode is a photodetector built from an avalanche photodiode (APD) array on common silicon substrate substrate operated in Geiger mode. 5

SSPM

Solid State Photomultiplier is a photodetector built from an avalanche photodiode (APD) array on common silicon substrate substrate operated in Geiger mode. 5

List of Figures

LIST OF FIGURES

List of Tables

LIST OF TABLES

Bibliography

[1] Michael E. Phelps. *PET: Physics, Instrumentation, and Scanners*. Springer, 2006. 1

[2] Bernd J Pichler, Et al., Martin S Judenhofer, Ciprian Catana, Jeffrey H Walton, Manfred Kneilling, Robert E Nutt, Stefan B Siegel, Claus D Claussen, and Simon R Cherry. **Performance test of an LSO-APD detector in a 7-T MRI scanner for simultaneous PET/MRI**. *J Nucl Med*, **47**[4]:639, 2006. 2

[3] Sri Harsha Maramraju, S David Smith, Sachin S Junnarkar, Daniela Schulz, Sean Stoll, Bosky Ravindranath, Martin L Purschke, Sergio Rescia, Sudeepti Southekal, Jean-François Pratte, Paul Vaska, Craig L Woody, and David J Schlyer. **Small animal simultaneous PET/MRI: initial experiences in a 9.4 T microMRI.** *Physics in medicine and biology*, **56**[8]:2459–80, April 2011. doi:10.1088/0031-9155/56/8/009. 2

[4] P. Buzhan et al. **Silicon photomultiplier and its possible applications**. pages 48–52. Elsevier Science Bv. ISI Document Delivery No.: 685AG Times Cited: 67 Cited Reference Count: 12. 2

[5] G. Llosa et al. **Characterization of a PET detector head based on continuous LYSO crystals and monolithic, 64-pixel silicon photomultiplier matrices**. *Physics in Medicine and Biology*, **55**[23]:7299–7315, 2010. 680UN Times Cited:0 Cited References Count:23. doi:10.1088/0031-9155/55/23/008. 2

[6] D. R. Schaart et al. **A novel, SiPM-array-based, monolithic scintillator detector for PET**. *Physics in Medicine and Biology*, **54**[11]:3501–3512, 2009. 10.1088/0031-9155/54/11/015. 2

[7] N. Otte et al. **The potential of SiPM as photon detector in astroparticle physics experiments like MAGIC and EUSO**. *Nucl. Phys. B Proc. Sup.*, **150**:144–149, 2006. doi:10.1016/j.nuclphysbps.2004.10.084. 2

[8] N. Dinu et al. **Characteristics of a prototype matrix of Silicon PhotoMultipliers (SiPM)**. *Journal of Instrumentation*, **4**, 2009. 10.1088/1748-0221/4/03/P03016. 2

[9] S. Espana et al. **Performance Evaluation of SiPM Photosensors in the Presence of Magnetic Fields**. *La Rabida 2009: International Scientific Meeting on Nuclear Physics*, **1231**:171–172, 2010. Bro49 Times Cited:0 Cited References Count:2 AIP Conference Proceedings. 2

[10] S. Espana et al. **Performance Evaluation of SiPM Detectors for PET Imaging in the Presence of Magnetic Fields**. *2008 Ieee Nuclear Science Symposium and Medical Imaging Conference (2008 Nss/Mic), Vols 1-9*, pages 2866–2870, 2009. Bkn17 Times Cited:0 Cited References Count:6 Ieee Nuclear Science Symposium - Conference Record. 2

[11] Sul Woo-Suk et al. **Guard-Ring Structures for Silicon Photomultipliers**. *IEEE Trans. Electron. Dev.*, **31**[1]:41–43, 2010. doi:10.1109/LED.2009.2035829. 2, 10

[12] C. Merck et al. **Back Illuminated Drift Silicon Photomultiplier as Novel Detector for Single Photon Counting**. In *IEEE NSS CONFERENCE RECORD*, **3**, pages 1562–1565, 2006. 2, 7

[13] C. Degenhardt et al. **The digital Silicon Photomultiplier — A novel sensor for the detection of scintillation light**. In *IEEE NSS CONFERENCE RECORD*, pages 2383–2386, 2009. 2

[14] J. Ninkovic et al. **SiMPl-Novel high QE photosensor**. *Nucl. Instrum. Meth. A*, **610**[1]:142–144, 2009. doi:10.1016/j.nima.2009.05.182. 2, 8

[15] G. Q. Zhang et al. **Demonstration of a silicon photomultiplier with bulk integrated quenching resistors on epitaxial silicon**. *Nucl. Instrum. Meth. A*, **621**[1-3]:116–120, 2010. doi:10.1016/j.nima.2010.04.040. 2, 8

[16] D. Henseler et al. **SiPM Performance in PET Applications: An Experimental and Theoretical Analysis**. In *IEEE NSS CONFERENCE RECORD*, pages 1941–1948, 2009. 2, 82

[17] D. Liksonov et al. **Development of a simulation tool to predict the behavior of a SiPM detector coupled to a scintillation crystal**. In *IEEE NSS Conference Record*, pages 1747–1751. IEEE, 2010. 2

[18] H. T. van Dam et al. **A Comprehensive Model of the Response of Silicon Photomultipliers**. *IEEE Trans. Nucl. Sci.*, **57**[4]:2254–2266, 2010. doi:10.1109/TNS.2010.2053048. 2, 82

[19] D. Renker and E. Lorenz. **Advances in solid state photon detectors**. *JINST*, **4**[04]:P04004, 2009. 5, 8

[20] V. Golovin. **Avalanche photodetector**, 1998, Patent No. RU 2142175. 5

[21] Z. Sadygov. **Avalanche detector**, 1998, Patent No. RU 2102820. 5

[22] H. Otono et al. **Study of the internal mechanisms of Pixelized Photon Detectors operated in Geiger-mode**. *0808.2541*, 2008. 6

[23] F. Corsi et al. **Electrical Characterization of Silicon Photo-Multiplier Detectors for Optimal Front-End Design**. In *Nuclear Science Symposium Conference Record, 2006. IEEE*, **2**, pages 1276–1280. 10.1109/NSSMIC.2006.356076. 6

[24] Hamamatsu Photonics Deutschland GmbH, SiPM (http://sales.hamamatsu.com/de/produkte/solid-state-division/si-photodiode-series). 7, 15, 16, 49, 50, 64, 113, 117

[25] J. Ninkovic. **Recent developments in silicon photomultipliers**. *Nucl. Instrum. Meth. A*, **580**[2]:1020–1022, 2007. doi:10.1016/j.nima.2007.06.059. 7

[26] H. G. Moser. **Development of Back Illuminated SiPM at the MPI Semiconductor Laboratory**. 2007. 7

[27] Jelena Ninkovic et al. **SiMPl-Novel high QE photosensor**. *Nucl. Instrum. Meth. A*, **In Press, Corrected Proof**, 2009. 10.1016/j.nima.2009.05.182. 8

[28] W. G. Oldham and et al. **Triggering phenomena in avalanche diodes**. *IEEE Trans. Electron Dev.*, **19**:1056, 1972. 8

[29] Patrick Eckert et al. **Characterisation studies of silicon photomultipliers**. *Nucl. Instrum. Meth. A*, **620**[2-3]:217–226, 2010. doi:10.1016/j.nima.2010.03.169. 8, 9, 16, 45, 46, 50, 63, 64, 107, 113, 117

[30] P. Eckert. **Characterisation Studies of Silicon Photomultipliers for a Calorimeter for the ILC**. In *Workshop on New Photon Detectors*, 2009. 8

[31] Gomi Shinichi. **Research and development of MPPC for T2K experiment**. 8

[32] A. L. Lacaita et al. **On the bremsstrahlung origin of hot-carrier-induced photons in silicon devices**. *IEEE Trans. Electron. Dev.*, **40**:577–582, 1993. 10

[33] R. Mirzoyan et al. **Light emission in Si avalanches**. *Nucl. Instrum. Meth. A*, **610**[1]:98–100, 2009. 10.1016/j.nima.2009.05.081. 10

[34] Ivan Rech et al. **Optical crosstalk in single photon avalanche diode arrays: a new complete model**. *J. Modern Opt.*, **16**[12]:8381–8394, 2008. doi:10.1080/09500340408235272. 10, 107

[35] Y. Du and F. Retière. **After-pulsing and cross-talk in multi-pixel photon counters**. *Nucl. Instrum. Meth. A*, **596**[3]:396–401, 2008. doi:10.1016/j.nima.2008.08.130. 10, 11, 16, 45, 46, 50, 107, 117

[36] H. Oide. **Study of afterpulsing of MPPC with waveform analysis**. *PoS*, 2007. 11, 12, 16, 45, 50, 107, 117

[37] **PreLude 420**. Saint-Gobain, PreLude 420 (http://www.detectors.saint-gobain.com/). 15, 64, 65, 113, 117

[38] http://solutions.3mdeutschland.de. 15, 54

[39] **DELO-PHOTOBOND^{TM} 400**. DELO-PHOTOBOND^{TM} 400 (http://www.delo.de/fileadmin/datasheet/DELO-PHOTOBOND_400_), Januar 2012. 15

[40] T. Murase. **Development of PPD: characterization and simulation**. *PoS*, 2009. 16, 50, 117

[41] A. Velroyen. *Development of a Novel Detector Module for PET/MR Imaging Based on SiPMs and Fast Scintillation Crystals*. Diploma thesis, 2010. 23, 54, 67

[42] Tae Yong Song, Heyu Y Wu, Sergey Komarov, Stefan B Siegel, and Yuan-Chuan C Tai. **A sub-millimeter resolution PET detector module using a multi-pixel photon counter array**. *Physics in Medicine and Biology*, **55**[9]:2573–2587, 2010. doi:10.1088/0031-9155/55/9/010. 25

[43] A B Mann. **A Data Acquisition System for a Silicon Photomultiplier Based PET Detector**. 2008. 28, 38

[44] A. Kaplan. **Correction of SiPM temperature dependencies**. *Nucl. Instrum. Meth. A*, **610**[1]:114–117, 2009. doi:10.1016/j.nima.2009.05.137. 35, 37

[45] A Gil, J Rodriguez, V Alvarez, J Diaz, JJ Gomez-Cadenas, and D Lorca. **Programmable power supply system for SiPM bias**, 2011. doi:10.1109/NSSMIC.2011.6154298. 42

[46] J. Allison et al. **Geant4 developments and applications**. *IEEE Trans. Nucl. Sci.*, **53**[1]:270–278, 2006. doi:10.1109/TNS.2006.869826. 43, 54

[47] S. Agostinelli et al. **G4–a simulation toolkit**. *Nucl. Instrum. Meth. A*, **506**[3]:250–303, 2003. doi:10.1016/S0168-9002(03)01368-8. 43, 54

[48] S. Villa et al. **Photon emission from hot electrons in silicon**. *Phys. Rev.*, **52**[15]:10993–10993, 1995. doi:10.1103/PhysRevB.52.10993. 46

[49] D. K. Schroder. **Carrier lifetimes in silicon**. *IEEE Trans. Electron. Dev.*, **44**[1]:160–170, 1997. doi:10.1109/16.554806. 46

[50] P. Buzhan et al. **Large area silicon photomultipliers: Performance and applications**. *Nucl. Instrum. Meth. A*, **567**[1]:78–82, 2006. 54

[51] M. Heller. **AX-PET : A novel PET concept with G-APD readout**. In *New Developments In Photodetection*, 2011. 56

[52] M. Moszynski et al. **Absolute light output of scintillators**. *IEEE Trans. Nucl. Sci.*, **44**[3]:1052–1061, 1997. 10.1109/23.603803. 56, 65, 117

[53] E. V. D. van Loef et al. **High-energy-resolution scintillator: Ce3+ activated LaBr3**. *Applied Physics Letters*, **79**[10]:1573–1575, 2001. doi:10.1063/1.1385342. 56, 65, 117

[54] J. T. M. de Haas and P. Dorenbos. **Advances in Yield Calibration of Scintillators**. *Nuclear Science, IEEE Transactions on*, **55**[3]:1086–1092, 2008. doi:10.1109/TNS.2008.922819. 64, 113

[55] P. Dorenbos. **Light output and energy resolution of Ce3+-doped scintillators**. *Nucl. Instrum. Meth. A*, **486**[12]:208–213, 2002. doi:10.1016/s0168-9002(02)00704-0. 65, 117

[56] W W Moses and Planmed Scanditronix Perkin Elmer Casic Infn Ats. **Current trends in scintillator detectors and materials**. pages 123–128, Orosei, Italy, 2001. Elsevier Science Bv. 66

[57] S. Vinogradov et al. **Probabilistic distribution and noise factor of solid state photomultiplier signals, taking into account cross-talk processes**. *Bulletin of the Lebedev Physics Institute*, **36**[9]:253–259, 2009. 10.3103/S1068335609090012. doi:10.3103/S1068335609090012. 82

[58] S. Vinogradov et al. **Efficiency of Solid State Photomultipliers in Photon Number Resolution**. *IEEE Trans. Nucl. Sci.*, **58**[1]:9–16, 2011. doi:10.1109/TNS.2010.2096474. 82

[59] F Retiere, Y Du, S Foreman, P Kitching, A Kostin, T Lindner, M Low, P Masliah, I Moult, S Oser, H Tanaka, A Vacheret, F Retière, and Et al. **Characterization of Multi Pixel Photon Counters for T2K Near Detector**. *Nucl. Instrum. Meth. A*, **610**[1]:378–380, 2009. doi:10.1016/j.nima.2009.05.124. 82

[60] J Pulko, F R Schneider, A Velroyen, D Renker, and S I Ziegler. **A Monte-Carlo model of a SiPM coupled to a scintillating crystal**. *Journal of Instrumentation*, **7**[02]:P02009, 2012. 83

[61] W. Lustermann. **FACT First GAPD Cherenkov Telescope**. In *JENAM 2011*, 2011. 83

Declaration

This is to certify that Thesis entitled A Monte-Carlo Model of a Silicon Photomultiplier which is submitted by me in partial fulfilment of the requirement for the degree of doctor rerum naturalium (Dr. rer. nat.) is only my original work and due acknowledgement has been made in the text to all other material used.

Munich, October 21th 2012

Jožef Pulko